



Stefanie Runde

Design and Analysis of
fMRI Experiments
Probing
Brain Activity
Induced by
Tactile Stimulation

Diplomarbeit

HD-KIP-00-27

**Design and Analysis of
fMRI Experiments
Probing
Brain Activity
Induced by
Tactile Stimulation**

**This diploma thesis has been carried out by *Stefanie Runde* at the
KIRCHHOFF-INSTITUTE OF PHYSICS
UNIVERSITY OF HEIDELBERG
under the supervision of
Prof. Dr. Karlheinz Meier**

Faculty of Physics and Astronomy

University of Heidelberg

Diploma thesis
in Physics

submitted by

Stefanie Runde

born in Karlsruhe

September 2000

Abstract

This thesis presents the design and analysis of fMRI experiments on the processing of tactile information in the human brain. For this purpose the principles of neurology and fMRI relevant for the experiments are introduced. A pneumatically driven tactile display, whose non-interference with the fMRI image acquisition is verified, is used to effect tactile stimulation. The somatotopic representations in the primary and the secondary somatosensory cortex are successfully mapped at two distinct points (index finger and foot) for three healthy, seeing subjects. The analysis is performed by means of statistical parametric mapping of t-scores, a hypothesis testing approach based on the general linear model. The tactile stimulations elicited activation of the primary motor cortex for almost all image series in spite of precautions with regard to the subjects' comfort and immobility. The reproducibility of the resulting brain activities is examined in terms of location, extent and significance. It turns out that the location of the most significant point of activity can be reliably reproduced using three dimensional maps of t-scores while extent and intensity are subject to large random variations.

Inhalt

In dieser Arbeit werden Design und Analyse von fMRI Experimenten zur Erforschung der Verarbeitung taktiler Informationen im menschlichen Gehirn vorgestellt. Dazu werden die notwendigen Grundlagen der Neurologie und der funktionellen Magnetresonanztomographie erarbeitet. Taktile Stimulationen werden mit Hilfe eines pneumatischen taktilen Displays erzeugt. Es wird gezeigt, daß das taktile Display die fMRI Bildaufnahme nicht beeinflußt. Die somatotopische Repräsentation im primären und im sekundären somatosensorischen Kortex an je zwei diskreten Punkten (dem Zeigefinger und dem Fuß) wird bei drei gesunden, sehenden Probanden ermittelt. Die Analyse basiert auf dem sogenannten 'Statistical Parametric Mapping'. Dabei werden den Aktivitätsverlauf im Gehirn modellierende Hypothesen mittels linearer Regression getestet. Obwohl versucht wurde motorische Reize zu minimieren, wird durch taktile Stimulationen in fast allen Fällen der primäre Motorcortex mit angeregt. Die Reproduzierbarkeit der gefundenen Gehirnaktivitäten wird auf Ort, Ausdehnung und Signifikanz untersucht. Es stellt sich heraus, daß der Ort der stärksten Aktivität anhand von 3-D Karten der t-Werten verlässlich reproduziert werden kann, während Ausdehnung und Intensität größeren Schwankungen unterliegen.

Contents

Introduction	1
1 Processing Tactile and Motor Stimulation	3
1.1 The Brain's Functional Organization	3
1.2 The Cerebral Cortex	4
1.3 The Somatosensory Pathways	5
1.4 Somatosensory Receptors	5
1.5 Somatosensory Cortical Regions	6
1.5.1 Functionality	6
1.5.2 Location	7
1.5.3 Modality-Specific Organization	7
1.5.4 Somatotopic Organization of SI and SII	8
1.6 Motor Task Processing	9
2 Basics of fMRI	11
2.1 Concepts of Nuclear Magnetic Resonance	11
2.2 Principles of Magnetic Resonance Imaging	12
2.3 Echo-Planar Imaging	13
2.4 The BOLD Effect	14
2.5 Artifacts and Noise	15
2.5.1 Artifacts	15
2.5.2 Noise	15
2.6 MRI-System in Strasburg	16
3 The Pneumatically driven Tactile Display	19
3.1 Description of the PTD	19
3.2 Functionality of the PTD	20
3.3 The Visor software and Pattern Generation	22
4 Statistical Parametric Mapping	25
4.1 Preprocessing	26
4.1.1 Principles of Spatial Transformations in Brain Imaging	26
4.1.2 Realignment (Within Modality Coregistration)	26

4.1.3	Between Modality Coregistration	27
4.1.4	Normalization	27
4.1.5	Smoothing	29
4.2	Statistical Models	30
4.2.1	The General Linear Model	30
4.2.2	Low Frequency Confounds	31
4.2.3	t-Test	31
4.2.4	Contrasts	32
4.2.5	Inference	33
	4.2.5.1 Hypothesis Testing	33
	4.2.5.2 The Multiple Comparison Problem	33
	4.2.5.3 Bonferroni Correction	33
	4.2.5.4 Random Field Theory and Euler Characteristic	33
4.3	Using SPM99 for Statistical Analysis	35
4.3.1	Setting up a Design Matrix in SPM99	35
4.3.2	Using the Thresholding Function in SPM99	37
4.3.3	Automatisation of the Analysis	38
5	Experiments	40
5.1	Experimental Setup	40
	5.1.1 Subjects and Experimental Setting	40
	5.1.2 Mounting of the modules	41
5.2	Mapping SI for One Subject	42
	5.2.1 Experimental Procedure	42
	5.2.2 SPM Analysis	43
5.3	Tactile versus Motor Stimulation	48
	5.3.1 Experimental Procedure	48
	5.3.2 SPM Analysis and Overlap	48
5.4	Reproducibility of Motor Stimulation	50
5.5	Reproducibility of Tactile Stimulation	51
	5.5.1 Experimental Procedure	51
	5.5.2 SPM Analysis	52
5.6	Intersubject Analysis	61
5.7	Non-interference of the PTD with the MRI	66
5.8	t-Scores Reviewed	67
	5.8.1 Signal and Cascades	67
	5.8.2 Autocovariance	70
	5.8.3 Fourier Transformation	71
	Summary and Outlook	75
A	Directions and Planes in the Human Brain	77

B	Affine Transformations in Preprocessing	78
B.1	General Affine Transformation	78
B.2	Voxel to Real World Coordinates	78
B.3	Realignment	79
B.4	Affine Normalization	79
C	Coordinates in SPM99	80
C.1	Talairach Coordinate System	80
C.2	The MNI brain	80
D	Examples for Batch-Files in SPM99	82

Introduction

The Electronic Vision Group at the Kirchhoff Institute for Physics has been founded in 1994 with the initial goal to develop a practical tactile vision substitution system (TVSS). The TVSS was intended to supplement the orientation of blind or visually impaired persons by making use of their tactile perception. This initial research goal has recently been achieved. A small, single chip camera with image sensors based on CMOS technology performs the image acquisition [Loo99]. The main step of the image processing takes place in the EDDA chip (EDge Detection Array), which converts analog greyscale images from the camera into a digitally coded edge image [Sch99]. The Virtual Tactile Display (VTD) constitutes the output device of the project based on piezoelectric actuators assembled in a movable tactile output unit. It can be moved around a two dimensional surface to explore the line structure of a virtual raised image [Mau98]. A mobile image processing computer completes the TVSS. It comprises a miniaturized PC in combination with additional electronics for image processing purposes, cooperates with the camera chip and EDDA and can address the VTD as well as other peripheral devices. For more information on the Electronic Vision Group see also [Vis00].

While the Electronic Vision Project initially focussed on using the infrastructure available at the ASIC Laboratory for Microelectronics to develop intelligent vision chips, it soon became clear that the interdisciplinary nature of the project offers exciting research opportunities also in neighbouring fields. The project was extended to include a division that is concerned with basic research on tactile perception. The motivation of this work is to optimize the information transfer via the tactile channel to the human brain. In order to investigate the processing of tactile stimulation in the human brain experiments applying fMRI are performed. Functional Magnetic Resonance Imaging (fMRI) presents a non-invasive method capable of monitoring the change in blood oxygenation due to brain activity. It is used to record the human brain's response to well-defined, reproducible tactile stimulations, which are generated by a Pneumatically driven Tactile Display (PTD) developed within the scope of this project.

This thesis presents the results of first fMRI experiments with three seeing subjects using the PTD for tactile stimulation. Their aim is to map the somatotopy of the primary somatosensory cortex (the 'somatosensory homunculus'). In addition the relationship of tactile and motor activation of the human brain and their reproducibility are investigated. Another experiment with a brain phantom probes the interference between the PTD and the MRI image acquisition.

The first chapter of this thesis is dedicated to those structures of the human brain that are

most important for processing tactile and motor stimulation. The next one introduces the principles of fMRI completing the theoretical background for the experiments. The PTD is presented in chapter three. The analysis of the fMRI data is performed with the software package SPM99¹ that uses statistical parametric maps of t-scores to locate activation sites in the human brain. Additionally the data at detected activation sites is inspected by standard correlation analysis methods to verify their significance. The statistical knowledge required to work with SPM99 is summarized in chapter four while chapter five presents the results from the analyzed experiments.

¹Wellcome Department of Cognitive Neurology, London, UK

Chapter 1

Processing Tactile and Motor Stimulation in the Human Brain

The conducted experiments involve mostly tactile stimulation but also some motor tasks for reference purpose. This chapter focuses on a presentation of structures of the human brain that are involved in processing tactile and motor stimulation. Following short introductions on theories of the human brain's functional organization and the structure of the cerebral cortex, the somatosensory information pathway is sketched and a summary of the different peripheral receptors is given. Then an overview of those parts of the brain (mostly in the cerebral cortex) concerned with tactile perception and their somatotopic organization will be presented. The relevant regions are the primary and secondary somatosensory cortex as well as the related association areas. Finally motor task processing is introduced.

1.1 The Brain's Functional Organization

Historically two different and opposing theories dominated the concepts of brain functionality in the nineteenth century: The aggregate field view and localism. The latter claimed that every mental function, including emotion, is carried out by a single, precisely localized and specialized area of the brain. On the contrary, the followers of the aggregate field view believed that all parts of the brain especially the cerebral hemispheres participate in all mental functions. In 1876 C. Wernicke introduced the idea of 'distributed processing' that still dominates the present concept of brain functionality. He suggested that the most basic mental function (those concerned with simple perceptual and motor activities) are localized to single cortical areas. More complex intellectual functions are then made possible by interconnection between those functional sites. The current theory on brain functionality is a more elaborate version of Wernicke's 'distributed processing' [Kan91]. Thereby the brain's functional organization is based on two fundamental principles: *functional integration* and *functional segregation*. Functional segregation implies

that a cortical region is specialized for some aspects of perceptual or motor processing and that this area is anatomically segregated in the cerebral cortex. A mental function may then involve many of those functionally segregated areas whose interaction is mediated by the functional integration among them. The techniques available to analyze functional brain images can be grouped as multivariate and univariate approaches on a procedural level which correspond to the theories of functional segregation and integration respectively [Fra97]. The univariate approaches are collectively brought under the heading of *Statistical Parametric Mapping* (Chapter 4).

1.2 The Cerebral Cortex

The Cerebral Cortex is located on the surface of the brain and is highly convoluted. Elevated convolutions, called gyri, are separated by grooves called sulci (or fissures if they are deep). In each of the brain's two cerebral hemispheres the overlying cortex is divided into four anatomically distinct lobes: The frontal, parietal, temporal and occipital lobe (see fig. 1.1).

The different lobes are specialized for remarkably distinct functions. The frontal lobe is mainly concerned with control of movement, the parietal lobe with somatic sensation and proprioception¹. They are separated by the central sulcus. The occipital lobe is important for vision, the temporal lobe for hearing, speech, various sensory functions as well as aspects of learning memory and emotion. The following sections will be mainly concerned with the primary somatosensory cortex located in the parietal lobe. Section 1.6 focuses on the frontal lobe due to its importance for movement.

One approach to parcel the cerebral cortex is of histological nature based on cellular characteristics. The most widely used classification was proposed by K. Brodman in 1909 and contains 52 cytoarchitectonic areas (Brodman areas) [Afi98]. It is remarkable that the histological and functional classifications are correlated, i. e. that different Brodman areas resemble different functional areas. In particular this is true for the primary somatosensory cortex as will be explained in section 1.5.3.

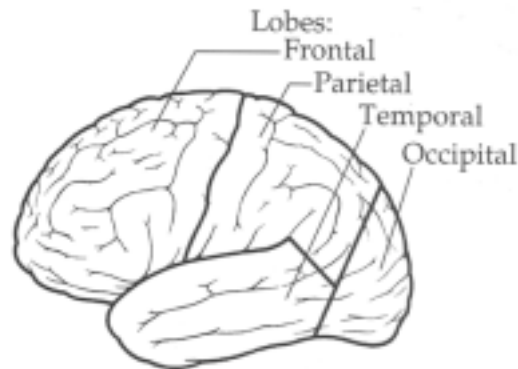


Figure 1.1: The 4 lobes of the cerebral cortex [Mar96]. The frontal and the parietal lobe are separated by the central sulcus (bold line).

¹limb position sense

1.3 The Somatosensory Pathways

The somatic (or bodily) senses consist of four distinct modalities: limb position sense, touch, thermal sensation, and pain. Two parallel ascending pathways transmit the somatic information to the primary somatosensory cortex. The ‘dorsal column-medial lemniscal system’ mediates touch and limb position while the ‘anterolateral system’ subserves pain and temperature sense (and to a much lesser extent touch). Starting at a peripheral sensory receptor the information is passed on to the spinal cord and then the brain stem. From there it continues through the thalamus to the primary somatosensory cortex (see fig. 1.2). Sensory information that enters the spinal cord from the left side of the body crosses over to the right side of the nervous system (either within the spinal cord or in the brainstem) before being conveyed to the cerebral cortex. Thus each hemisphere of the cerebral cortex is concerned primarily with sensory (and motor) processes on the contralateral side of the body.

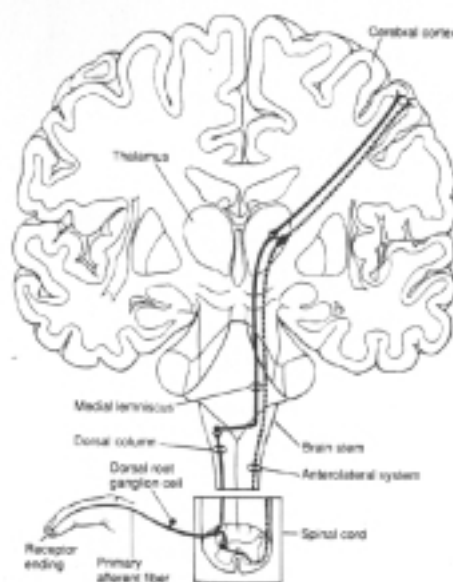


Figure 1.2: Illustration of the somatosensory pathways: dorsal column-medial and anterolateral [Kan91].

1.4 Somatosensory Receptors

The sensation of touch is mediated by mechanoreceptors. Mechanoreceptors can be divided into two major functional groups. The *slowly adapting* ones respond continuously to a persistent stimulus while *rapidly adapting* mechanoreceptors respond only at the onset (and often also at the termination) of the stimulus. Slowly adapting receptors are

Merkel's receptors in superficial skin and *Ruffini's corpuscles* in subcutaneous tissue. *Meissner's* and *Pacinian corpuscles* belong to the group of rapidly adapting receptors and are also located in superficial skin and subcutaneous tissue respectively.

Hairy and glabrous (hairless) skin do not contain the same mechanoreceptors. Hairy skin has hair follicle receptors, that respond to flutter stimulation, and Merkel's receptors (slowly adapting) while glabrous skin incorporates Meissner's corpuscles (rapidly adapting) and Merkel's receptors. The mechanoreceptors of the subcutaneous tissue are identical for both skin types (see fig. 1.3).

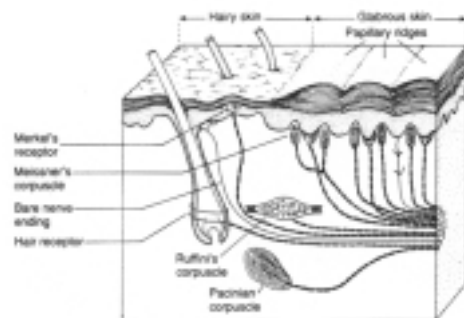


Figure 1.3: The cutaneous and subcutaneous mechanoreceptors [Kan91].

1.5 Somatosensory Cortical Regions

1.5.1 Functionality

There are three major somatosensory cortical areas. The *primary somatosensory cortex (SI)* receives the direct projection from the thalamus. It then projects to the *secondary somatosensory cortex (SII)* and the *somatosensory association area* (see fig. 1.5). The primary somatosensory cortex is the most important part for sensory perception. Ablation of SI will result in the loss of all modalities of sensation in the immediate postoperative period. Pain and temperature sensation will return in form of a crude awareness but discriminative touch and proprioception are lost forever. Removal of SII will cause severe impairment in the discrimination of both shape and texture. The secondary somatosensory cortex is also important for the conscious perception of noxious stimuli. In addition there is some evidence that vibrational stimulation is primarily processed in SII [Mal99]. The somatosensory association area is concerned with higher order processing. Damage to the latter will produce complex abnormalities in attending to sensations from the contralateral half of the body.

1.5.2 Location

The primary somatosensory cortex is located in the postcentral gyrus of the parietal lobe. Its position is posterior to the central sulcus and anterior to the postcentral sulcus (see fig. 1.4). In the sagittal plane (the plane separating the two hemispheres) it ends at the cingulate sulcus (see fig. 1.7). The lateral sulcus, which also anatomically separates the parietal from the temporal lobe, terminates the postcentral sulcus on the lateral surface of the cerebral cortex (see fig. 1.4).

The secondary somatosensory cortex is mostly located in the superior bank and depth of the lateral sulcus (parietal operculum) and on the most inferior aspect of the postcentral gyrus. It is hidden from a superficial view of the brain. The somatosensory association area can be found in the superior parietal lobe and extends further into the posterior part of the parietal cortex.

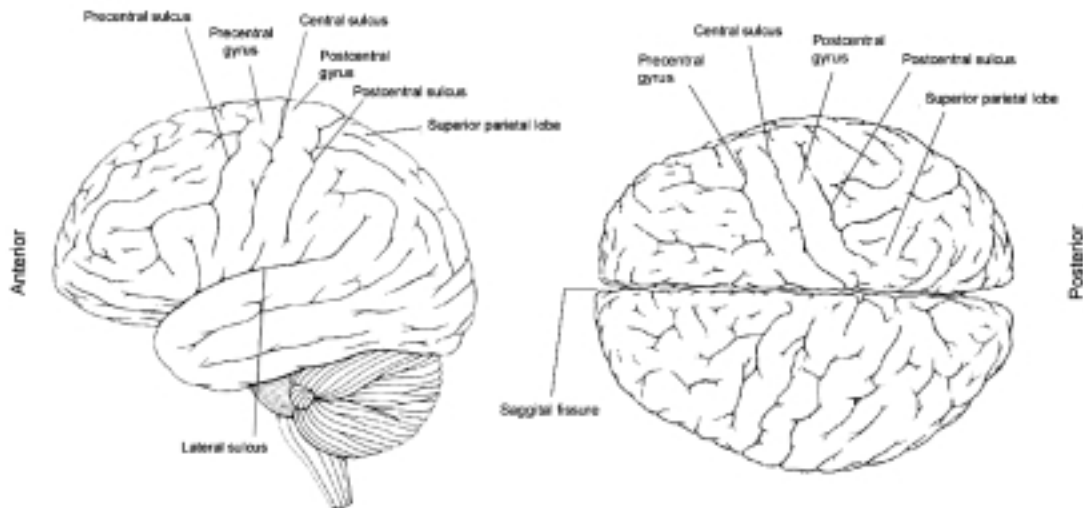


Figure 1.4: Dorsal and lateral view of the brain [Mar96].

1.5.3 Modality-Specific Organization

The postcentral sulcus corresponds to Brodman areas 1, 2 and 3. Area 3 is further divided into 2 parts: 3b on the posterior wall of the central sulcus and 3a in the depth of the central sulcus (see fig. 1.5). As in other cortical areas regions with different cytoarchitecture within the primary somatosensory cortex subserve different functions. Brodman areas 2 and 3a receive information from receptors located in deep structures, such as muscles and joints, areas 1 and 3b from mechanoreceptors of the skin (see fig. 1.5). In each of these areas a separate representation of the body can be found (see the following paragraph). The representations in 1 and 3b are complete and highly detailed while that in areas 2 and 3a appear more coarse. Areas 2 and 3a are important in limb position sense and shape discrimination of grasped objects while areas 1 and 3b are responsible for touch perception.

Concerning tactile stimulation areas 1 and 3b as well as areas 5 and 7 (posterior parietal cortex) are relevant.

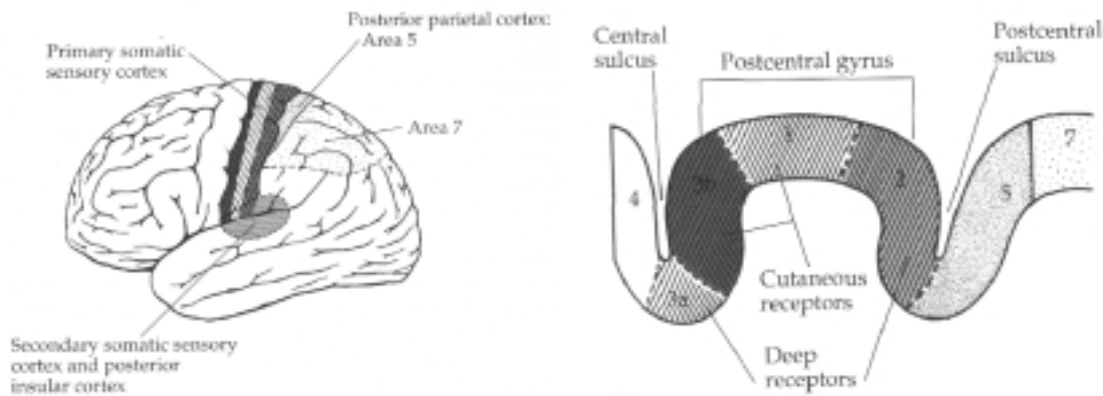


Figure 1.5: The somatosensory cortical regions and the corresponding Brodman areas [Mar96].

1.5.4 Somatotopic Organization of SI and SII

The most striking feature of the organization of all sensory systems, and in particular of the somatosensory system, is that the inputs from the peripheral receptor sheet (for the somatosensory system: the body surface) are systematically mapped onto structures of the brain. In general this kind of mapping is termed ‘somatotopy’ and the somatotopic map of SI has been named ‘*Somatosensory Homunculus*’. It is remarkably similar to a map of the surface of the body with the different body parts more or less in the same order, i. e. head \rightarrow arm \rightarrow leg. The representations of the various body parts is not proportional to their size but instead related to their importance for discriminative tactile tasks. The fingers cover a large area while the leg’s portion is much smaller (see fig. 1.6, right). This distortion reflects differences in innervation density in different areas of the body. The secondary somatosensory cortex exhibits a similar somatotopic organization but it is not as precise as that of SI. Also it is often bilateral while the somatosensory homunculus of SI refers to the contralateral side of the body (except for the face representation which is also bilateral).

According to [Mar96] the somatosensory homunculus should neither be identical for everybody nor necessarily static. Instead he expects it to be dynamically controlled by the pattern of use of different body parts in tactile exploration. If for example one body part is prevented from use in tactile discrimination its cortical representation should shrink. In contrast, if one part is used extensively its representation most likely expands. By this rationality a blind person who is accomplished in reading in Braille code would be apt to exhibit a large representation of the index and the middle finger.

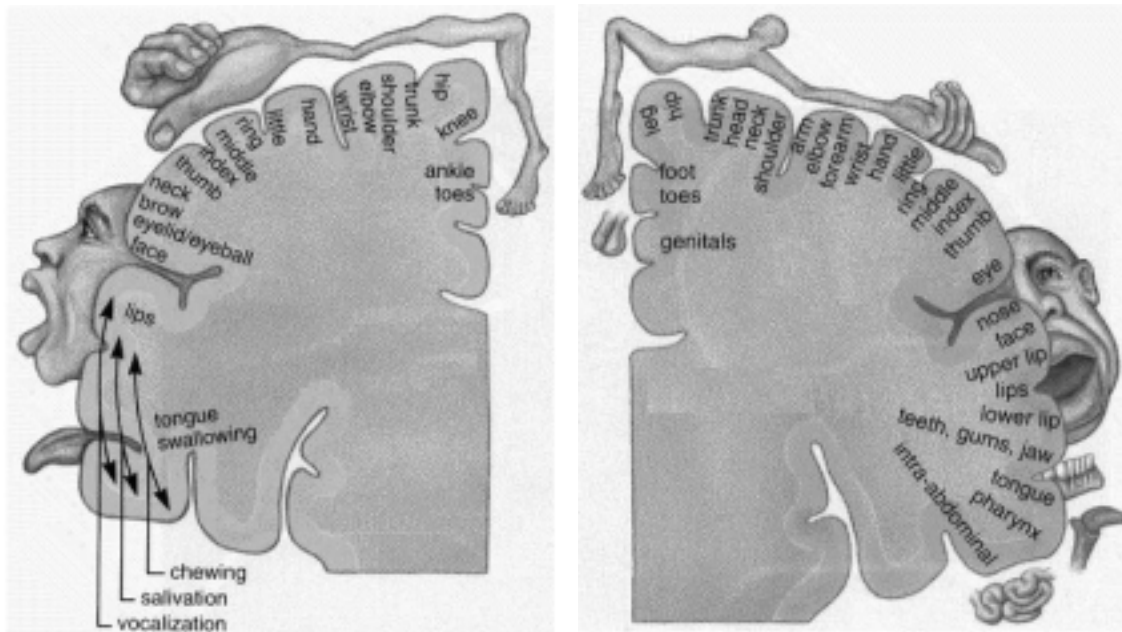


Figure 1.6: Motor (left) and somatosensory (right) homunculus.

1.6 Motor Task Processing

In section 1.2 the frontal lobe has been identified to be the cerebral cortical area responsible for the control of movement. The pertinent areas are classified as *primary motor area (MI)*, *supplementary motor area (MII)* and *premotor area*. The latter two are also known collectively as the nonprimary motor cortex. MI governs the initiation of highly skilled fine movements (e.g. sewing) but also of simple motor tasks. MII is crucial in the temporal organization of movement. Its role for simple motor task is less significant than that of MI. The premotor area is concerned with voluntary motor function dependent on sensory inputs (visual, auditory, somatosensory). The cerebellum is also involved in the processing of motor tasks.

The primary somatosensory and the primary motor cortex are direct anatomical neighbours. The first is located on the postcentral gyrus, the latter on the precentral gyrus with the central sulcus separating them. MI is bordered by the lateral and the cingulate sulcus on the lateral and medial side respectively as is SI. A precise but disproportionate somatotopic representation of the different body parts determines the *motor homunculus* (see fig. 1.6), the analogue to the somatosensory homunculus. MII can be found on the medial surface of the frontal lobe anterior to the medial extension of MI. The premotor area extends MII laterally and is located anterior to MI (see fig. 1.7). The primary and the nonprimary motor cortex correspond to Brodman areas 4 and 6 respectively.

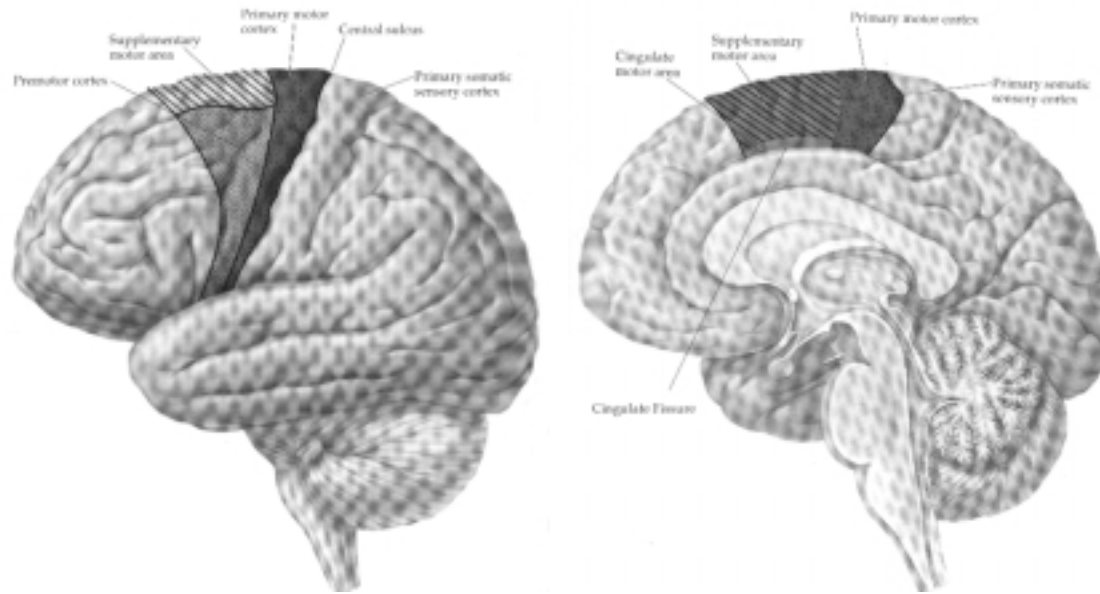


Figure 1.7: The motor areas in the cerebral cortex [Mar96].

The cerebellum also plays a key role in movement. It does not affect the excitability of motor neurons directly, but it does so indirectly through actions on the descending motor pathways. Damage to the cerebellum results in erratic and uncoordinated movement.

After the key features of somatosensory and motor information processing in the human brain have been introduced now, the question arises of how to measure brain activity in the pertinent cerebral cortical regions (and the cerebellum for motor activity). The next chapter is devoted to functional magnetic resonance imaging.

Chapter 2

Basics of fMRI

Brain activity is monitored by means of *functional Magnetic Resonance Imaging* in the reported experiments. MRI is a non-invasive imaging technique based upon the interaction between a non-zero nuclear spin and an external magnetic field. *Echo-Planar Imaging* is an ultra-fast imaging method that allows to take 3-D images of a human head within only a few seconds. The functionally sensitive contrast used originates in the **Blood Oxygenation Level Dependent** effect. It is caused by the different magnetic properties of oxygenated and deoxygenated haemoglobin.

2.1 Concepts of Nuclear Magnetic Resonance

In a static external magnetic field B_0 a nuclear spin of $I = \frac{1}{2}$ can occupy two different energy levels due to the Zeemann-interaction. Their population can be described by the Boltzmann factor $\frac{N^-}{N^+} = e^{-\frac{\Delta E}{kT}}$. $\Delta E = \hbar\omega$ corresponds to the energy difference between the two states. Transitions between the two states involve photons of the Larmor-frequency $\omega = \gamma B$ (where γ is the gyromagnetic ratio) and can be caused by a short pulse of radio frequency energy which is generated by a rf-coil (the same rf-coil that also detects the image signal in MRI). A '90°-pulse' will rotate the net magnetization M_0 from its initial position along the z -axis into the xy -plane. The longitudinal magnetization after the rf-pulse is governed by $M_Z = M_0(1 - e^{-\frac{t}{T_1}})$.

T_1 is the *spin-lattice* or *longitudinal* relaxation time. Dephasing of the spins takes place according to $M_{XY} = M_{XY_0}e^{-\frac{t}{T_2}}$. T_2 is called the *spin-spin* or *transverse* relaxation time. T_2 is always less than or equal to T_1 . There are several potential causes for loss of coherence. True T_2 originates in the movement of adjacent spins due to molecular interaction. Main field inhomogeneities result in T_2^{inhom} and sample-induced inhomogeneities, i.e. differences in magnetic susceptibility, in $T_2^{suscept}$. These yield a total transverse relaxation time T_2^* according to $\frac{1}{T_2^*} = \frac{1}{T_2} + \frac{1}{T_2^{inhom}} + \frac{1}{T_2^{suscept}}$ [Bro99].

Figure 2.1 depicts a commonly used spin-echo imaging sequence. Here the 90°-pulse is followed by a 180°-pulse (spin flip), which aligns M_0 anti parallel to the z -axis and causes a reversal of the phases relative to the resonant frequency. The signal S depends on both

T_1 and T_2 according to $S \sim \rho(1 - e^{-\frac{TR}{T_1}})e^{-\frac{TE}{T_2}}$ where ρ is the spin density, TR the repetition time and TE the echo time (see fig 2.2).

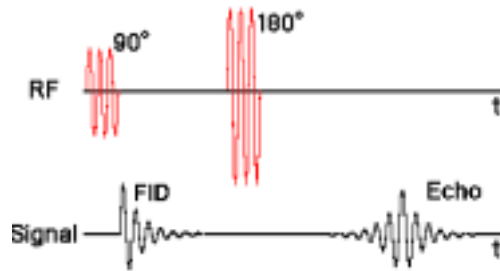


Figure 2.1: The signal of a spin-echo sequence [Hor00]; FID = Free Induction Decay.

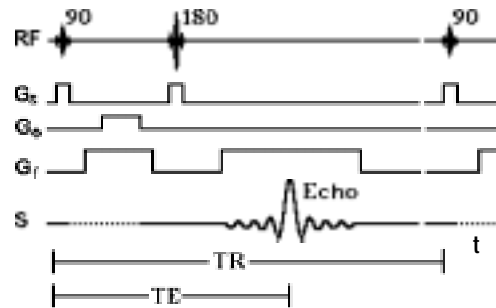


Figure 2.2: The time scheme of a spin-echo sequence [Hor00].

2.2 Principles of Magnetic Resonance Imaging

A natural choice for probing the body with MRI techniques is the ^1H nucleus. It owns a spin of $1/2$ and is the most abundant isotope for hydrogen. The body tissues are primarily composed of water and fat, both of which contain hydrogen. Its gyromagnetic ratio is large resulting in strong sensitivity to the applied magnetic field.

MRI is based on the Larmor frequency's dependence on the magnetic field strength. The magnetic field is made spatially dependent through the application of magnetic field gradients in order to assign different proton frequencies to different regions. These gradients are only small linear perturbations to the main magnetic field B_0 typically producing field distortions of less than 1 %. The gradients are applied for short periods of time and are thus termed gradient pulses.

Three different gradients are required to obtain a 3-D image: *slice selection* G_s , *frequency encoding* G_f and *phase encoding* gradient G_ϕ . Convention is to choose the z-axis parallel to B_0 and G_s . The presence of magnetic field gradients requires an expanded version of the Larmor equation namely $\omega_i = \gamma(B_0 + \vec{G} \cdot \vec{r}_i)$ where ω_i is the frequency of the nuclear spin at position \vec{r}_i and \vec{G} is the total gradient.

The slice selection gradient G_s is applied in conjunction with the rf-pulse so that only the spins in the selected slice are affected. The phase encoding gradient is then applied in the y-direction. When it is turned off the spins resume their initial ω but they are now out of phase by an amount that is determined by the duration and magnitude of G_ϕ , i.e. G_ϕ leaves a y-dependence of the phase. Finally the frequency encoding gradient G_f is applied along the x-axis introducing a x-dependence of the frequency. Now every spin-packet (sum of all spins in a voxel¹) in the selected slice has a unique combination of frequency and phase. Figures 2.2 and 2.3 show the time scheme of a spin-echo and an

¹volume element

echo-planar imaging sequence.

The phase encoding gradient is the one that is modified during image acquisition. For a resolution of 64 pixels in the phase encoding direction, G_ϕ is varied in 64 steps. At each step one line of k-space along the frequency encoding direction is read out.

The field of view (FOV) and thus the voxel size for a given resolution is determined by the gradient for every direction. A resolution of 64×64 in the xy-plane and a voxel size of $4 \times 4 \times 5 \text{ mm}^3$ yields a FOV of $25.6 \times 25.6 \text{ cm}^2$. The choice of the FOV is critical since wrap around (aliasing) occurs when the digitization rate is less than the spectral width, i.e. the frequencies in the signal (see also 2.5). The wrap around artifact is the occurrence of a part of the imaged anatomy, which is located outside the FOV, inside the FOV. The field of view also influences the signal to noise ratio (SNR): a smaller FOV yields a smaller SNR.

2.3 Echo-Planar Imaging

EPI is an ultra-fast imaging method particularly useful in fMRI as it is capable of monitoring changes in blood oxygenation with a spatial resolution in the order of a few millimeters (about the same as for PET) and a temporal resolution of less than 100 ms per slice. It is characterized by a series of very rapid gradient reversals in the frequency encoding direction. Conventional imaging sequences record one line of k-space during each phase encoding step, i.e. only one line every TR. Echo-Planar Imaging on the contrary measures all lines of k-space in one slice in a single TR period. Figures 2.3 and 2.4 show the time scheme of an EPI sequence.

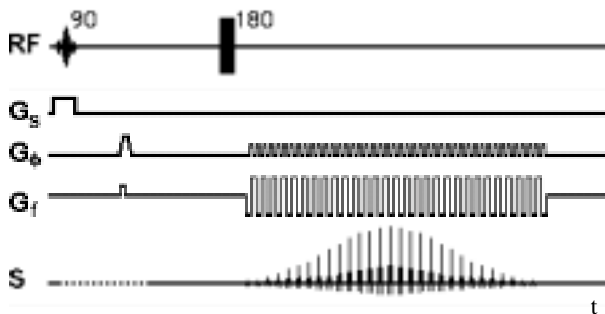


Figure 2.3: The time scheme of an EPI sequence [Hor00].

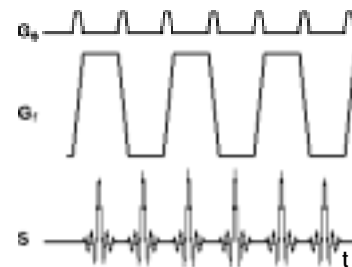


Figure 2.4: Zoom into the time scheme of an EPI sequence [Hor00].

2.4 The BOLD Effect

The Blood Oxygenation Level Dependent effect generates the contrast for fMRI. Haemoglobin is an inherent magnetic-susceptibility-induced T_2^* -shortening intravascular contrast agent found in every tissue. Oxygenated haemoglobin (HbO_2) contained in arterial blood is diamagnetic and thus hardly affects the magnetic susceptibility, i. e. it does not greatly affect tissue T_2^* . Deoxygenated haemoglobin (Hb) is significantly more paramagnetic (due to 4 unpaired electrons) disturbing the local magnetic field and reducing tissue T_2^* .

Neuronal activation causes an increased Cerebral Blood Flow (CBF) to the activated region as well as an increase in Cerebral Blood Volume (CBV) and oxygen delivery. As CBF increases more than CBV, oxygen delivery quickly exceeds slight increases in local oxygen needs owing to the activation. Thus any activated voxel will, after a short delay, contain a surplus of HbO_2 . Thus the tissue T_2^* is prolonged and signal increased [Tra98]. The BOLD contrast activation changes are approximately linear as a function of main magnetic field strength [Fri94a]. At field strengths of 1.5-2.0 Tesla signal changes of 1-2% can be expected [Box95] but larger signals are also possible especially in the vicinity of large blood vessels.

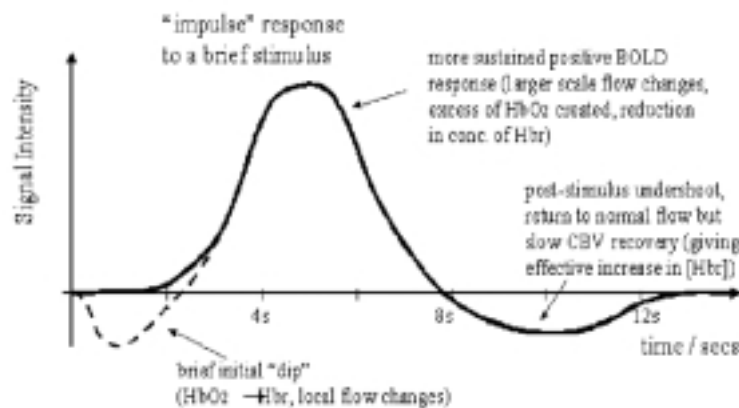


Figure 2.5: The BOLD signal response also called the *haemodynamic response function* [Jez99].

Figure 2.5 depicts a typical BOLD signal with an initial 'dip' due to increased oxygen need. In SI a peak in the fMRI BOLD signal is reached between 5-8 seconds after the onset of stimulus corresponding to a **haemodynamic response function** with a FWHM of approximately 6 seconds [Ban93]. A post-stimulus undershoot is observed that is caused by an excess of Hb since it takes longer for the CBV than the CBF to return to normal. The spatial as well as the temporal resolution of fMRI may ultimately be limited by the characteristics of the BOLD effect. Blood vessels during stimulation become more oxygenated over an area of a few millimeters in diameter around the site of neuronal activity. The haemodynamic response function peaks in the order of a few seconds. Rapid imaging techniques like EPI can acquire a single-slice image in less than 100 ms. Thus the temporal resolution is intrinsically restricted to the haemodynamic response.

2.5 Artifacts and Noise

2.5.1 Artifacts

Since fMRI techniques are sensitized to T_2^* they are responsive to all kinds of magnetic susceptibility differences, as they occur e. g. between air, bone and different tissue types. These inhomogeneities can cause geometric distortions of the image, which are particularly critical in EPI due to its very low frequency per point in the phase encoding direction. Another common problem with EPI images are *Nyquist ghosts*, i. e. low intensity ($\sim 1\%$) secondary images which appear a half FOV away from the real image. They are due to timing or phase differences between the odd and even echoes in the echo train. Figure 2.6 shows an image (n1_2_011 .img) taken during one of the reported experiments that exemplifies the occurrence of a Nyquist ghost. The presented axial section of a raw EPI image was brightened to make the ghost appear.

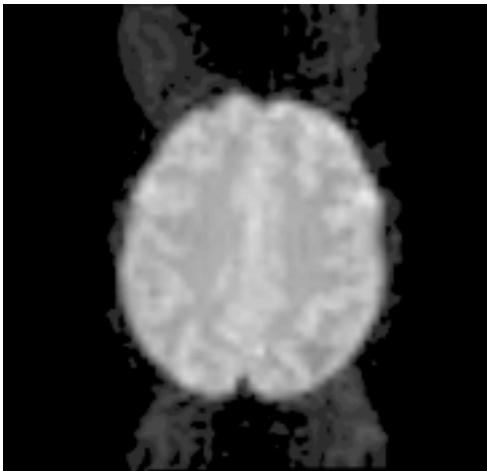


Figure 2.6: An example of a Nyquist ghost.

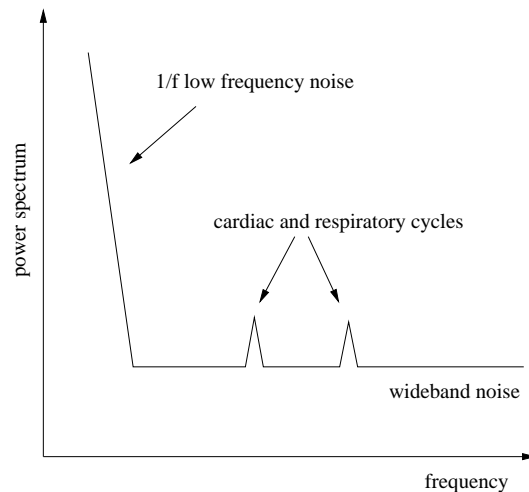


Figure 2.7: The typical power spectrum of noise in an fMRI image.

2.5.2 Noise

The noise spectrum of the fMRI signal comprises a low-frequency and wideband component. In addition periodic physiological noise sources can appear as focal peaks in the spectrum for short TR ($TR < 6s$). Figure 2.7 schematically illustrates the noise spectrum of a fMRI signal. The actual signal of frequency f_0 would appear as a high focal peak at f_0 . The non-periodic, low-frequency noise components arise because of long term physiological shifts, movement related noise remaining after realignment or of instrumental instability. This noise component typically exhibits a $1/f$ characteristic. The wideband noise originates in the r.f. coil and within the subject. It determines the SNR of the MRI

images. The cardiac and the respiratory cycle are periodic noise sources in fMRI. The cardiac cycle causes periodic blood flow and pulsatile bulk motion due to induced pressure variation, which can extend through the entire brain. Generalized variation in blood oxygenation and bulk displacement of the head in reaction to breathing is brought about by the respiratory cycle. In entire brain EPI the TR is typically a several seconds (4 and 5 s in the conducted experiments). The cardiac and the respiratory cycle exhibit frequencies of about 1 and 0.25 Hz correspondingly. These are above the Nyquist limits of 0.125 and 0.1 Hz for the given TRs so aliasing takes place.

2.6 MRI-System in Strasburg

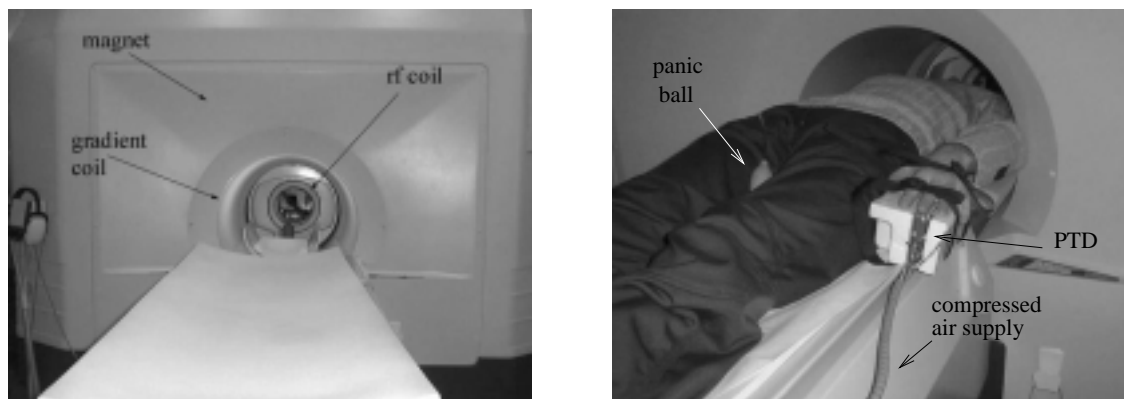


Figure 2.8: The MRI scanner at the Faculty of Medicine of the University Louis Pasteur, Strasburg, France without and with a subject.

The fMRI measurements are performed with the MRI scanner (Bruker, Karlsruhe) of the Biological Physics Institute of the Faculty of Medicine at the University Louis Pasteur in Strasburg, France. It is used both for clinical application and for research. Figure 2.8 shows the MRI scanner with and without a subject. For every subject a series of functional EPI-scans was performed with an echo-time $TE = 43$ ms and a repetition time of $TR = 4$ s or $TR = 5$ s. Additionally a structural, high-resolution T_2 -weighted (Turbo-RARE) scan was made for each subject.

The superconductive NoTi magnet (Oxford Co, weight = 2 t) produces a magnetic field of 2 Tesla. The homogeneity is 0.1 ppm in a 40 cm sphere centered in the magnet. The inside diameter of the tube is 55 cm with gradients and body coil inserted and reduced to 33 cm with the EPI gradient coil inserted. Maximum gradient strengths are $30 \frac{mT}{m}$. The rf head coil is a quadrature bird cage coil (see fig. 2.9) of 28 cm in outside and 25 cm in useful inside diameter. The rf coil is a transmit and receive coil. It both creates the B-field that rotates the net magnetization and detects the transverse magnetization.

Two concentric solenoids provide active shielding where the external one acts to counter the field and shield the room. This results in a 0.5 mT peripheral magnetic field of 6 m in

the z-direction and 3 m in the x- and y-directions. Data acquisition is performed with the NMR spectrometer software *tomikon* and the imaging software *ParaVision 2.0* (Bruker). The image data is initially in Bruker format and later converted to ANALYZE format for further processing. The ANALYZE format uses a header file with every image file that contains relevant information, like dimensions, voxel size, etc.. The header file can be customized. The image file is a concatenation of image lines along the x-direction of a left-handed coordinate system. For details see [Ana00].

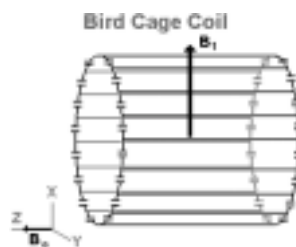


Figure 2.9: A bird cage head coil typically used in fMRI [Hor00]

Chapter 3

The Pneumatically driven Tactile Display

Experiments investigating the processing of tactile stimulation in the human brain require a dedicated device that can generate well-defined, adjustable and reproducible stimuli. In an fMRI environment this device cannot rely on electronic elements as they are likely to fail and may even locally change the magnetic field which inevitably leads to image distortion. Ferromagnetic materials have to be avoided for the same and for security reasons. The device has to be small as the tube of the MRI system is only 55 cm in inside diameter.

Some devices have been successfully applied in fMRI experiments of tactile stimulation. Pneumatic fingerclips have been employed by C. Stippich in clinical applications. They can deliver ‘fully automated tactile stimulation’ [Sti99]. Another successfully applied device is a piezoceramic vibrotactile stimulator. It does not seem to disturb the MRI image acquisition in spite of the high voltages needed for the piezo [Har00]. Both of these devices stimulate single areas of the skin. Within the scope of this project a new *Pneumatically driven Tactile Display* has been developed by T. Maucher¹.

3.1 Description of the PTD

The PTD is a modular, two-dimensional device that is designed to present tactile patterns without disturbing the MRI image acquisition. The display itself does not include any electronic or ferromagnetic parts and the control units are placed outside the magnet. A variety of tactile stimulation comprising both static and vibrational patterns of variable frequencies can be performed. These patterns can be interactively adjusted via a dedicated software. The display is made up of 16 modules (fig. 3.1), each one consisting of 4 pneumatically driven tactile elements (taxels). A great deal of flexibility is provided by the modularity of the PTD. The 16 modules can be arranged to form a regular square matrix of 8×8 taxels, which are spaced in intervals of 15 mm so that an area of $100 \text{ mm} \times 100 \text{ mm}$

¹Phd student at the Kirchhoff-Institute for Physics (KIP) of the University of Heidelberg

is regularly filled. It is also possible to attach single modules to different parts of the body. This was done in the experiments that will be reported. Each one of the 64 taxels can be addressed individually with a maximum frequency of 20 Hz, i. e. each taxel has a maximum temporal resolution of 50 ms.

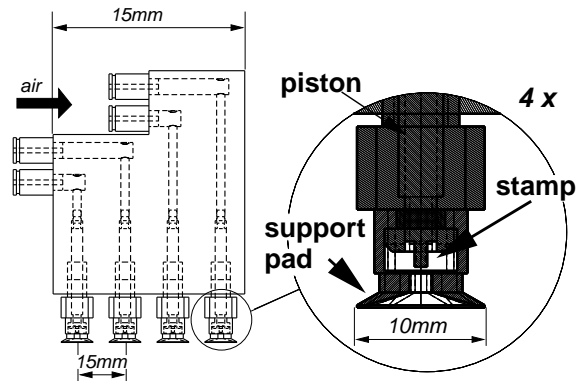


Figure 3.1: Detailed drawing of one module of the PTD [Mau00].

Every taxel consists of a stamp of 1 mm in diameter which contacts the skin and is driven by a piston of 2.5 mm in diameter (see fig. 3.1). Air pressures between 3 and 7 bar result in a maximum force on the stamp between 1.3 and 2.3 N. The air pressure, and thus the force, can be adjusted by means of the pressure regulator (see fig. 3.2). The stamps are free to move 10 mm in the vertical direction. A taxel is ON when the stamp exceeds its shaft and OFF when it is completely inside. The distance between the skin and the stamp is controlled by a silicon support pad. The area of the pad is much bigger than the contact area of the stamp and should not influence the tactile stimulation.

3.2 Functionality of the PTD

Control of the PTD involves 2 main components: the PTD control unit, basically consisting of pneumatic switches and the electronic interface, and a PC with a digital I/O card (DAQ24) and the Visor software. Figure 3.2 schematically illustrates the PTD system with its components. A picture of the PTD control unit is presented in figure 3.3. Modules fixed on different body parts can be seen in figures 5.3 and 5.4.

The PC is connected to the electronic interface via the DAQ24 card and its appendant cable. There are 13 lines. 8 of them serially submit a line of data each to the electronic interface. The data is in form of an activation pattern or state (Section 3.3). The other 5 lines serve control purposes. One of the lines transmits the trigger signal from the electronic interface to the PC, a second one the trigger error in case of readout failure. The PC transmits a clock, a strobe and a trigger reset to the electronic interface on the remaining 3 lines. The clock describes the timing of the serially submitted data and the strobe ensures simultaneousness.

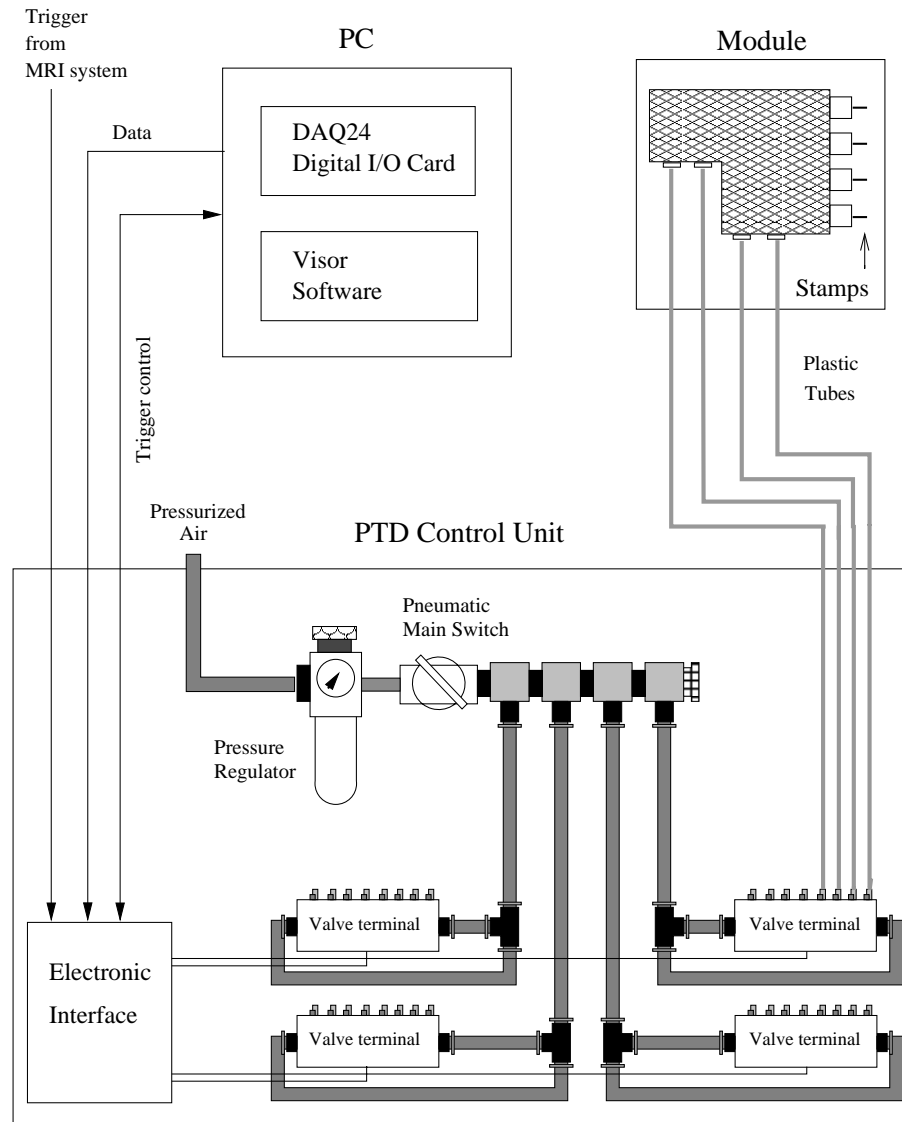


Figure 3.2: Schematic of the PTD system. The electronic interface links the MRI system (trigger), the PC and the PTD. It controls the trigger and transmits the data to the PTD.

The electronic interface is composed of 3 parts. The serial-parallel converter distributes the data that arrives on 8 serial lines to 8×8 parallel ones that forward the data to the pneumatic switches. The serial Transmittor-Transmittor Logic (TTL) level of 5 V is transformed to the standard level of the pneumatic switches of 24 V. The third part is a trigger controller. The electronic interface receives a trigger impulse from the MRI system at the beginning of each image acquisition. If the data has not been read out by the PC when the next trigger arrives a trigger error occurs.

64 pneumatic switches, a pressure regulator and a pneumatic main switch make up the pneumatic 'circuit'. The pressure regulator reduces the air pressure of 8 bar from the

compressor to 3 - 7 bar. 7 bar is the maximum pressure that is compatible with the integrated pneumatic elements. The pneumatic switches are grouped into 4 valve terminals. Each valve terminal consists of 16 pneumatic switches and can thus address 16 taxels (4 modules). Plastic tubes with an inside diameter of 2 mm and 6 m length connect the modules to the valve terminals.

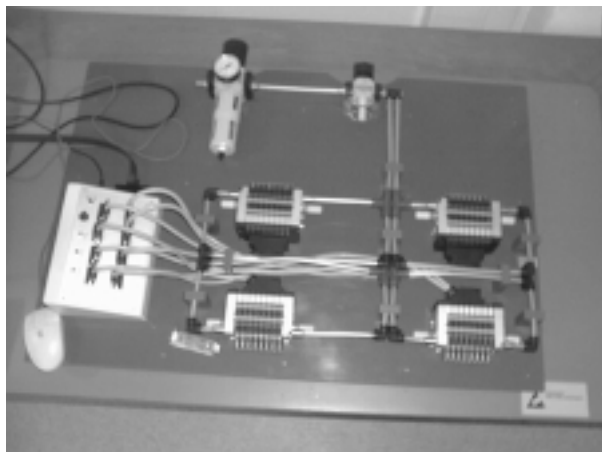


Figure 3.3: A picture of the PTD control unit.

3.3 The Visor software and Pattern Generation

When the electronic interface receives a trigger signal from the MRI, the trigger jumps to high and a signal is transmitted to the PC via the trigger line. The PC returns a trigger reset and a data set with the corresponding clock followed by a strobe signal. Each data set describes one state of the PTD, i. e. which taxels are on and which ones are off. The data is only forwarded to the PTD once the strobe signal has arrived to ensure simultaneity. One PTD state after another is sent to the PTD via the electronic interface with a user definable frequency $f = 1/t$. The maximum frequency that is compatible with the damping of the plastic tubes that connect the PTD to the pneumatic control unit is $f = 20 \text{ Hz}$ ($t = 50 \text{ ms}$). Data transmission itself takes less than two milliseconds. Figure 3.4 illustrates the time scheme of the data transmission.

Pattern generation is controlled by an extension to the Visor software², which was also developed by T. Maucher. Version 1.0 was adapted for a PTD with 4 modules, i. e. 4×4 taxels and is the one that was used in the conducted experiments. The PTD has been extended to 8 modules by now and the software has been upgraded to Version 2.0.

Figure 3.5 shows a screenshot of the Visor software's user interface (V1.0).

The main window of Visor is the pneumatic control window. The options 'on' and

²written by J. Schemmel, Postdoc at the Kirchhoff-Institute for Physics of the University of Heidelberg in the framework of this project

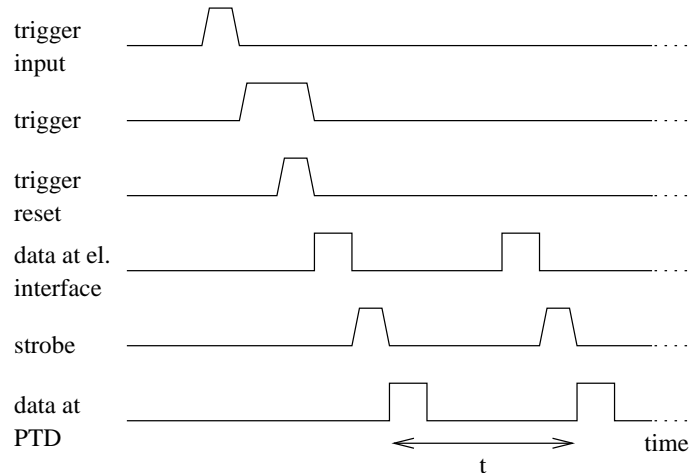


Figure 3.4: Time scheme of data transmission from the PC to the PTD via the electronic interface. The diagram is not to scale. The period t can be defined via the Visor software.

‘off’ set the time during which the stamps of the PTD are on and off in a single period $t=1/\text{‘frequency’}$. The period t corresponds to ‘time/line’ in the pneumatic control window. Additionally a ‘break’ can be added to each period, so the frequency is actually $f = 1/(t + \text{break})$.

The patterns can be entered either manually by choosing ‘manual’ or automatically by choosing ‘prog’ for the ‘data’ option in the image control section. The ‘manual’ input is usually only used for control purposes. The pattern can be defined by means of the ‘manual input’ section. The manual input can also be applied to save a pattern to a file. In most cases a *paradigm file* is employed for automatic pattern generation. The file contains *data lines* of the following format.

Name trigger flags cycles Data1, Data2, ... DataN

Every ‘DataX’ is composed of 4 integers, that describe the state of one module each. DataX = 0 4 0 1 implies that the 3rd taxel of the 2nd module and the 1st taxel of the 4th module are on while all other taxels are off. The data line is repeated until as many trigger signals as are defined by ‘trigger’ have been received. Then the next data line is executed. The number of cycles corresponds to N. Two flags can be set. The first one is either ‘t’ for trigger or ‘c’ for clock. If it is set to ‘c’ the program does not expect any triggers but instead executes each data line as many times as defined by the variable ‘trigger’. If the second flag is ‘y’ for yes the program ignores the ‘DataX’ and instead generates random patterns. Usually specific patterns are called for and this flag is set to ‘n’. Checking the ‘stop pneumatic’ button turns the pneumatic system off.

The ‘personal settings’ window can be used to enter additional information about experiment, the instructor and the subject. This information is added to the log-file that is written after each run. It also contains the ‘start/stop’ option. ‘Stop’ inhibits program execution. The last window depicted in fig. 3.5 serves as a control window.

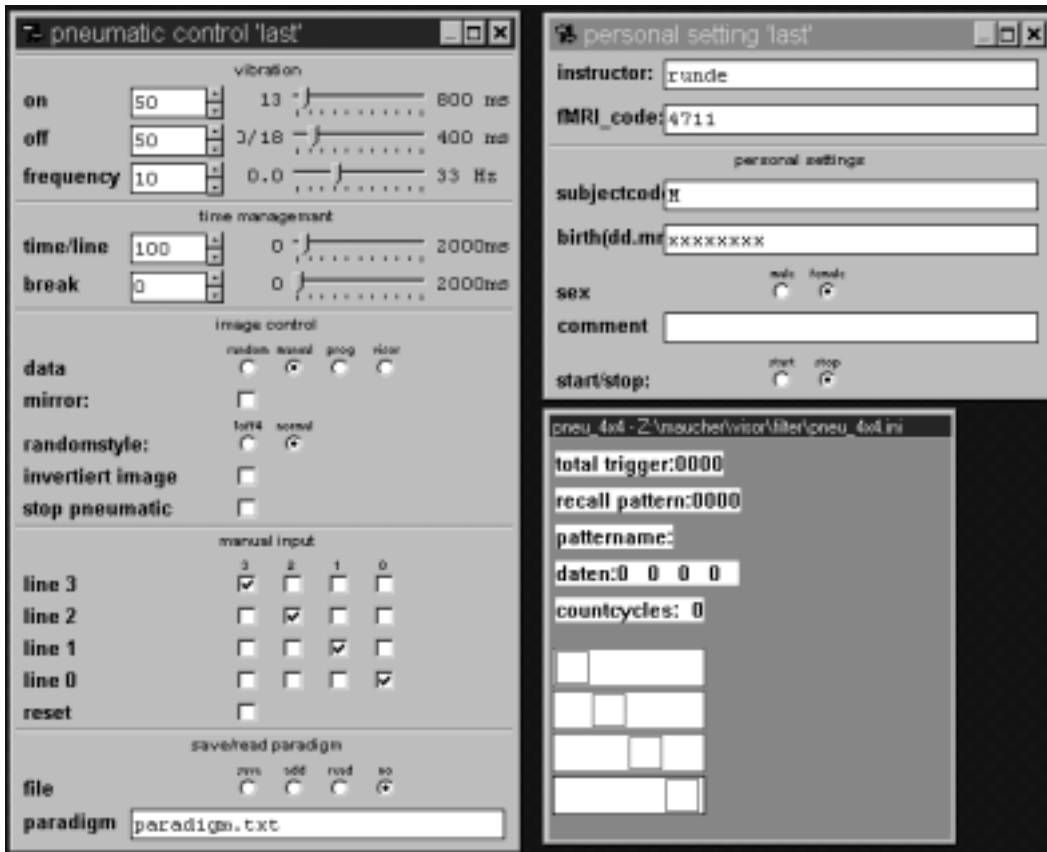


Figure 3.5: Screenshot of the user interface of the Visor software (V1.0) that controls the pattern generation for the PTD.

Chapter 4

Statistical Parametric Mapping

For each of our experiments certain tactile stimuli with a specific timing are presented to the subject by means of the PTD. Every functional brain image acquired with fMRI methods consists of approximately 100 000 *voxels* (volume elements). The signal at every voxel is recorded at N points in time, so there are about 100 000 signals that need to be investigated. The analytical approach that is adopted here is based functional segregation (see section 1.1), i. e. it is expected that a well-defined stimulus causes activation of specific regions of the brain only. It is a univariate method that investigates every voxel separately. One possibility is to calculate the correlation coefficient between the observed and the expected time course. Another approach is implemented by the software-package SPM99 (Wellcome Department of Cognitive Neurology, London, UK) written in MATLAB¹. Here a test of significance, usually a t-test, is applied to each voxel yielding an image of t-scores, a so-called **Statistical Parametric Map**.

Before the actual analysis commences several preprocessing steps are required. Preprocessing steps consist of various spatial transformations that are concerned with mapping one or more images onto a reference image: *Realignment* is done to correct for motion of the subject. *Coregistration* of a morphological image to a functional image series allows for precise localization of an activation in the individual brain. Applying *normalization* a multi-subject analysis can be performed and coordinates can be reported in a reference coordinate system. *Smoothing* ensures the validity of inference and generally enhances the signal to noise ratio (see section 2.4).

A hypothesis about the behaviour of the signals of interest, including possible confounds, needs to be set up. This hypothesis is implemented in the ‘design matrix’ and relies on the **General Linear Model**. Evaluating the model and applying ‘contrasts’ results in Statistical Parametric Maps of t-scores. These SPMs are finally assessed according to the **Random Field Theory**. This means that they are *thresholded* to comply with a certain significance, i. e. in the end it is possible to determine the probability that the residual activations reflect real physiological changes.

¹MathWorks, Inc.

4.1 Preprocessing

In the following an overview of the essential preprocessing steps, namely realignment, between modality coregistration, normalization and smoothing, is given. Figure 4.1 exemplifies the effects of these spatial transformations.

4.1.1 Principles of Spatial Transformations in Brain Imaging

Spatial Transformations in Brain Imaging can be broadly divided into *label based* and *non-label based*. Label based transformations rely on certain landmarks, e. g. anterior and posterior commissures. The superposition of these landmarks is optimized. Non-label based approaches treat both object and reference image as unlabeled continuous objects. These attempts identify a spatial transformation that minimizes some index of difference between the two images, generally the sum of squared differences. The crucial point of both kinds of transformations is to find appropriate constraints according to which they are effected. SPM99 applies only non-label based spatial transformations since they are not limited by the reproducibility of landmarks.

There are two major steps involved in mapping one or more object images to a reference image: *registration* and *transformation*. During registration the parameter values are calculated, that describe the transformation by minimizing the *residual sum of squares* of the difference between the voxel values of the reference and the object image. Transformation requires resampling of the object image(s) which usually involves sampling between the centres of voxels. Hence an interpolation method is needed. In SPM99 sinc interpolation is the preferred higher order interpolation method. Resampling introduces some smoothing of the raw data.

4.1.2 Realignment (Within Modality Coregistration)

In brain imaging the different image acquisition methods or modes are termed ‘modalities’. A PET² image will look very different from a T_1 (MRI) image, which again has much better resolution than a T_2 (MRI) image, etc. Within modality coregistration takes care of mapping object images to a reference image of the same modality.

Movement related variance components in fMRI present one of the most serious confounds of analysis. Hence the most common application of within modality coregistration is motion correction (*realignment*). One image of the functional image series is chosen as the reference image that the other images are realigned to. An additional reason for realignment is that it increases the sensitivity of detecting an activation. The t-test used by SPM99 is based on the signal change relative to the residual variance, which is increased by movement artifacts.

A rigid body registration with 6 parameters (3 for translation and 3 for rotation) is used for realignment in SPM99 (see appendix B.3). The amount of necessary realignment is in general very small (about 1 mm and tenths of degrees), but can nevertheless introduce

²Positron Emission Tomography

serious confounds. The movement of the subject is minimized by taping its head to the head restraint it rests on (see fig. 5.1).

4.1.3 Between Modality Coregistration

Between modality coregistration is used to map images of different modalities onto each other. It is, for example, often desirable to register a structural image (e. g. T_2 -weighted) to a functional image series (EPI). This is again a rigid body transformation but the registration cannot be simply performed by minimizing the residual sum of squares due to the different modalities. In the first step the affine transformations (see appendix B.1), that register the structural image and the first image of the functional image series to template images of the respective modalities, is determined. These transformations are constrained in such a way that only the parameters that describe the rigid body transformation are allowed to differ. Next the images are segmented using probability images (provided by the Montreal Neurological Institute, Canada) of gray matter, white matter and cerebro-spinal fluid. At last the image partitions can be simultaneously coregistered to produce the final solution.

The procedure has been successfully applied to the coregistration of T_1 to T_2 , both T_1 and T_2 to PET and T_2 to EPI. Between modality coregistration of a structural image (T_2) to a functional image series (EPI) is used to accurately localize activation sites of a single subject.

4.1.4 Normalization

In order to allow for comparison of different subjects it is necessary to warp the corresponding images into roughly the same standard space. Spatial normalization is useful for determining what happens generically over individuals. Additionally activation sites from spatially normalized images can be reported in standard Euclidian coordinates within a standard space. The coordinate system adopted by SPM99 is that described by Talairach and Tournoux ([Tal88]) but uses the MNI³ 152 average (ICBM⁴ brain) as a template (see also appendix C.2). This template has been determined by averaging MRI scans of 152 brains yielding an average image that is larger than the one used by Talairach and Tournoux. The Talairach coordinate system uses the **A**nterior **C**ommissure as the origin. Its axes are defined by the line through the superior edge of the AC and the inferior edge of the **P**osterior **C**ommissure - the AC-PC line - and the interhemispheric, sagittal plane (see also appendix C.1). The AC and the PC are fibre tracts that connect the two cerebral hemispheres. The AC connects the middle and the temporal gyri, the PC midbrain and diencephalon structures. Unfortunately it is not possible to perform a proper transformation between the MNI and the Talairach space since the brains vary significantly in shape. This makes it difficult to compare SPM99 results to results reported in Talairach space. Since individual brains vary in shape and size more parameters are needed to describe the

³Montreal Neurological Institute

⁴International Consortium for Brain Mapping

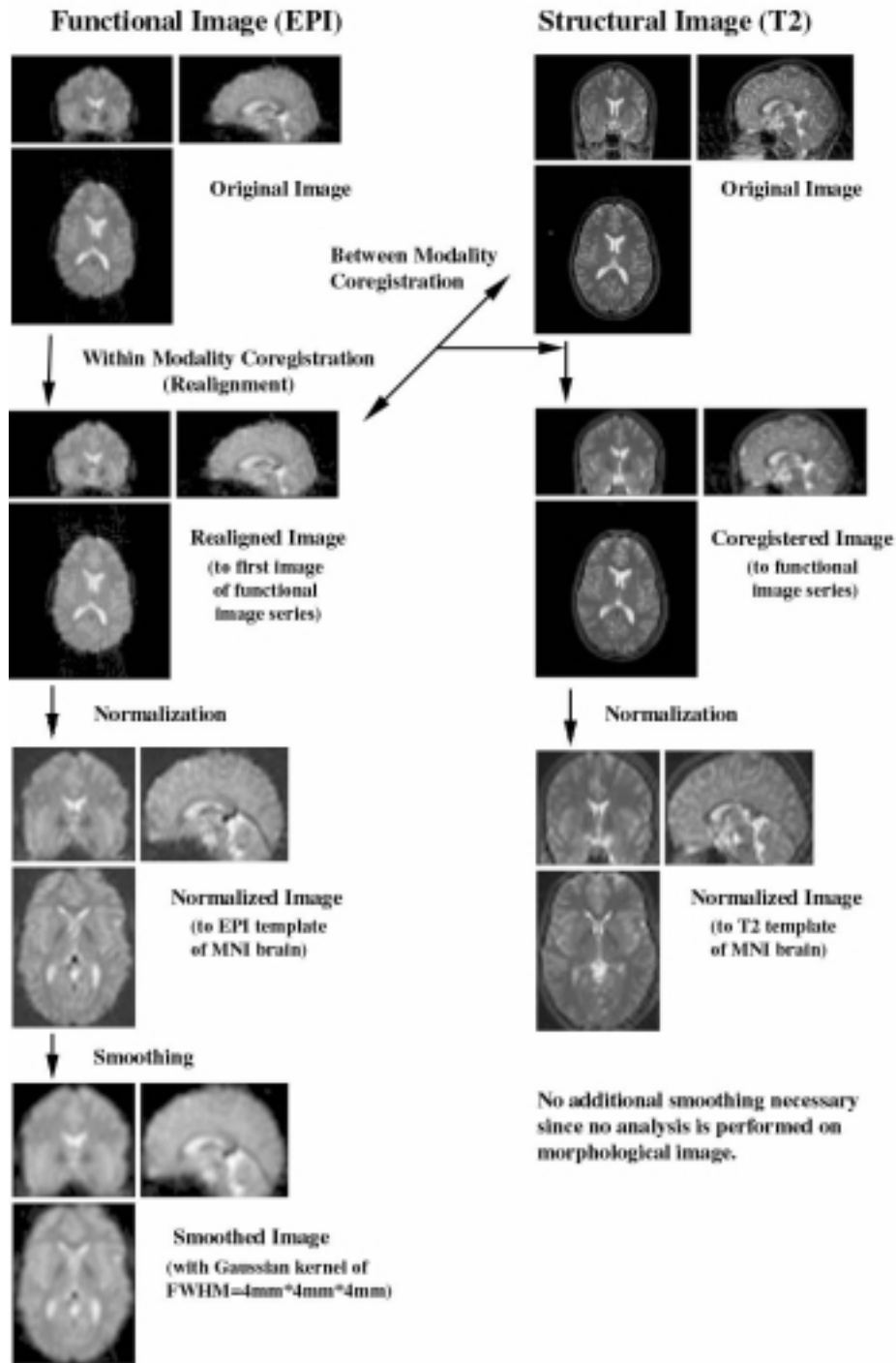


Figure 4.1: Overview of the preprocessing steps involving a functional image series and a corresponding structural image. The depicted sections all pass through the origin. The images (`m1_1_010.img` and `mt2.img`) were taken on 28.6.00 of subject M.

spatial transformation, i. e. a rigid body transformation is not sufficient. The first step in normalization is to correct for the variation in position and size of the image compared to a template image of the same modality. This involves determining the optimum 12 parameter of the affine transformation: 3 for translation, 3 for rotation, 3 for shear and 3 for zoom (see appendix B.4). Optimization is again effected by minimizing the residual sum of squares. The second step corrects more subtle differences by means of a non-linear registration taking into account only smoothly varying deformations. These deformations are modelled by a linear combination of smooth basis functions (see [Fra97], Ch. 3 and [SPM97], Ch. 2).

4.1.5 Smoothing

Some smoothing of the raw data is intrinsically introduced by resampling the images as has been mentioned above. Additional smoothing is done by convoluting the data with a Gaussian kernel. Now inferences about the data can be drawn using Gaussian Random Field Theory. In particular thresholding can be performed by correcting with the Euler Characteristic instead of the Bonferroni correction, which is more conservative.

Smoothing also potentially increases signal to noise according to the matched filter theorem ([Ros82]). This theorem states that the filter that will give optimum resolution of signal from noise is a filter that is matched to the signal. Usually neither exact size nor shape of the signal are known. A rule of thumb for fMRI signals is to try a Gaussian kernel of FWHM of about 2 to 3 times the voxel size.

4.2 Statistical Models

4.2.1 The General Linear Model

In physics the **General Linear Model** is widely known as regression analysis, the most simple form of which is the linear regression $Y_j = \beta x_j + \mu + e_j$. An experiment yields a time series of N observations Y_j acquired at times t_j at every voxel, where $j = 1 \dots N$ is the scan number. For fMRI brain images every observation relates to the blood oxygenation level. The approach of the GLM is to model the observed time series at every voxel as a linear combination of L explanatory functions $f^l(t_j)$ plus a residual error or ‘noise’ term:

$$Y_j = f^1(t_j) \beta_1 + \dots + f^l(t_j) \beta_l + \dots + f^L(t_j) \beta_L + e_j \quad (4.1)$$

The basis functions $f^1(t_j), \dots, f^L(t_j)$ are chosen so that they span the space of possible fMRI responses. The β_l are the unknown parameters that Eqn. 4.1 needs to be solved for. The errors e_j are assumed to be independent and identically distributed normal random variables with zero mean. Equation 4.1 can be expressed in matrix form:

$$\begin{pmatrix} Y_1 \\ \vdots \\ Y_j \\ \vdots \\ Y_N \end{pmatrix} = \begin{pmatrix} f^1(t_1) & \dots & f^l(t_1) & \dots & f^L(t_1) \\ \vdots & \ddots & \vdots & \ddots & \vdots \\ f^1(t_j) & \dots & f^l(t_j) & \dots & f^L(t_j) \\ \vdots & \ddots & \vdots & \ddots & \vdots \\ f^1(t_N) & \dots & f^l(t_N) & \dots & f^L(t_N) \end{pmatrix} \begin{pmatrix} \beta_1 \\ \vdots \\ \beta_l \\ \vdots \\ \beta_L \end{pmatrix} + \begin{pmatrix} e_1 \\ \vdots \\ e_l \\ \vdots \\ e_L \end{pmatrix} \quad (4.2)$$

The matrix $\mathbf{X} = \{x_{jl}\}$ is the *design matrix* (see section 4.3.1). Its columns are the discretized basis functions. interest and effects of no interest respectively.

The number of basis functions L is usually less than the number of observations N (for the conducted experiments $N=200$), i. e. the problem is overdetermined. Thus the simultaneous equations implied by the GLM cannot be solved so the parameters that best fit the data are estimated by - again - minimizing the residual sum of squares⁵ S .

$$S = \sum_{j=1}^N e_j^2 = \sum_{j=1}^N (Y_j - f^1(t_j) \beta_1 - \dots - f^L(t_j) \beta_L)^2 \quad (4.3)$$

$$\frac{\partial S}{\partial \beta_l} = 2 \cdot \sum_{j=1}^N -f^l(t_j) (Y_j - f^1(t_j) \beta_1 - \dots - f^L(t_j) \beta_L) = 0 \quad \forall \beta_l \quad (4.4)$$

$$\Rightarrow \vec{\beta} = (\mathbf{X}^T \mathbf{X})^{-1} \mathbf{X}^T \vec{Y} \quad (4.5)$$

Every voxel in the analyzed brain volume is now attributed a parameter set $\vec{\beta}$. For every component β_i a separate image is created by SPM99 called ‘beta_000i.img’.

⁵The values of the residual sums of squares are saved as ‘ResMS.img’ in SPM99.

4.2.2 Low Frequency Confounds

Low frequency confounds such as baseline drifts and aliased cardiac and respiratory effects (see section 2.5.2) are modelled in the design matrix by means of the high-pass filter. The design matrix is extended by R columns. A suitable set of basis functions for the high-pass filter are discrete cosine functions of the form

$$f_r(t) = \cos\left(r\pi \cdot \frac{t - t_1}{t_N - t_1}\right)$$

where $t_1 \cdots t_N$ are the acquisition times of the N scans. The index r ranges from 1, which gives a half cosine cycle, to a user specified maximum R. The cut-off R should be chosen such that the period of $f_r(t)$ is below that of the experimental design. Choosing a cut-off of twice the period of the experimental design ensures that the signal is not accidentally modelled as a confound, i. e. filtered out. The name 'high-pass filter' is somewhat misleading for it does not eliminate the low frequencies but instead includes them in the model.

4.2.3 t-Test

The t-test (also known as Student t-test) is concerned with making inferences about a sample mean \hat{x} for a small number of observations. Assume we draw a simple random sample from a normally distributed population $N(\mu, \sigma^2)$ and calculate the mean \hat{x} and the standard error s. By means of the t-test it is possible to determine the probability of getting a certain value for the mean [Bor99]. The t-statistic with n-1 degrees of freedom (df) is given by equation (4.6).

$$t = \frac{\hat{x} - \mu}{s/\sqrt{n}} \quad (4.6)$$

The shape of the t-distribution depends on the degrees of freedom (\sim sample size) and approaches the normal distribution for $df \rightarrow \infty$ (fig. 4.2).

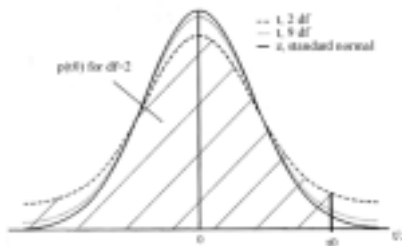


Figure 4.2: The t-distribution approaches the normal distribution (z) for large degrees of freedom or many observations [Moo95].

A certain t_0 yields the probability p of getting a value $t \geq t_0$.

By means of the least squares method every voxel is assigned a parameter estimate $\vec{\beta}$.

These are normally distributed according to $N(\vec{\beta}, \hat{\sigma}^2)$. Linear compounds called *contrasts* $\vec{c}^T \vec{\beta}$ (section 4.2.4) are also normally distributed as $N(\vec{c}^T \vec{\beta}, \hat{\sigma}^2 \vec{c}^T (X^T X)^{-1} \vec{c})$ where \vec{c} is a column vector of the same length as $\vec{\beta}$.

The residual variance σ^2 is estimated by the *residual mean square* $\hat{\sigma}^2$, the residual sum of squares divided by the appropriate degrees of freedom:

$$\hat{\sigma}^2 = \frac{\vec{e}^2}{N - p} \quad p - \text{Rank}(X) \quad (4.7)$$

The t-statistic (4.8) yields a t-distribution with $df = N - p$.

$$t_{N-p} \sim \frac{\vec{c}^T \vec{\beta} - \vec{c}^T \hat{\vec{\beta}}}{\sqrt{\hat{\sigma}^2 \vec{c}^T (X^T X)^{-1} \vec{c}}} \quad (4.8)$$

This is the t-test used by SPM99, which is based on the signal change relative to the residual variance.

4.2.4 Contrasts

To understand contrasting in SPM99 it is important to note that the software distinguishes between ‘effects of interest’ and ‘effects of no interest’. The effects of interest comprise only those parameters that describe the ideal signal, e. g. the heights of the box-car functions. Additionally some regressors can be modelled as effects of interest (see section 4.3.1). Everything else (offset, high-pass filter, etc.) is modelled as effects of no interest.

Hypotheses $d = \vec{c}^T \vec{\beta}$ can be assessed by means of different column vectors \vec{c} . These are subject to certain restrictions (see [SPM97], Ch. 3). Contrast weights are requested only for the parameters of interest, weights for other parameters are set to zero. For the designs implemented in SPM99, the contrast weights must sum to zero with the exception of a design with one effect of interest. The latter design can search for activated voxels via $\vec{c} = [1 \ 0]$ and for deactivated ones via $\vec{c} = [-1 \ 0]$. A design with 2 effects of interest (E1 & E2) can be assessed with $\vec{c}^T = [1 \ -1 \ 0]$ and $\vec{c}^T = [-1 \ 1 \ 0]$. These correspond to a search for voxels that are activated during E1 and deactivated during E2 and those that behave vice versa.

Having chosen an appropriate contrast and calculated the corresponding t-value for every voxel the result is a statistical parametric map of t-values. SPM99 creates an image of every SPM{t} called `spmT_000i.img` where `i` corresponds to the numbering of the contrast. The contrast values are also saved in `con_000i.img`.

4.2.5 Inference

4.2.5.1 Hypothesis Testing

The reasoning of Hypthesis Testing is the following. The Null Hypothesis H_0 is that a given sample behaves just like the entire population. For comparing means this implies that the sample mean does not deviate from the population mean. The Alternative Hypothesis H_a expects a certain divergence, i. e. a larger or a smaller sample mean. For the t-test this means that a t-statistic t_0 with its corresponding p-value (fig. 4.2) has a probability p to have occurred by chance and of $(1-p)$ to reflect a real change. Thus applying a threshold of $p = p_0$ to a collection of t-scores filters those values that have a probability of $(1-p)$ to be false positives. The appropriate choice of threshold is critical as will be explained in the next sections.

4.2.5.2 The Multiple Comparison Problem

In a typical SPM of t-statistics (SPM{t}) there are about 100 000 values, one for each voxel. Now, even if H_0 is true some t-scores will appear to be significant at a standard statistical threshold, e. g. $p=0.05$ simply because there are so many. The multiple comparison problem is the question of how high the threshold needs to be to ensure reasonable confidence in the significance of the residual t-scores.

4.2.5.3 Bonferroni Correction

The traditional way to correct for the multiple comparison problem is to apply a Bonferroni Correction (BC). Here a certain rate of false positives α that are to be accepted is given, typically $\alpha = 0.05$, i. e. one of 20 ‘activations’ may be just by chance. The BC then yields a threshold of $p = \frac{\alpha}{\text{number of tests}}$. Unfortunately the Bonferroni Correction can only be applied to independent scores. This is not given for fMRI data since there is strong spatial correlation. Spatial correlations in statistical parametric maps are caused by several factors:

- Due to low resolution an individual voxel will contain some signal from the surrounding tissue.
- Resampling during realignment and normalisation causes some smoothing.
- Most analyses work on smoothed images.

For correlated data the Bonferroni Correction is far too conservative and would wipe out real ‘activations’.

4.2.5.4 Random Field Theory and Euler Characteristic

An appropriate correction of the multiple comparison problem for spatially correlated data requires an estimation of the degree of correlation. The approach adapted by SPM99 is to use **Random Field Theory**. Three basic steps are involved in the application of RFT: Determining the number of **RESolution ELeMents** in an image, working out the **Euler**

Characteristic for different thresholds and finally using the expected EC to correct the threshold for the required control of false positives.

A RESEL is defined as a block of voxels of the same size as the FWHM of the smoothness of the image. The number of RESELS can be regarded as an estimate of the number of independent observations in an image. The number of RESELS depends mainly on the number of voxels and the FWHM but also on the shape and the volume of the image. In SPM99 the smoothness of the image is not equivalent to the FWHM of the smoothing kernel but is instead calculated from the residuals of the statistical analysis.

The Euler Characteristic is a property of the image after it has been thresholded. The EC can be thought of as the number of ‘activities’ surviving the threshold. At any given threshold the EC can be estimated if the number of RESELS in the image and the shape of the volume containing the voxels is known ([Wor96]). The EC’s dependence of the vol-

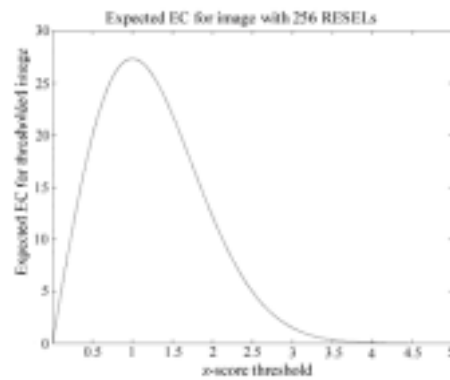


Figure 4.3: The Euler Characteristic as a function of threshold z for an image of 256 RESELS [Bre99].

ume’s shape is significant only for small volumes and can be neglected when the FWHM is small compared to the volume. Fig. 4.3 depicts the expected EC for a thresholded image as a function of the threshold z , where z refers to the standard normal distribution. T-scores are easily converted into z-scores using a voxel by voxel t-to-z probability transformation such that $\Phi(z) = \Psi(t)$ where Φ is the standard normal distribution and Ψ the t-distribution

The expected EC is a good estimate of the probability of observing one or more ‘activities’ at the given threshold. Any remaining ‘activities’ after an applied threshold x that gives an expected EC of $p = 0.05$ can be said to have a probability of 5% or less to have occurred by chance.

4.3 Using SPM99 for Statistical Analysis

4.3.1 Setting up a Design Matrix in SPM99

SPM99 distinguishes between ‘effects of interest’ and ‘effects of no interest’ as already mentioned in section 4.2.4. In general, confounds are modelled as effects of no interest, e. g. the high-pass filter, while the functions whose linear combinations make up the ‘ideal’ signal as well as additional parameters and regressors are effects of interest. Additional parameters can be used to model e. g. a linear reduction in the signal due to adaptation. Regressors can be applied to model motion effects rather than correct for them by means of realignment. The design matrix is specified in SPM99 via the ‘fMRI models’ button in the section ‘model specification & parameter estimation’. SPM99 saves the design matrix and related information by writing two MATLAB-variable files `SPMcfg.mat` and `SPM_fMRIdeSMtx.mat`. `SPM_fMRIdeSMtx.mat` contains the actual design matrix in the variable `xX.X` while `SPMcfg.mat` stores additional information like the exact user input, filenames, etc.

The simple experimental design presented in this section serves to exemplify the implementation of the GLM in SPM99. It consists of an ‘active phase’ during which a stimulus is presented to the subject and of a ‘compare phase’ during which the subject is at rest. Each phase lasts for 10 scans and each scan takes 3.9 s (= TR). In total 200 images are taken. The expected time course at an activated voxel will basically be of a box-car shape but lagged by one image due to the slow onset of the haemodynamic response function. SPM99 models the rest phase as an effect of no interest or an offset with $\{f^2(t_j)\} = 1 \quad \forall j$ while the active phase corresponds to a box-car function with mean zero and is an effect of interest. The parameters to be estimated β_1 and β_2 reflect the amplitude of the box-car and a offset that is of no interest. Without modeling any confounds, additional parameters or regressors the design matrix in SPM99 will be as follows:

$$\begin{pmatrix} Y_1 \\ Y_2 \\ \vdots \\ Y_{11} \\ Y_{12} \\ \vdots \\ Y_{21} \\ \vdots \\ Y_{200} \end{pmatrix} = \begin{pmatrix} -0.5 & 1 \\ +0.5 & \\ \vdots & \\ +0.5 & \\ -0.5 & \vdots \\ \vdots & \\ -0.5 & \\ \vdots & \\ 1 & \end{pmatrix} \begin{pmatrix} \beta_1 \\ \beta_2 \end{pmatrix} + \begin{pmatrix} e_1 \\ \vdots \\ e_L \end{pmatrix} \quad (4.9)$$

The following table lists the SPM99 prompts with the corresponding user specifications for the given experimental design. In addition further modeling options are explained.

SPM99 prompt	Variable	Comment
What would you like to do?	specify and estimate a model	Seperate specification and estimation is possible.
<i>Scans and sessions...</i>		
Number of sessions...	1	
Select scans for session 1 ..		
Interscan Interval {sec}	3.9	This is the repetition time (TR).
<i>Session 1/1</i>		
Number of conditions or trials	1	SPM99 only counts the effects of interest.
Name for condition/trial 1	trial 1	
<i>Trial specification</i>		
SOA	variable	SOA = Sequence Of Analyse; if 'fixed' this corresponds to the period of the design.
Vector of onsets {scans} - trial 1	1:20:200	MATLAB code for [1 21 41 ... 181]; a non-lagged function would start with 0.
Variable durations?	no	The active phase is always of the same length.
<i>Parametric specification</i>		
parametric modulation	none	This could be used to model e. g. adaptation to stimulus.
<i>Session 1/1: trial 1</i>		
Are these trials events or epochs?	epochs	Each phase lasts for $10 \cdot 3.9$ s; long-lasting stimuli like this are epochs.
Select type of response	fixed response (box-car)	
Convolve with hrf?	yes	The box-car shaped function is convoluted with the hrf; this is not really necessary for long epochs.
Add temporal derivatives?	no	
Epoch length {scans} for trial 1	10	This is how long the active phase lasts; the length of the rest phase is then calculated taking the SOA into account.

<i>Design matrix options</i>		
Interaction among trials (Volterra)?	no	No interaction can take place as there is only one trial
<i>Other regressors...</i>		
User specified regressors	0	This could be used to model e. g. the realignment parameters as confounds.
<i>Global intensity normalization...</i>		
Remove global effects?	none	Baseline drifts are modelled by the high-pass filter.
<i>Temporal autocorrelation options</i>		
High-pass filter	specify	The high-pass filter corrects mainly for baseline drifts, cardiac and respiratory effects.
Session cutoff period {sec}	156	This is twice the experimental period.
Low-pass filter	none	
Model intrinsic correlations	none	
<i>Estimation options</i>		
Setup trial-specific F-contrast?	no	Only the t-test is used for the conducted experiments.
Estimate	now	or later

4.3.2 Using the Thresholding Function in SPM99

Thresholding of the SPM $\{t\}$ s is done using the ‘Results’ button in the ‘statistical inference’ section. Both a height threshold p_0 and a spatial extent threshold k can be set. With the spatial extent threshold a minimum cluster size k (in voxels) is defined [Fri94b], i. e. only clusters that consists of at least k voxels above p_0 survive the threshold. A cluster is specified with an 18 connectivity scheme. SPM99 prompts for a corrected or an uncorrected threshold. Choosing ‘corrected’ is followed by entering the expected EC, i. e. the rate of false positives one is prepared to accept. For the ‘uncorrected’ threshold the EC is calculated but thresholding is employed without correcting for the multiple comparison problem.

4.3.3 Automatisation of the Analysis

SPM99 can also be run in batch mode. The preprocessing options as well as design matrix and contrasts can be entered as nested structures. A short script performs the requested steps falling back on these structures. Even though the batch mode is still in beta-testing and has a few problems it nevertheless saves a lot of tedious parameter specification with the user interface. In trying to get the batch mode to work several problems occurred. The SPM99 analysis of these experiments has been performed using a network that comprises a Sun Solaris and a HP Unix workstation as well as a Linux PC. Working with certain programs (nedit or netscape) on the linux PC changes the keybindings and the batch-files won't work any more. SPM99 also seems to have problems with certain directory structures. It is not possible to start the batch scripts from the directory they are filed in. The structures that the batch modus relies on are poorly documented. There are a few example files, but some of them are corrupt. The second source of information is the SPM99 help function, but it is incomplete and very brief.

The batch modus can be started with 'spm_bch('directory/batch-script.m','FMRI')'. The following file 'analyses.m' is an example for the script that coordinates the analysis with SPM99.

analysis.m

```
%-----
% user variables defined here
%-----

tp=[3 6 8 7 8 1 2 1 2];
ix=[1 1 1 1 1 1 1 2 1];
wd=[1 1 1 1 1 2 2 3 3];
mf=[1 2 2 3 3 4 4 4 4];

%-----
% batch variables defined here for analyses
%-----

analyses = struct('type',      tp, ...
                  'index',    ix, ...
                  'work_dir', wd, ...
                  'mfile',    mf );

%-----

type = {'model', 'contrasts', 'defaults_edit', 'headers', ...
        'means', 'realignment', 'normalisation', 'smooth'};

%-----

work_dir = {'/misctmp/vision/ex_28jun00/m1.1/', ...
            '/misctmp/vision/ex_28jun00/RESULTS/m1.1/sr', ...
            '/misctmp/vision/ex_28jun00/RESULTS/m1.1/snr'};
```

```

%-----
mfile = {'/misc/tmp/vision/ex_28jun00/RESULTS/batch/defaults.m',...
        '/misc/tmp/vision/ex_28jun00/RESULTS/batch/prepro1.m',...
        '/misc/tmp/vision/ex_28jun00/RESULTS/batch/prepro2.m',...
        '/misc/tmp/vision/ex_28jun00/RESULTS/batch/stat.m'};

```

The structure `analysis` is successively evaluated. Its components are row vectors that contain indices into the structures `type`, `work_dir` and `mfile`. The component `index` contains indices into the structures that are defined in the MATLAB files (m-files) specified by `mf` and are of the type indicated by the corresponding element of `tp`. The structure `work_dir` indicates which directory the results are to be written to.

The m-files are listed in full in appendix D. In the given example the m-file 'defaults.m' contains a main structure `defaults_edit` that is again composed of indices into the structures that are responsible for the different default settings. The m-file 'prepro1.m' comprises the structures `realign` and `smooth` that define the parameters that need to be specified for realignment and smoothing. For the second type of preprocessing the realigned files are also normalized and smoothed afterwards. The corresponding parameters are contained in the structures `normalize` and `smooth` from m-file 'prepro2.m'. The design matrices are specified in 'stat.m'. There are two instances of the structure `model`. The first one takes care of the first design matrix that models the realigned and smoothed data (sr-data). The second one contains the parameters for the model for the snr-data. Additionally a structure `contrasts` is embodied in 'stat.m' that specifies the contrast to be applied.

The main script 'analyses.m' hence first sets the relevant defaults and performs the first kind of preprocessing, i. e. realignment and smoothing (sr) on a set of raw data. In the next step the second kind of preprocessing is done by taking the realigned scans, which are first normalized and afterwards smoothed (resulting in snr-data). After the preprocessing steps have been performed the design matrix and contrasts for the sr-data and the snr-data are defined successively. It is to be noted that the index for the second design matrix is 2. This means the second instance of the structure `model` is in charge.

Chapter 5

Experiments

Three fMRI experiments using single modules of PTD are reported in this chapter with the aim to investigate the processing of tactile stimulation in the human brain for the seeing subjects. In the first experiment the somatosensory homunculus is mapped for one male subject in three sessions at three distinct points: the index finger, the arm and the foot. The same subject is also imaged during a motor task with the index finger to compare the tactile to a motor stimulation. During the ‘rest’ or ‘compare’ phases of the sessions with this subject another motor task is performed with the contralateral index finger. By this ‘compare’ motor stimulation the reproducibility of motor activation is probed.

In the second experiment both index finger and foot are alternately stimulated in every session. There were two subjects and six sessions for each subject. The main goal of this experiment is to examine the reproducibility of tactile stimulation. A frequency encoding is applied to the sessions to examine whether the tactile stimulation is related to the frequency. An intersubject analysis is finally performed on the three subjects to investigate reproducibility of tactile activations across subjects. Another experiment with a dummy brain serves to ensure that the PTD does not perturb the MRI image acquisition.

5.1 Experimental Setup

5.1.1 Subjects and Experimental Setting

All experiments were performed with the MRI scanner of the Biological Physics Institute of the Faculty of Medicine at the University Louis Pasteur in Strasbourg, France that is described in section 2.6. Only single modules were mounted on index finger, arm and foot of the subjects. The PTD control unit and the laptop with the are situated about 2 m away from the MRI magnet. Pressurized air is provided by a compressor that is placed outside the building. The MRI system provides the trigger signals. There is one trigger at the beginning of each image acquisition process. To account for saturation three dummy images are made before the first image is taken [Mau00]. MRI image acquisition is controlled from an adjacent room.



Figure 5.1: A blindfolded subject equipped with ear plugs and headphones. The head is taped to the head restraint.

The volunteers are blindfolded to restrict visual stimulation to a minimum. As the coils of the magnet cause a lot of noise the subjects are equipped with ear plugs and headphones. The headphones can also be used to talk to the subjects. In order to minimize movement the volunteer's head is taped to the head restraint it rests on. Figure 5.1 depicts a blindfolded volunteer with his head fixed to the head restraint and the headphones. Every subject holds a so-called 'panic ball' while it is in the MRI tube. When the subject squeezes the panic ball an alarm goes off and the subject is immediately pulled out of the tube.

5.1.2 Mounting of the modules

Mounting the modules turned out to be more critical than expected. For the experiments that involved the index finger the module was inserted in a Styrofoam box. The subject's arm lies on an arm rest and its hand is fixed to the Styrofoam box in such a way that the module is right underneath the index finger. Figure 5.2 depicts subject M with her right hand fixed to the Styrofoam box with fabric straps. For the arm and the foot stimulations a square piece of teflon coated cardboard was attached to the module. It was then mounted on the arm/foot with fabric straps as is depicted in figures 5.3 and 5.4.



Figure 5.2: For tactile stimulation of the index finger, the module is inserted in a Styrofoam box.

Great care was taken not to evoke any motor responses from the subject since motor activity generally produces stronger signals in the brain than tactile stimulation does. A motor activity might complicate the detection of the brain activation induced by tactile stimulation for two reasons. One is that motor and somatosensory cortex are very close together. The other is that it makes the detection of the tactile activations more difficult. A motor activation of the brain is not only elicited by real movement of a body part but also by the mere urge to move. If the subject feels uncomfortable with the mounted module or has to exert itself to keep the stimulated limb in place, activation of the motor cortex will most likely result. The tightness of the straps is crucial for all sessions. If the straps are too tight a constant

tactile stimulation is likely to take place. This could reduce the brain activation gradient between the rest state and the actual stimulation. Since an alternation of stimulation/no stimulation is essential to the analysis this would reduce the significance of the activations. If the straps are too loose the module is unstable. Feedback from the subject is required for appropriate mounting of the module.

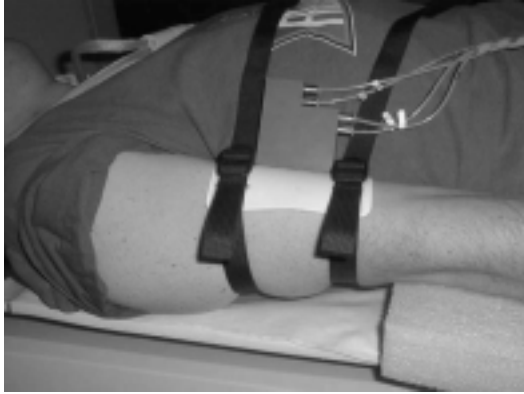


Figure 5.3: A module mounted on the right upper arm of subject F.



Figure 5.4: A module mounted on the instep of subject F's right foot.

5.2 Mapping SI for One Subject

5.2.1 Experimental Procedure

The first fMRI experiment performed aimed to map the somatosensory homunculus at 3 distinct points for one subject (F) using the PTD. Subject F is a 30 years old healthy male. For sake of the subject's comfort the mapping was restricted to the upper part of the homunculus omitting the facial region. Since the spatial resolution of fMRI is limited by the BOLD effect the 3 stimulation points were chosen with regard to maximum separation in the somatosensory homunculus. Foot and index finger are farthest apart and the arm is located in between (see fig. 1.6). Hence one module was successively mounted on the right index finger, the right upper arm and the medial side of the right foot's instep during sessions 1, 2 and 3 (see section 5.1.2). Great care was taken to fasten the modules in a comfortable manner. The PTD was operated at an air pressure of 4 bar.

For each session 200 EPI images were taken with a TR of 3.9 seconds. Every brain volume was recorded in 26 slices of 5 mm thickness with no gap. A field of view of 25 cm and a slice resolution of 64×64 voxels yield a voxel size of $1 \text{ vx} = 3.9 \text{ mm} \times 3.9 \text{ mm} \times 5 \text{ mm}$. In addition a structural T_2 scan with a resolution of $128 \times 128 \times 80 \text{ vx}$ and a voxel size of $1 \text{ vx} = 2 \text{ mm} \times 2 \text{ mm} \times 2 \text{ mm}$ was taken.

The experimental design is identical for the 3 sessions. It consists on an 'active' and a 'compare' phase, each one lasting for 10 images. During the active phase the subject was presented with a walking pattern stimulus. Since it is essential to maintain the subject's

concentration it is presented with a task. The frequency of the walking pattern is varied pseudo-randomly from one active phase to the next one. There is a ‘target’ frequency of 1 Hz and a ‘distractor’ frequency of 0.8 Hz. For a walking pattern of frequency $f_{wp} = 1$ Hz each taxel is successively on for 200 ms each followed by a 200 ms break. During the first two trials the subject is knowingly presented with the target frequency. For the following trials the volunteer is asked to count how many times the target appears. During the compare phase the PTD module is turned off. The subject silently lists the days of the week backwards to help keep the subject’s concentration. Tapping its left index finger simultaneously constitutes a robust motor task for reference purposes and to give a first estimate of reproducibility of motor activation.

5.2.2 SPM Analysis

Preprocessing, Model and Threshold

Preprocessing of the data comprises realignment and smoothing. The brain volumes of all sessions are realigned to the first image of session 2 (arm). Additionally the structural T_2 image is coregistered to the realigned functional image series. Smoothing is done with a Gaussian kernel of $FWHM = 8 \text{ mm} \times 8 \text{ mm} \times 10 \text{ mm}$. Coordinates are reported in an individual coordinate system with its origin at the anterior commissure. The coordinates are used only for determining the relative positions of clusters. It contains no direct information about the anatomical location of the activation. The first column of the design matrix consists of a box-car function lagged by one image to account for the slow rise of the haemodynamic response function. Additionally it is convoluted with the hrf and a high-pass filter (see section 4.2.2) is applied. The second column contains the offset that is of no interest. Evaluating the three functional image series with this design matrix results in 2 parameter images for each experiment. The approximated amplitudes of the fitted box-car functions make up the first one (`beta_0001.img`). The second image is made up of the offsets (`beta_0002.img`). A contrast $\vec{c} = [1 \ 0]$ yields the activations during the active phases. Thereby statistical parametric maps of t-scores are generated that reflect the similarity of the fitted box-car function to the modelled box-car function (see section 4.2.3). Thresholding of these $SPM\{t\}$ s is done at a corrected $p = 0.001$ and a spatial extent $k = 5 \text{ vx}$. All activities that remain after this threshold has been applied can be said to have a probability of less than 0.1 % to have occurred by chance (see section 4.2.5.4).

Detected Brain Activity

Figure 5.5 shows ‘glass’ brain coordinate systems (see also appendix C.1) with projections of all activity clusters that are significant at this threshold for each session. This is how results are typically presented in SPM99. The glass brains are not adapted to the individual coordinate system that the clusters are reported in. They represent the MNI coordinate system. Hence the clusters that occur close to the brain’s surface are placed much lower in the glass brain. Normalized data (see section 4.1.4) would instead match

the glass brain MNI coordinate system. The glass brains from SPM99's result section are interactive, i. e. the spatial pointer can be place on a particular cluster to help locate it in space and extract its coordinates. Additionally a list of the coordinates of the maximum t-scores in each depicted cluster can be printed. With non-normalized data this presentation is only useful to get a first impression of the location of the clusters and their relative positions.

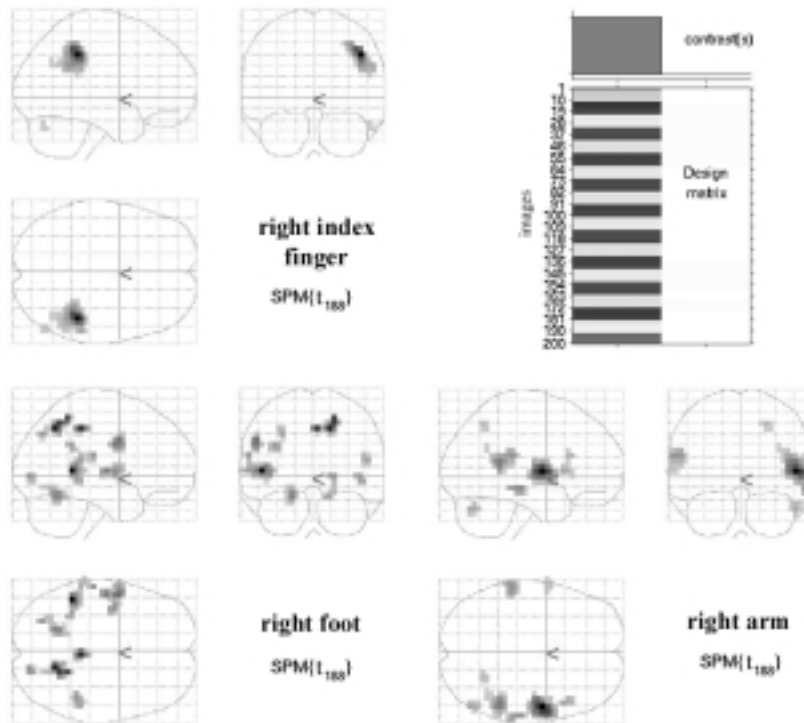


Figure 5.5: Glass brain coordinate systems with projections of activity clusters are the typical SPM99 output. For subject F, sessions 1, 2 and 3, contrasted for the active phase, a threshold of $p_{\text{corr}}=0.001$ and $k=5 \text{ vx}$ is applied. The design matrix as it is represented in SPM99 is depicted in the right upper corner. The greyscale represents the values of the column entries.

In the main region of interest (primary somatosensory cortex SI on the contralateral cerebral hemisphere) the given threshold yields a large cluster of 101 voxels with a maximum $t=16.3$ at $(44, -40, 40)$ for session 1 (index). Several activity clusters survive the threshold for sessions 2 and 3. For session 3 (foot) two highly significant clusters appear in the proximity of the region of interest. The first one exhibits a maximum $t=8.81$ at $(16, -60, 45)$ and spans 21 voxels. It is located medial (smaller x) and posterior (smaller y) to the index activity cluster as expected from the somatosensory homunculus. Close by there is a second cluster of 11 voxels with a maximum $t=8.65$ at $(4, -36, 45)$. It is anterior both to the first foot and the index activity clusters and probably corresponds to the primary motor cortex MI. For session 3 this threshold results in a small cluster of 7 voxels

with a maximum $t = 6.31$ at $(24, -60, 50)$ and a second more significant one with $t = 8.25$ at $(48, -44, 15)$. While the first cluster is very close to the first foot activity cluster and thus probably corresponds to the arm representation of the somatosensory homunculus, the second one might reflect activation of SII. The small size of the first ‘arm cluster’ is not surprising since the representation of the arm in the somatosensory homunculus (see fig. 1.6) is also relatively small.

Mapping of Brain Activity

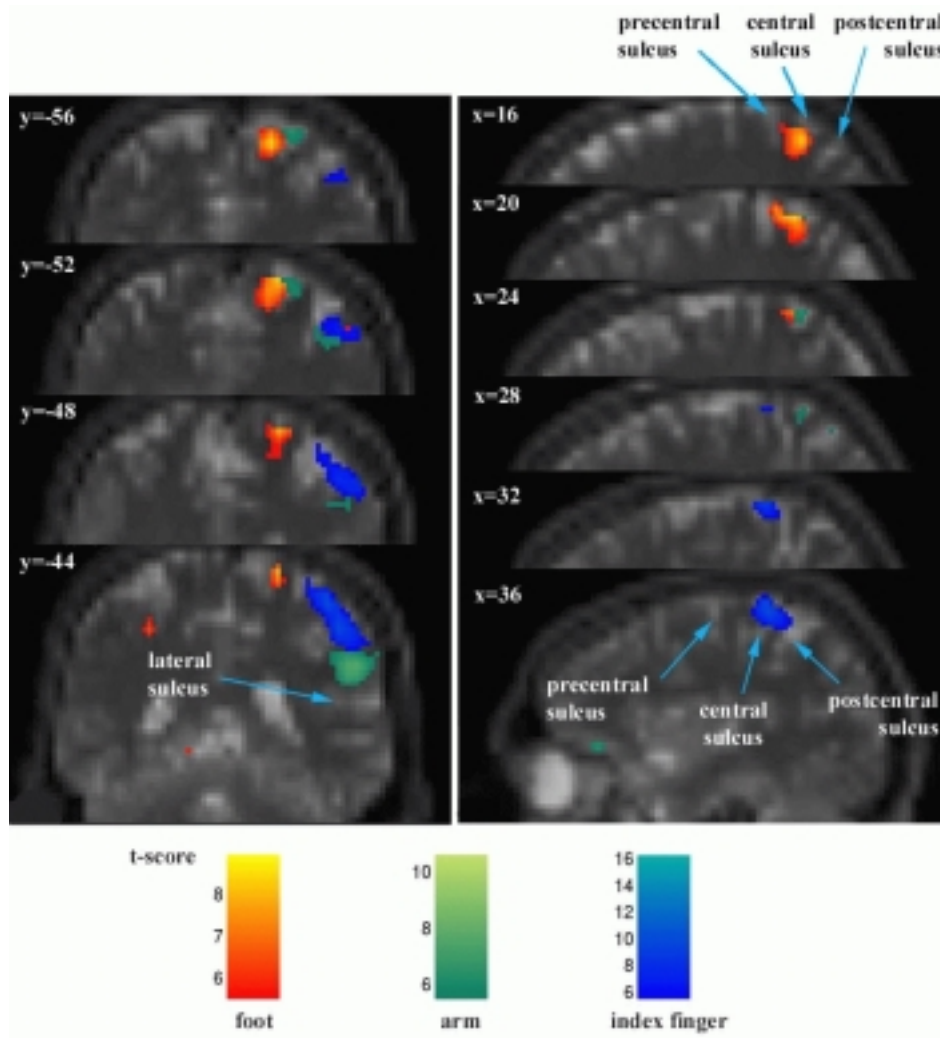


Figure 5.6: Left: Coronal slices of the structural scan of subject F with superimposed $\text{SPM}\{t\}$ s from the 3 sessions thresholded at $t = 5.5$ ($p_{\text{corr}} = 0.001$ at $df = 198$). The top slice ($y = -56$) is the most anterior one. Right: Sagittal slice of the same mapped brain volume. The top slice ($x = 16$) is the most medial one. All slices are spaced with $1 \text{ voxel} = 4 \text{ mm}$.

Only superposition of thresholded $SPM\{t\}$ s onto a coregistered structural scan of the subject can accurately localize the activity clusters of non-normalized data. This has to be done by identifying certain structures through comparison to a brain atlas. Figure 5.6 depicts series of coronal and sagittal slices of the coregistered structural scan of subject F with superimposed $SPM\{t\}$ s from foot, arm and index finger. The lateral, central, postcentral and precentral sulci were localized by visual inspection [No195]. In MRI images sulci are generally white and gyri black.

The top coronal slice ($y = -56$) resembles the somatosensory homunculus with the foot located medially to the arm and followed by the index finger. Continuing to more anterior slices the arm and foot clusters disappear. This makes sense since the angle between the plane formed by the central sulcus and the z-axis and the interhemispheric plane is less than 90° , i.e. the foot is situated posterior to the index finger. The central sulcus can be identified on the sagittal slices. The three activity clusters are located in the direct proximity of the central sulcus. The index finger lateral and anterior, the foot medial and posterior and the arm in between.

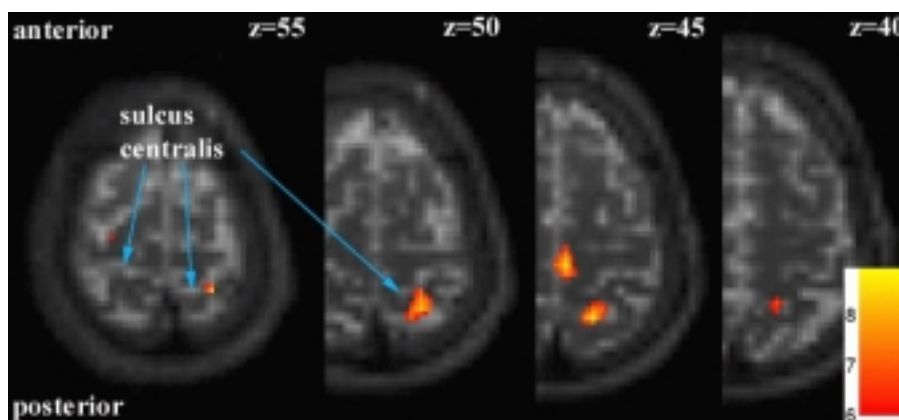


Figure 5.7: Axial slices showing the foot activity clusters in SI and MI (SI is anterior to MI) for subject F.

In the lower coronal slices the second arm cluster appears. A mere look at the SPM99 glass brains would have identified it as an activation of SII. Figure 5.6 shows that it is located where one would expect the facial representation in SI, which is anterior to SII, above the lateral sulcus. No funded explanation for the occurrence of this cluster can be offered here. One guess might be, that the subject has moved his lips during the active phases of the experiment. Any movement automatically involves tactile stimulation. The lips have a very large representation in both somatosensory and motor homunculi, so even slight movements can evoke brain activation. It is also possible that the stimulus is caused by twitching of the facial muscles.

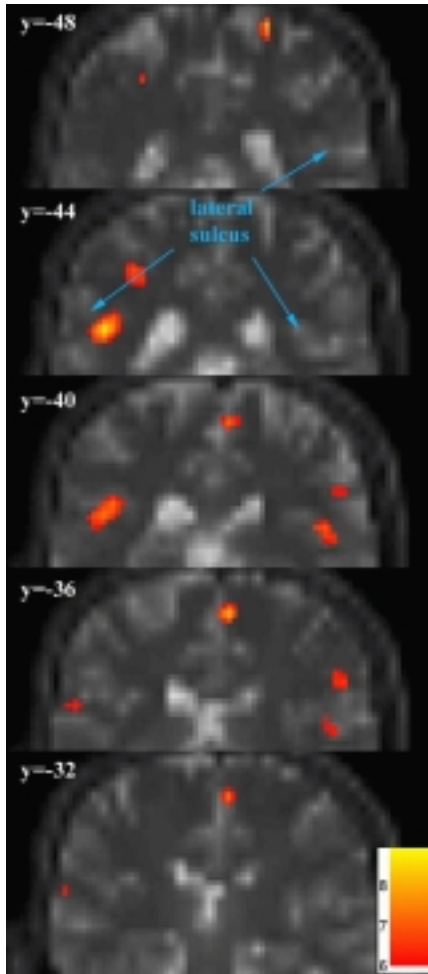


Figure 5.8: Coronal slices showing the foot activity clusters in SI and SII for subject F.

As mentioned above there are two foot activity clusters in the superior part of the brain. The second one has not yet been localized precisely. Figure 5.7 depicts a series of axial slices of the coregistered structural scan with only the $SPM\{t\}$ from session 2 thresholded at $t=6$ superimposed. The second cluster appears anterior to the SI foot activity cluster and the central sulcus that has again been spotted by visual inspection. This cluster is situated in the primary motor cortex (MI) on the border to the supplementary motor area (MII). Hence there had to be motor stimulation. Since the motor and the somatosensory activity clusters are well separated the unwanted motor cluster does not perturb the analysis.

So far the focus has been on the primary somatosensory cortex neglecting the secondary somatosensory cortex. The conducted analysis yields only one activity cluster of interest for session 1, so there is no activation of SII at the given significance. Session 2 on the contrary yields a bilateral representation of SII. SII is located in the depth of the lateral sulcus. Figure 5.8 depicts a series of coronal slices with again only the $SPM\{t\}$ from session 2 superimposed. The bilateral activation of SII can best be seen on the middle slice. The ipsilateral¹ activation area is a little posterior to the contralateral one². Both activations are highly significant and it can be concluded that stimulation of the foot with the PTD is apt to cause activation of the secondary somatosensory cortex additionally to that of SI.

Summary

Tactile stimulation of the right index finger, arm and foot with the PTD has resulted in brain activations in SI resembling the expected somatotopic map both in position and size. The activations take place along the central sulcus with the foot activation on the medial side followed by the arm and the index finger activations towards the lateral side. The index activation is the largest one (101 voxels) followed by the SI foot cluster of 21 voxels and the arm with only 7 voxels. There is an unexplained brain activation of that area in SI that should be primarily responsible for processing facial tactile stimulation that occurred during the stimulation of the arm. Stimulation of the foot with the PTD also

¹‘on the same side’

²Ipsi- and contralateral refer to the stimulation not the other activations

involves bilateral activation of SII and effects stimulation of the motor cortex for subject F. The activity clusters of somatosensory and motor stimulation are well separated, so the motor activation does not confound the analysis. It can be concluded that the reported tactile experiments with the PTD succeeded in mapping the somatosensory homunculus at three distinct points. The stimulation of the index finger appears to be the most stable and well-defined one. SII was involved only in processing the foot stimulation. Motor stimulation could not be avoided completely in spite of careful mounting of the modules.

5.3 Tactile versus Motor Stimulation

5.3.1 Experimental Procedure

Motor tasks intrinsically involve tactile stimulation due to the deep receptors (Brodmann areas 3a and 2) but usually the cutaneous receptors are also stimulated. When bending and stretching a finger, for example, the skin of different parts of the finger touch. On the contrary tactile stimulation does not necessarily cause motor stimulation, although this can happen as was seen in the previous section for subject F, session 2. The separation of motor and tactile brain activation resulting from the corresponding stimulation of the right index finger is investigated in this section. For this purpose another fMRI experiment with subject F (session 4) concerned with motor stimulation of the right index finger was performed. The experimental procedure is basically the same as for the three tactile sessions from the last section. During the active phase the subject alternately bends and stretches his right index finger. During the compare phase he silently lists the days of the week backwards, but does not tap his left finger as he did for the compare phases of the three tactile sessions. The PTD is used to ‘trigger’ the phases, i. e. to let the subject know when to start bending and stretching his finger and when to stop. It is mounted on the left hand in the same way it was for tactile stimulation of the index finger (see fig 5.2).

5.3.2 SPM Analysis and Overlap

The SPM analysis is performed exactly the same way as for sessions 1, 2 and 3 involving tactile stimulation. The threshold of $p_{\text{corr}} = 0.001$ and $k = 5$ vox yields 2 relevant activity clusters. The first one comprises 69 voxels with its maximum $t = 11.9$ at (40, -40, 45), the second on 11 voxels with a maximum $t = 8.02$ at (56, -36, 30). A third cluster in the cerebellum is observed but is of no further interest. The cerebellum is expected to be involved in motor task processing (see section 1.6). Figure 5.9 depicts a series of sagittal slices of the structural scan with the motor and the tactile SPM $\{t\}$ s superimposed next to a series that shows only the tactile activities. The two motor clusters are very close together, the second one seems to be an extension of the first one. The motor clusters are located anterior to the tactile one as expected. They overlap by 38 voxels, i. e. 47.5 % of the motor cluster are also active during a mere tactile stimulation and 37.6 % of the voxels active during tactile stimulation also exhibit activation during motor stimulation.

The overlap was calculated by means of a self-written MATLAB script (`overlap.m`). It uses the structure `SPM` that SPM99 calculates during thresholding in its ‘results’ section. `SPM` is a structure that contains information on the `SPM{t}`, the corresponding t-distribution and on thresholding details. It includes a matrix with the coordinates of the voxels that survived thresholding as well as an array with the corresponding t-scores. The coordinate matrices of the two `SPM{t}`s are compared and the overlap determined. It is not possible to totally separate the motor and the tactile brain activations in subject F. The motor activation extends to the postcentral gyrus as expected (see fig. 5.9). The tactile activation in SI also ‘leaks’ into the precentral gyrus. It is nevertheless possible to distinguish between an activation due to tactile stimulation of the index finger with the PTD and a motor activation from the same index finger in subject F as the overlap of the two is less than 50 %.

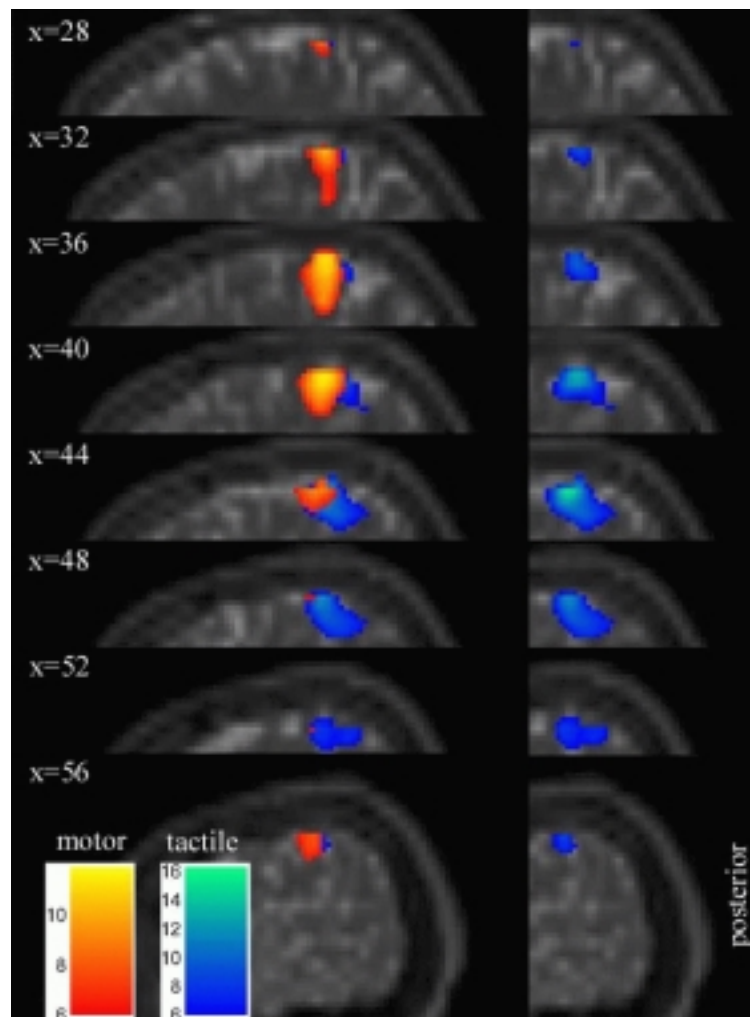


Figure 5.9: A series of sagittal slices with the motor and the tactile activations in MI and SI next to a series of the same slices with only the tactile activations in SI for subject F.

5.4 Reproducibility of Motor Stimulation

During the compare phases of the three tactile experiments the subject tapped his contralateral finger and silently listed the days of the week backwards. This is primarily a motor stimulation, so activation clusters in MI and in the cerebellum are to be expected. The compare phase was identical in all three experiments so it can be used to estimate the reproducibility of the results for motor tasks.

Regions that exhibit activity during the compare phase can be extracted by applying a contrast of $\vec{c} = [-1 \ 0]$. Since motor tasks are generally very robust a higher threshold of $p_{\text{corr}} = 10^{-5}$ and $k = 30$ voxels is effected. For all 3 sessions this threshold yielded clusters in both MI and the cerebellum. The clusters with their maximum t-scores are listed in table 5.1. All maximum t-scores are located in MI.

Session & Phase	Coordinates [mm]	t-score	cluster size [vx]
1 (index, compare)	(-40, -36, 40)	20.0	125
2 (arm, compare)	(-40, -36, 45)	25.7	180
3 (foot, compare)	(-36, -32, 40)	20.7	120
4 (motor, active)	(40, -40, 45)	11.9	69

Table 5.1: The maxima of the activities in MI for the compare phases of the 3 tactile sessions and the active phase of session 4.

All maxima of the clusters from the compare phases are located within a neighbourhood of 4 voxels.. Even the cluster from the active phase from session 4 peaks at almost the same point in the opposite cerebral hemisphere. The cluster from session 1 and 3 are almost of the same size and the maximum t-scores are very similar. Session 2 yields a larger cluster (about 1.5 times the size of the other two) and a higher maximum t-score. Hence the overlap of the other clusters with this one is relatively small. Table 5.2 contains the overlap in percent of the clusters.

cluster from session	overlaps with cluster from session [%]		
	1	2	3
1 (index)		88.0	87.2
2 (arm)	61.1		61.7
3 (foot)	90.8	92.5	

Table 5.2: The overlap of the clusters from the compare phases of the 3 tactile sessions.

The clusters from sessions 1 and 3 are almost identically reproduced. In addition to almost identical maximum t-scores in both location and value, their cluster size differs by only 5 voxels and they overlap by 109 voxels (87.2 % and 90.8 %). Cluster 2 is larger and more significant than clusters 1 and 3. About 90 % of clusters 1 and 3 are contained in cluster 2.

In summary it can be said that the motor activations are well reproducible. In particular the coordinates of the most significant voxel can be reproduced with a deviation of only one voxel. Cluster size and maximum t-value are subject to larger deviations (max. $\Delta t = 5.7$ and max. $\Delta k = 60$ vx).

5.5 Reproducibility of Tactile Stimulation

5.5.1 Experimental Procedure

Experiments with two other subjects (M and N) were performed with the main goal to investigate the reproducibility of activations due to tactile stimulations. Subjects M and N are a 21 years old healthy female and a 22 years old healthy male. Index finger and foot were chosen as stimulation sites as they turned out to be suitable locations for well-defined, significant brain activation for subject F. Their brain activations are also expected to be farthest apart in the somatosensory homunculus as confirmed by analysis of sessions 1 and 3 with subject F.

In the experiment with subject F the active and the compare phases lasted for 10 scans each. The resulting brain activation was highly significant. For this experiment the length of active and compare phases were reduced to 7 and 3 scans respectively to save time. While index finger and foot were stimulated in separate sessions for the first experiment they are now alternately stimulated in a single session. This means there are two active phases in each session separated by a short compare phase. One module is mounted on the right index finger of the subject, a second one on the medial side of its left foot's instep as described in section 5.1.2. A walking pattern is applied to the first module for 7 scans (active phase index). Then a compare phase lasting for 3 scans follows during which the subject silently lists the days of the week backwards. Afterwards the same walking pattern is applied to the second module for 7 scans (active phase foot) followed again by a compare phase of 3 scans. This is repeated 10 times (200 scans in total). To maintain the subject's attention the direction of the walking pattern is pseudo-randomly varied from one period to the next. The subject tries to count the occurrences of the walking pattern in the initial direction.

There were 6 sessions for each subject. For the first 3 sessions (M[N]1.1, M[N]1.2 M[N]1.3) the modules were mounted on the right index finger and the left foot, for the last 3 sessions (M[N]2.1, M[N]2.2 M[N]2.3) on the left index finger and the right foot. Thus a comparison to the activation of the opposite cerebral hemisphere can be made. There were always 3 sessions performed in one run. This means the subject was inside the MRI tube for about one hour at a time. There was a 1.5 hour break for each subject between the two runs. Unfortunately a program error occurred during the second run for subject N and the PTD did not work properly. Therefore run N2.x is not included in the analysis.

In addition to the reproducibility the frequency dependence of the stimulations performed by the PTD is investigated. The frequency of the walking pattern is varied within the sessions. There are 3 different frequencies. For frequency A (B/C) the 4 taxels are suc-

cessively activated for 50 ms (200 ms/350 ms) each with no break, which corresponds to a frequency of 5 Hz (1.25 Hz/0.7 Hz). M[N]1.1 is performed with frequency B, M[N]1.2 and M[N]1.3) with frequencies C and A respectively (frequency encoding BCA). In the second run the frequency encoding was ABC.

The modules are operated at an air pressure of 5.9 bar. For each session 200 images were taken with a TR of 5 s. 32 slices of 4 mm thickness with no gap make up one brain volume. One slice consists of 64×64 voxels. With a FOV of 25.6 cm this yields a voxel size of $1 \text{ vx} = 4 \text{ mm} \times 4 \text{ mm} \times 4 \text{ mm}$. The resolution of the structural T_2 scan is $128 \times 128 \times 80 \text{ vx}$ with $1 \text{ vx} = 2 \text{ mm} \times 2 \text{ mm} \times 2 \text{ mm}$.

5.5.2 SPM Analysis

Preprocessing, Model and Threshold

Preprocessing was performed similar to that of the first experiment with subject F. The data was realigned for each run (1 run = 3 sessions) to the first image of the first session. The structural T_2 scan was coregistered to the same image. Smoothing was performed with a Gaussian kernel of $\text{FWHM} = 8 \text{ mm} \times 8 \text{ mm} \times 8 \text{ mm}$. Coordinates are again reported in the same kind of individual coordinate systems as for the first experiment.

The design matrix comprises two effects of interest and one effect of no interest. The first column is also a box-car function lagged by one image with a period of 20 images. The ‘on’ phase of the box-car function lasts for 7 images, the ‘off’ phase for 13 images. The second column is a box-car function lagged by 11 images. The first column models the stimulation of the index finger, the second one that of the foot. The third column contains the offset that is an effect of no interest. The box-car functions are again convoluted with the haemodynamic response function. A high-pass filter with a cut-off period of 200 s is applied.

A contrast of $\vec{c} = [1 \ -1 \ 0]$ yields a contrast image (`con_0001.img`) of the approximated height of the first minus the approximated height of the second box-car. The corresponding $\text{SPM}\{t\}$ reflects the significance of each voxel for being active during the stimulation of the index finger and inactive during stimulation of the foot. An $\text{SPM}\{t\}$ relating to the significance of voxels being active during stimulation of the foot and inactive during stimulation of the index finger can be obtained with a contrast of $\vec{c} = [-1 \ 1 \ 0]$. The same threshold as for the first experiment is applied ($p_{\text{corr}} = 0.001$ and $k = 5 \text{ vx}$) to the $\text{SPM}\{t\}$ s.

Detected Brain Activity

This threshold yields index finger activation clusters in the contralateral primary somatosensory cortex for all sessions. These clusters are large (up to 250 vx) and have highly significant maxima ($10.4 \leq t \leq 26$). The larger ones ‘leak’ into the primary motor cortex. The high significances and the large cluster sizes are probably due to the high pressure of 5.9 bar (compared to 4 bar in the experiment with subject F). Index finger activation cluster in the secondary somatosensory cortex are visible in eight out of nine sessions. They are smaller than the clusters in SI (5 to 72 vx) and less significant ($6.1 \leq t \leq 12.6$).

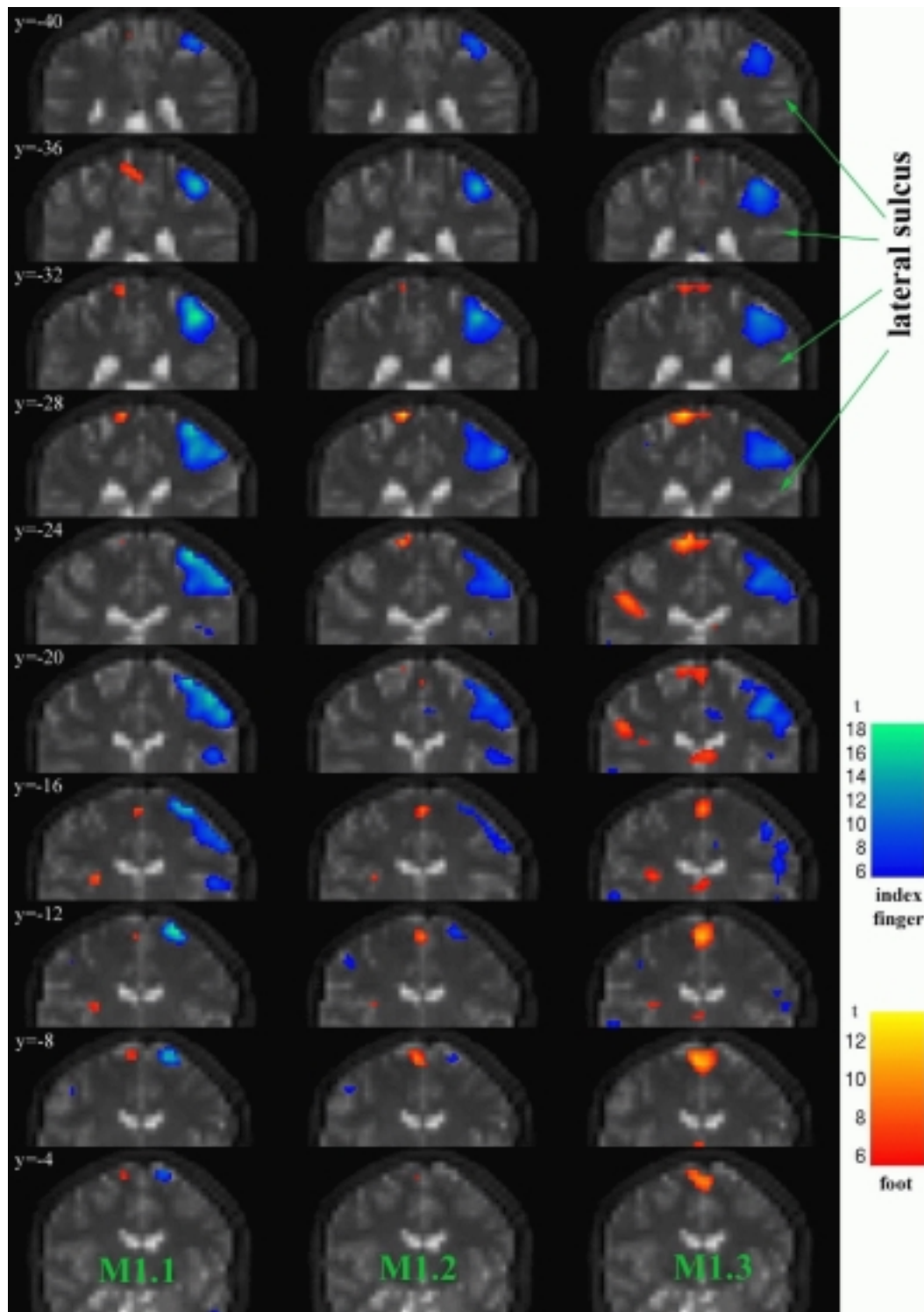


Figure 5.10: The index and foot brain activations in coronal slices for the first run with subject M.

In session M2.2 the activations in the primary and the secondary somatosensory cortex are not separable at the given threshold. While these activation clusters in the contralateral SI and SII were to be expected there are some other ones on the ipsilateral SI and MI that are rather surprising. In four out of nine sessions an activation of the ipsilateral primary somatosensory cortex occurred. In two out of these four the ipsilateral primary motor cortex was also involved. In another session only the ipsilateral MI exhibited a rather small activation.

In eight out of nine sessions foot activation clusters appear in SI at the given threshold. Cluster size ranges from 11 to 39 vx with maximum significance of $8.3 \leq t \leq 13.7$ except for session M1.3. In session M1.3 the foot activation clusters in SI and MI are indistinguishable and form one large cluster of 90 vx. The foot activation clusters in SII are of comparable size and significance (7 to 36 vx and $7.1 \leq t \leq 11.9$). Subject M did not exhibit activation of SII for the foot during session M1.2 nor during the entire second run (M2.x). While the foot stimulation did not evoke any motor response from subject N, there are activation clusters in MI in all sessions for subject M.

Mapping of Brain Activity

Figures 5.10, 5.11 and 5.12 depict the superpositions of the SPM $\{t\}$ s thresholded at ($p_{\text{corr}} = 0.001$) for both contrasts onto the structural scans in series of coronal slices for the three analyzed runs. The figures illustrate the large size of the index finger activations in the proximity of SI. Only in N1.3 and M2.3 they are reduced to 41 and 81 voxels respectively.

In figure 5.10 the index finger activations of SII are clearly visible in the lateral sulcus. Since there was no spatial threshold applied for the superposition of the activations on the structural slices a small index finger activation of SII is visible in M1.3 on slice $y = -20$. The foot activations in SII can also be discerned in slices $y = -20$ to $y = -12$. The index activations in SI are very large and extend deep into the brain. For M1.1 and M1.2 the foot activations in SI and MI are well separated. The ones in SI span the slices $y = -36$ to $y = -24$. There is an ipsilateral activation in MI for session M1.2 (slices $y = -12$ and -8). The overlap of the clusters in M1.x is 128 vx in index and 6 vx in foot activation of SI. There is no overlap in the index activations of SII while the clusters from the foot activations in SII overlap by 5 vx. For the calculation of the overlap the combined height and spatial threshold is used.

For subject N the index activations in SI are closer to the brain surface. During the first session an activation on the ipsilateral SI for both index and foot become visible. The index finger activation of SII is present in all sessions. Subject N exhibits a stronger foot activation in SII than in SI. For session N1.2 the one in SI is even eliminated by the spatial threshold of $k = 5$ vx and only appears on the coronal slices in figure 5.11. The index clusters overlap by 41 and 10 voxels in SI and SII, the foot clusters by 0 and 19 voxels respectively.

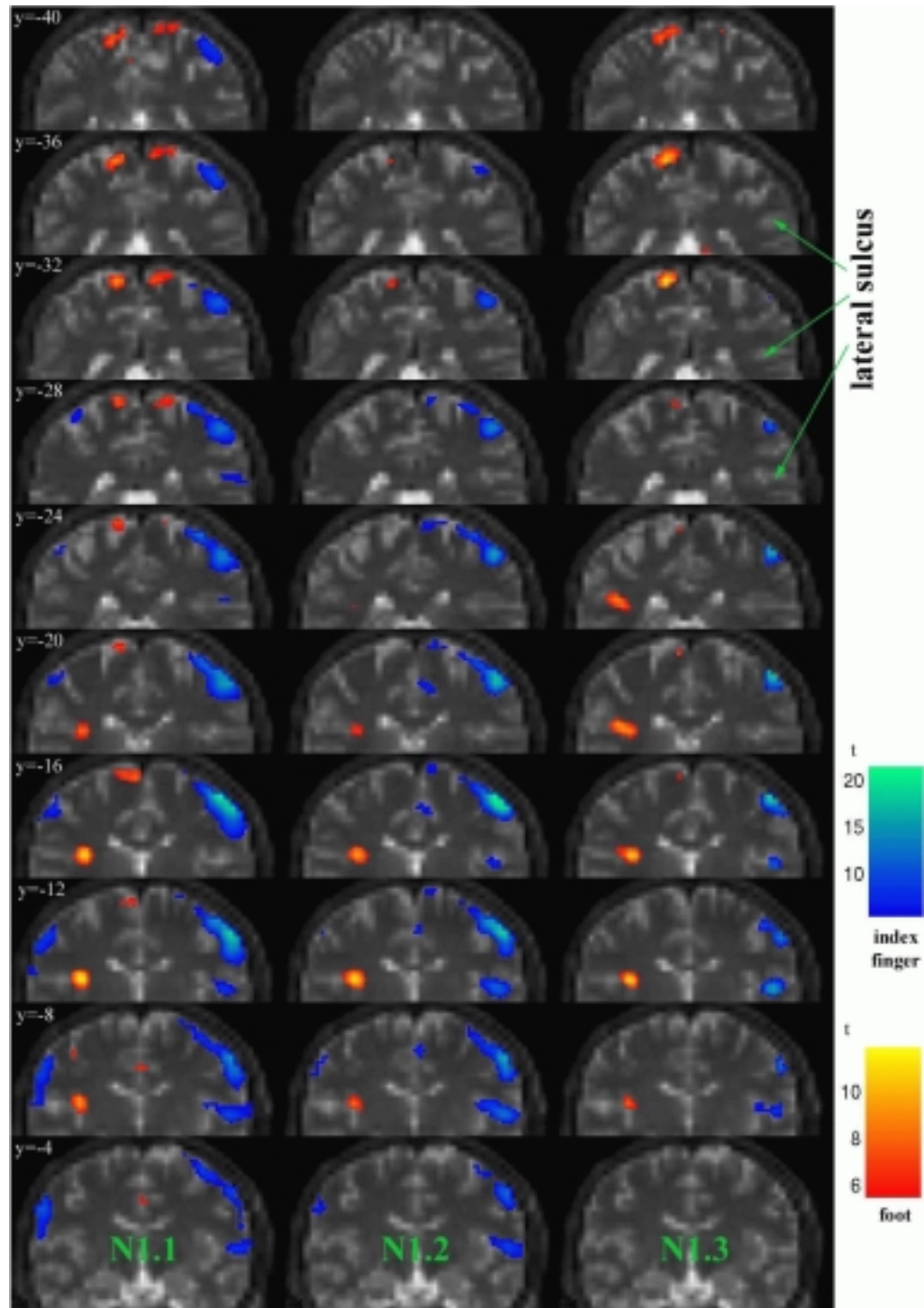


Figure 5.11: The index and foot brain activations in coronal slices for the first run with subject N.

For the second run with subject M both index and foot activation of SI takes place in the opposite cerebral hemispheres than for the first run. There is no foot activation of SII but the index finger cluster is present in figure 5.12. The foot activations in SI and MI are well separated for all three sessions. In sessions M2.1 and M2.2 there is again an activation of the ipsilateral SI. The overlap comprises 64 and 5 voxels in SI and SII for the index activation and 22 and 4 voxels correspondingly for the foot activation.

Summary

There are index finger activations in the contralateral SI and SII for all analyzed sessions for both subjects. One of these activations in SII (M1.3) is smaller than 5 vx. Foot activation clusters in SI also appear in all sessions, but one (N1.2) is again smaller than 5 vx. There are foot activations in SII in all sessions of the first runs for both subjects. During the second run for subject M only one small (< 5 vx) foot activation shows in SII during session M2.2.

For subject N the foot activations in SII are more significant than those in SI. Activations in SII are often linked to the degree of concentration according to C. Stippich³. This would indicate that subject N focussed intensely on his task. Reduction of concentration with preceding sessions could also explain the lack of foot SII activation in the second run for subject M.

For both subjects activation of the ipsilateral SI and MI occurred in some sessions, but not in all. All stimulations evoke activity in the motor cortex although the modules were mounted carefully. This might be avoided by operating the PTD at a lower air pressure. The stimulation of the index finger involves activation of MI that is not separated from the activation in SI for both subjects. The two are ‘melted together’. On the contrary the stimulation of the foot caused activation of MI only in subject M and it is disjoint from the activation of SI with the exception of session M1.3.

The foot activity cluster is located medial to the index finger activation in SI for all sessions corresponding to the expected somatotopic map of SI. Since the index finger cluster in SI is large and not separable from the index finger MI activation, it is difficult to judge whether it is posterior or anterior to the foot activation. Nevertheless it extends anterior to the foot cluster in all cases. The foot cluster in SII is found medial to the index finger activation along the lateral sulcus for all relevant sessions. It can be summarized that not only the somatotopy of SI but also that of SII has been successfully mapped for the index finger and the foot in subjects M and N.

The next step is to evaluate the reproducibility of tactile activations for each subject. This is done by comparing the respective maximum t-scores, their coordinates and corresponding cluster sizes, which are listed in tables 5.3 to 5.8. In section 5.4 the reproducibility of motor activation was examined and it turned out that the coordinates of the maximum t-scores were well reproduced while the t-values themselves and the cluster sizes varied on a larger scale.

³Department of Neuroradiology, University of Heidelberg, Medical School

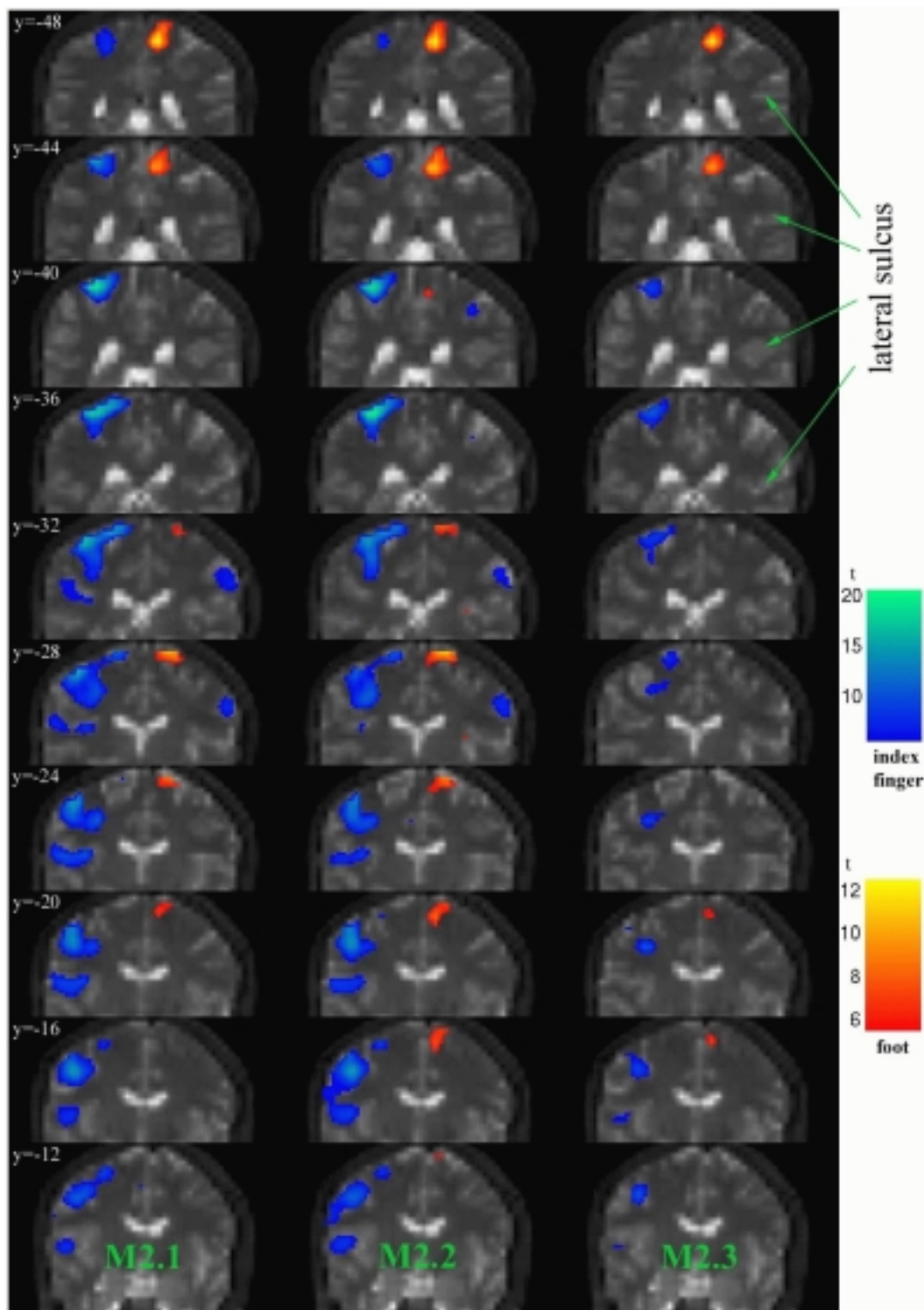


Figure 5.12: The index and foot brain activations in coronal slices for the 2^d run with subject M.

Reproducibility of Brain Activity

The coordinates of the maximum t-scores of the clusters are well reproduced for most major clusters. For subject N the coordinates of the maximum t-scores of the foot clusters in SI and SII are reproduced exactly. Those of the index clusters in SI and SII are at least direct neighbours. Only the most significant locations of ipsilateral activations of SI/MI (detected only in N1.1 and N1.2) are 1.2 cm apart.

In the first run with subject M the coordinates of the maximum t-scores of the index SI, the index SII and the foot MI clusters are reproduced adjacent to each other. The maxima of the foot SI cluster are found at identical locations. In SII the second maximum of the foot cluster of M1.3 is one voxel apart from the first maximum of M1.1 (there is no cluster for M1.2).

For the index SI cluster the maximum from M2.3 deviates by approximately 3 cm from the other two maxima, which are adjacent to each other. In index SII the maxima from M2.1 and M2.3 are 1.6 cm apart. A maximum for M2.2 cannot be determined as SI and SII are indistinguishable. The maxima in the ipsilateral SI for index finger stimulation, which was only detected in M2.1 and M2.1, are located next to each other. Exact reproduction of the foot activations in SI is recorded while there was no activity in SII during run M2. The foot MI maxima of M2.1 and M2.2 are found at the same locations and that of M2.3 neighbours the second maxima of M2.1 and M2.1.

So far only the coordinates of the maximum t-values within each run were compared. For subject M two runs were analyzed. The coordinates of both runs can be compared if one run is mirrored on the interhemispheric plane ($x \rightarrow -x$). One should keep in mind though, that the human brain is not necessarily exactly symmetric. The adjacent maxima of the index SI clusters from sessions M2.1 and M2.2 can be found superior (by 3 vx) and posterior (by 0-2 vx) to the maxima from run M1. On the contrary, the corresponding maximum from M2.3 is located inferior (by 2 vx) and anterior (by 3-4 vx) to the most significant voxels from M1.x. The activations detected in SII for index finger stimulation deviate by approximately 2 vx in all directions when comparing the two runs for subject M. The maxima of the foot SI activations were duplicated at the exact same locations within both runs. Those from M2 are located inferior by 3 vx, posterior by 5 vx and medial by 1 vx to the maxima from M1. In the proximity of the foot in SII no comparison can be made as no activation was detected for the second run with subject M. Comparing the maxima of the foot activations in MI is less straight forward (see table 5.8). The maxima of run 2 tend to be situated more superior (by 1-2 vx), more lateral (by 0-4 vx) and more posterior (by 0-4 vx).

Index finger activations in contralateral SI			
Session	Coordinates [mm]	t-score	cluster size [vx]
M1.1	(36, -32, 36)	18.0	241
M1.2	(36, -32, 36)	16.0	199
M1.3	(36, -36, 36)	13.3	213
N1.1	(48, -16, 40)	26.0	250
N1.2	(48, -16, 36)	21.5	163
N1.3	(48, -16, 40)	11.1	41
M2.1	(-32, -40, 48)	18.2	290
M2.2	(-32, -36, 48)	20.5	284
M2.3	(-36, -20, 28)	10.4	81
2 nd max	(-32, -36, 48)	10.3	

Table 5.3: Maxima of index finger activity clusters in contralateral SI.

Index finger activations in contralateral SII			
Session	Coordinates [mm]	t-score	cluster size [vx]
M1.1	(48, -20, 0)	9.6	18
M1.2	(48, -20, -4)	7.0	8
N1.1	(56, -8, -8)	11.6	26
N1.2	(56, -8, -8)	12.6	49
N1.3	(52, -12, -8)	9.2	16
M2.1	(-40, -24, 4)	9.8	72
3 rd max	(-52, -12, -4)	7.8	
M2.2	SI and SII 'melted together'		
M2.3	(-52, -16, -4)	6.1	5

Table 5.4: Maxima of index finger activity clusters in contralateral SII.

Index finger activations in ipsilateral SI and MI				
Session	Coordinates [mm]	t-score	cluster size [vx]	comment
M1.2	(-48, -8, 32)	6.3	5	ipsilateral MI
N1.1	(-72, -4, 20)	13.0	77	ipsilateral SI/MI
N1.2	(-64, 4, 24)	7.6	19	ipsilateral SI/MI
M2.1	(52, -28, 20)	7.2	16	ipsilateral SI
M2.2	(52, -28, 24)	7.6	14	ipsilateral SI

Table 5.5: Maxima of index finger activity clusters in ipsilateral SI and MI.

Foot activations in contralateral SI			
Session	Coordinates [mm]	t-score	cluster size [vx]
M1.1	(-12, -28, 56)	8.3	15
M1.2	(-12, -28, 56)	11.2	11
M1.3	(-12, -28, 56)	13.5	90
N1.1	(-20, -32, 52)	8.5	39
N1.3	(-20, -32, 52)	11.0	30
M2.1	(8, -48, 44)	11.5	26
M2.2	(8, -48, 44)	12.5	31
M2.3	(8, -48, 44)	13.7	22

Table 5.6: Maxima of foot activity clusters in contralateral SI.

Foot activations in contralateral SII			
Session	Coordinates [mm]	t-score	cluster size [vx]
M1.1	(-28, -16, 4)	7.1	7
M1.3	(-48, -24, 16)	9.3	22
2 nd max	(-32, -16, 4)	7.7	
N1.1	(-44, -12, 0)	10.3	27
N1.2	(-44, -12, 0)	11.9	22
N1.3	(-44, -12, 0)	10.9	36

Table 5.7: Maxima of foot activity clusters in contralateral SII.

Foot activations in contralateral MI			
Session	Coordinates [mm]	t-score	cluster size [vx]
M1.1	(0, -16, 48)	6.9	8
M1.2	(0, -12, 48)	8.5	18
M1.3	SI and MI ‘melted together’		
M2.1	(16, -28, 56)	9.6	20
2 nd max	(8, -20, 52)	6.7	
M2.2	(16, -28, 56)	10.9	38
2 nd max	(8, -20, 48)	8.4	
M2.3	(8, -16, 48)	7.3	5

Table 5.8: Maxima of foot activity clusters in contralateral MI.

Summary

16 clusters are detected in the regions of interest in 3 runs with 2 subjects, 3 of these clusters are found in the ipsilateral cerebral hemisphere. The coordinates of the maximum t-scores of 4 clusters were reproduced exactly for the 3 sessions of each run. 5 maxima were reproduced as face to face neighbours, i. e. with a deviation of only 1 vx or 4 mm and one maximum as edge to edge neighbours ($\Delta = 5.6$ mm). Taking the second and the third maxima of the clusters into account 2 more locations are reproduced as face to face neighbours, another one as edge to edge neighbours and one with a deviation of 2 vx in the x-direction. For one region of interest a cluster was present in only one session so no comparison can be made. The last one of the 16 clusters shows the largest maximum to maximum deviation of 12 mm. The deviation when comparing left and right cerebral hemisphere in subject M is up to 24 mm. As the human brain is not necessarily symmetric this is not unexpected. Neither the values of the t-scores nor the cluster sizes are reproducible. There is no adaptation effect or any correlation to the frequency discernable in either t-values, cluster sizes or location maximum t-values.

As the t-score depends on the quality of the estimation and on the residual variance, deviations in the t-value are to be expected. This uncertainty also justifies taking the second and third maxima of the activation clusters into account for evaluating the reproducibility of activation sites. The cluster size is linked strongly to the t-scores. With the coordinates of the most significant voxels, the most important spot for processing tactile information in the human brain can be accurately reproduced for each subject. In chapter 5.8 the significance of the voxels will be further investigated, but first an intersubject analysis with normalized data is performed.

5.6 Intersubject Analysis

Preprocessing, Model and Threshold

In the previous sections each subject was analyzed individually using the superpositions of the $SPM\{t\}$ s onto the coregistered structural scans. In this section the results from all subjects are compared to each other. For this purpose a reference coordinate system needs to be defined. SPM99 used the MNI coordinate system (see appendix C). The data from each subject is normalized to the standard MNI brain (see section 4.1.4) after realignment. The normalization parameters used are listed in the batch-file `prepro2.m` in appendix D. The images are resampled to $1\text{ vx} = 2\text{ mm} \times 2\text{ mm} \times 2\text{ mm}$. After normalization the images were smoothed with a Gaussian kernel of $FWHM = 4\text{ mm} \times 4\text{ mm} \times 4\text{ mm}$. The design matrices for all experiments as well as the applied contrasts are identical to those used for the individual analyses. The same corrected height threshold of $p = 0.001$ but with a larger spatial extent threshold of $k = 20\text{ vx}$ is applied to the $SPM\{t\}$ s for the active phases of all experiments.

Detected Brain Activity

The normalized data exhibits contralateral SI activity clusters for both index finger and foot in all sessions for all subjects. SII activation was also detected in all cases with only two exceptions: In session M1.3 no index finger activity and in session M2.3 no foot activity occurred. Subjects M and F also showed an activation of contralateral MI for the foot stimulation. Index finger activation of MI took place only for M2.3 and F. Finally there was also ipsilateral SI activation for the index finger in some sessions (M1.2, N1.1, N1.2, M2.1, M2.1 and F). Tables 5.9 to 5.15 list the maximum t-scores with the corresponding coordinates and voxel sizes classified by the stimulated brain region.

Index finger activations in contralateral SI			
Session	Coordinates [mm]	t-score	cluster size [vx]
M1.1	(44, -36, 58)	21.9	1106
M1.2	(44, -36, 58)	22.0	973
M1.3	(42, -20, 48)	15.2	803
2 nd max	(46, -36, 60)	13.0	
N1.1	(50, -18, 58)	27.3	1089
N1.2	(52, -18, 56)	21.9	680
N1.3	(54, -18, 56)	11.3	193
M2.1	(-36, -46, 68)	17.9	1104
M2.2	(-34, -44, 70)	21.2	1288
M2.3	(-30, -40, 72)	10.1	93
F	(50, -22, 62)	21.9	464

Table 5.9: Maxima of index activity clusters in contralateral SI for normalized data.

Index finger activations in contralateral SII			
Session	Coordinates [mm]	t-score	cluster size [vx]
M1.1	(56, -16, 14)	13.7	98
M1.2	(58, -16, 10)	9.7	84
N1.1	(58, -10, 2)	16.5	179
N1.2	(58, -10, 2)	15.0	251
N1.3	(54, -14, 4)	11.3	84
M2.1	(-44, -22, 16)	12.6	353
M2.2	(-44, -24, 16)	12.2	395
3 rd max	(-54, -16, 8)	10.4	
M2.3	(-50, -16, 8)	7.7	51
F	(44, -14, 12)	10.5	86

Table 5.10: Maxima of index activity clusters contralateral SII for normalized data.

Index finger activations in ipsilateral SI			
Session	Coordinates [mm]	t-score	cluster size [vx]
M1.2	(-50, -20, 48)	8.9	54
N1.1	(-62, -18, 36)	12.6	351
3 rd max	(-58, -8, 38)	10.8	
N1.2	(-58, -8, 38)	10.3	66
2 nd max	(-62, -18, 36)	7.6	
M2.1	(64, -18, 38)	6.9	21
M2.2	(64, -18, 38)	8.3	81
F	(-48, -44, 14)	8.0	25

Table 5.11: Maxima of index activity clusters in ipsilateral SI for normalized data.

Index finger activations in contralateral MI			
Session	Coordinates [mm]	t-score	cluster size [vx]
M2.3	(-36, -22, 46)	13.9	251
F	(44, -24, 66)	11.7	432
2 nd max	(40, -24, 48)	11.7	

Table 5.12: Maxima of index finger activity clusters in contralateral MI for normalized data.

Foot activations in contralateral SI			
Session	Coordinates [mm]	t-score	cluster size [vx]
M1.1	(-12, -36, 80)	11.8	124
M1.2	(-12, -34, 80)	13.9	51
M1.3	(-12, -34, 80)	15.2	92
N1.1	(-12, -42, 70)	10.7	118
N1.2	(-12, -38, 72)	7.8	20
N1.3	(-12, -38, 72)	11.5	83
M2.1	(12, -48, 64)	15.3	139
M2.2	(12, -48, 64)	17.2	164
M2.3	(12, -48, 64)	18.5	111
F	(16, -48, 74)	9.6	55

Table 5.13: Maxima of foot activity clusters in contralateral SI for normalized data.

Foot activations in contralateral SII			
Session	Coordinates [mm]	t-score	cluster size [vx]
M1.1	(-32, -22, 12)	10.3	63
M1.2	(-32, -22, 14)	12.3	97
M1.3	(-56, -34, 32)	11.9	291
3 rd max	(-34, -22, 16)	10.1	
N1.1	(-38, -22, 16)	13.1	131
N1.2	(-38, -22, 16)	12.8	100
N1.3	(-36, -24, 14)	11.7	150
M2.1	(36, -20, 16)	7.6	20
M2.2	(36, -20, 14)	8.1	23
F	(56, -28, 4)	8.8	46
2 nd max	(48, -28, 12)	7.4	

Table 5.14: Maxima of foot activity clusters in contralateral SII for normalized data.

Foot activations in contralateral MI			
Session	Coordinates [mm]	t-score	cluster size [vx]
M1.1	(-2, -18, 68)	10.0	101
M1.2	(0, -20, 68)	12.0	165
M1.3	(0, -16, 70)	13.5	297
M2.1	(8, -16, 74)	8.3	25
M2.2	(8, -18, 72)	11.9	63
M2.3	(8, -18, 74)	11.7	36
F	(4, -22, 68)	8.8	60

Table 5.15: Maxima of foot activity clusters in contralateral SI for normalized data.

The maximum t-scores of the normalized data are generally larger than the corresponding ones of the non-normalized data. This is mainly due to the resampling during normalization, which involves sinc interpolation and increases the signal to noise ratio. The normalized clusters are mostly smaller than the corresponding non-normalized ones. The M1.1 index finger activity cluster in SI, for example, consists of 241 non-normalized voxels or of 1106 normalized voxels, which correspond to 15.4 cm^3 and 8.85 cm^3 respectively. The ‘shrinking’ of the activation volume also originates in the resampling process. On the border of the activity clusters interpolation between pure noise voxels and voxels with a small signal is performed, which eliminates the small signal in most cases. The normalization process also includes zooming and warping of the individual brain, which may change the size of the activation clusters either way depending on the size and shape

of the individual brain. The normalized coordinates of the maximum t-scores are well reproduced within each run for each individual subject as expected. In the following the reproducibility across subjects will be investigated.

Summary

Regarding the index activation in SI the maximum t-scores from sessions N1.1 and F are closest to each other (0.6 cm) while those from N1.2 and M2.3 are farthest apart (3.6 cm). It is rather surprising that the first and the second maxima from session M1.3 were swapped by the normalization process. The separation of the maximum t-values in index finger SII activation ranges from 0.9 cm (M2.1 and F) to 2.4 cm (N1.2 and M2.2). The detected ipsilateral activations of SI in the normalized data exhibits the largest maximum separation of all clusters of interest. The maxima from session N1.1 and run M2 are only 0.3 cm apart while those from F and N1.2 differ by 4.4 cm. Index finger activations in MI were only detected for sessions M2.3 and F and the corresponding maxima are located 2.2 cm from each other. The x-coordinates for the activation of SI due to stimulation of the foot are reproduced exactly for subjects M and N and deviate by only 2 vx for subject F. The minimum and maximum separations are 0.8 cm and 2.1 cm for M1.1 versus N1.2 and M1.3 and M2.1 respectively. It is surprising that the maximum deviation occurs for the same subject on opposite cerebral hemispheres. In general the foot activation in SI for M2 and F are found posterior to those for M1 and N1. In SII the foot activations are at least 0.3 cm (N1.2 and M2.1) and at most 2.9 cm (M1.3 and F) apart. The separation of those in MI differ between 0.7 cm (F and M2.2) and 1.2 cm (M1.1 and M2.1). Again the maximum separation occurs for one subject. Table 5.16 summarizes the minimum and maximum distances between the coordinates of the most significant voxels for each area of interest.

Minimum and maximum distances of maximum t-scores for each region [mm]						
Index				Foot		
SI	SII	MI	ipsilat. SI	SI	SII	MI
2.8	8.9	21.6	2.8	8.2	2.8	6.9
36.3	24.2	21.6	41.7	21.3	28.6	11.8

Table 5.16: Minimum and maximum distances of most significant voxels for each region of interest.

5.7 Non-interference of the PTD with the MRI

For the investigation of possible interference of the PTD with the MRI image acquisition two experiments with the brain phantom ‘Oscar’⁴ in the head coil were performed. During the control experiment (A) the modules were removed from the MRI tube and all related electronic equipment was turned off. For experiment B one module of the PTD was positioned inside the magnet at the location where the right hand would be for a human subject. The same paradigm file as that for the first experiment with subject F was used to run the module, i. e. it was activated for 10 images, then turned off for the next 10 images etc. The technical specifications are also identical to those of the experiment with subject F (200 images total, TR = 3.9 s, 1 image = $26 \times 64 \times 64$ vx, 1 vx = $3.9 \text{ mm} \times 3.9 \text{ mm} \times 5 \text{ mm}$, FOV = 25 cm).

Preprocessing of the images is reduced to smoothing with a Gaussian kernel of FWHM = $8 \text{ mm} \times 8 \text{ mm} \times 10 \text{ mm}$ corresponding to approximately twice the voxel size. Realignment is not necessary. Just to be on the save side the dummy brain was taped to the head restraint. Normalization was not performed either since no comparison to other brain phantoms will be made.

The first column of the design matrix is a simple box-car function with a period of 20 images ($\hat{=} 78 \text{ s}$). Since no physiological changes need to be modeled no high-pass filter, no convolution with the haemodynamic response function or lagging of the box-car function is necessary.

Contrasting is done both for the ‘active’ and for the ‘compare’ phase, with $\vec{c} = [1 \ 0]$ and $\vec{c} = [-1 \ 0]$. The resulting statistical parametric maps of t-scores were thresholded at a much lower level of significance than those from the experiments with human subjects. An uncorrected threshold $p = 0.001$ with no additional spatial extent threshold was chosen. For the ‘active’ phase this threshold results in 7 and 5 activity clusters for experiments A (w/o PTD) and B (w/ PTD) respectively. The most significant voxels exhibit t-scores of $t_A = 4.07$ and $t_B = 3.46$. These t-scores correspond to expected Euler Characteristics of $EC_A = 0.578$ and $EC_B = 0.996$. This means that the probability p to have occurred by chance of even the most significant clusters is 57.8 % and 99.6 % for experiments A and B respectively. At a first glance 57.8 % does not seem to be a convincing value. Without correction for type II error (false positives) twelve chance clusters were expected for each one of the ‘active’ phases. Only seven clusters were detected and one of them having a significance of 42.2 % is well within normal statistical fluctuations. The same threshold yields 5 clusters with a maximum of $t_A = 3.98$ and no clusters for exp. B at all for the ‘compare’ phases. It can safely be concluded that there is no indication of interference of the PTD with the MRI image acquisition.

⁴JB005, Nuclemed sa., Roeselare 8800, Belgium

5.8 t-Scores Reviewed

In the last chapters the functional brain image series were analyzed by means of a voxel by voxel hypothesis testing approach. The hypothesis was set up by using the general linear model and a parameter estimation was performed. These parameters were then used to evaluate the significance of each voxel via a student's t-test. The t-test used by SPM99 is based on the signal change relative to the approximated residual variance, where 'signal change' refers to a linear compound of the estimated parameters of interest. The t-scores depend on the quality of the estimation and on the noise level in the signal. In this chapter the data of selected voxels is analyzed in more detail to obtain a better understanding of the t-values. The following analysis shall also verify the presence and the quality of the signals.

5.8.1 Signal and Cascades

The relationship of the t-score to the quality of the signal is investigated at a basic level in this section. A signal with a high t-score should basically be of a box-car shape with period T, lagged by one image. Ideally it would reflect a lagged box-car convoluted with the haemodynamic response function, but this effect is probably occluded by the noise. If a periodic structure underlies the signal and is merely covered up by uncorrelated noise, it should become apparent in a periodic superposition of the signal. Using equation 5.1 to cascade the signal upon itself the uncorrelated noise should be diminished while the signal remains.

$$C(j) = \frac{T}{N} \cdot \sum_{k=0}^{\frac{N}{T}-1} S(k \cdot T + j) \quad 1 \leq j \leq 20 \quad (5.1)$$

N - length of signal

T - period of box-car function

The signals that will be analyzed in this section are taken from the experiments with subjects M and N. Each signal consists of N=200 data points. The data is already pre-processed, i. e. realignment and smoothing has been performed. For voxels that are active during the index finger stimulation the time scheme should be a box-car of period T=20 images. Images 2 - 8 should exhibit a larger signal than images 1 and 9 - 20 in each period. For voxels that are active during the foot stimulation, the signals from images 12 - 18 should exceed those from the other images in every period.

At first the signals of voxels with different significances are compared. The left sides of figures 5.13, 5.14 and 5.15 show the signal at an insignificant (t=0.2), a significant (t=7) and a highly significant (t=18) voxel. The insignificant voxel does not exhibit any periodic structure. There is only noise with amplitudes of up to 80 points in greyvalue corresponding to about 2% of the mean signal \hat{S} . With a little imagination the signal of the voxel with a t-score of 7 shows a periodic structure, but it is ambiguous. The signal amplitude is less than 1% of the mean. Only the signal with a very high significance can

be identified as basically corresponding to a box-car shape with an amplitude of about 1.6% of \hat{S} . The signal is still confounded by noise of approximately 0.8% of the mean. Hence the signal to noise ratio is in the order of 2 to 1.

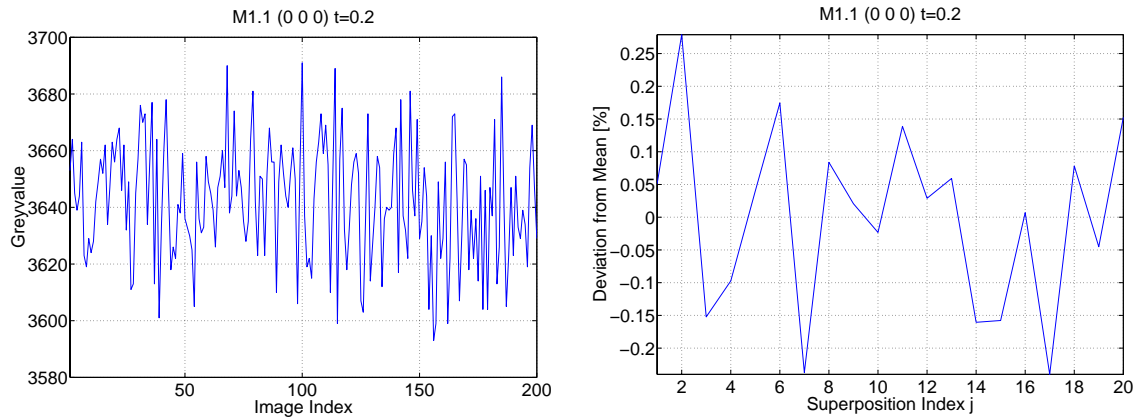


Figure 5.13: Signal and cascaded signal of an insignificant voxel ($t=0.2$), i. e. one that is not involved in processing the presented stimulation.

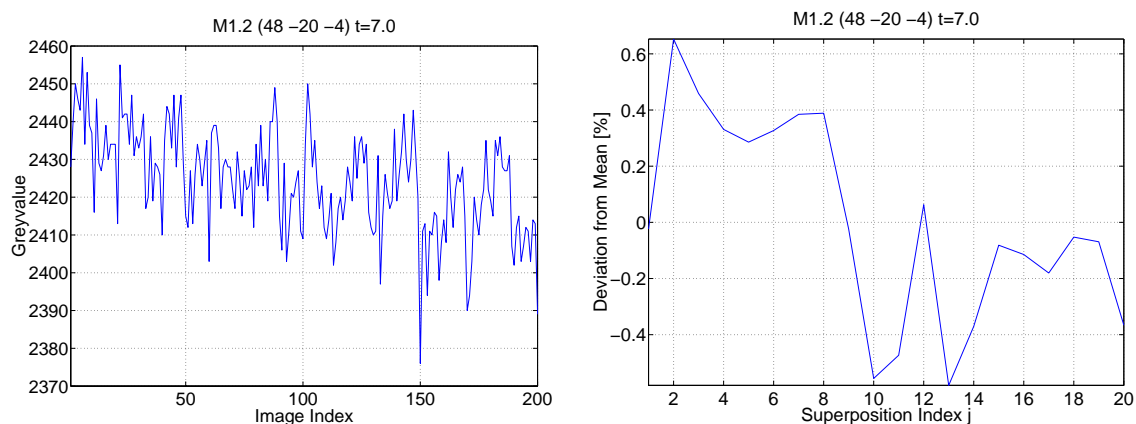


Figure 5.14: Signal and cascaded signal of a significant voxel ($t=7$) in SII for session M1.2.

The deviation of the signals cascaded according to equation 5.1 from the mean signal in percent is depicted in the right parts of figures 5.13, 5.14 and 5.15. Cascading the signal from the insignificant voxel does not yield an apparent structure. Only the amplitude of the noise is reduced to about 0.5% of the signal mean as would be expected for uncorrelated noise. The cascade of the voxel with a significance of $t=7$ does show a larger signal for $2 \leq j \leq 8$ as would a box-car function lagged by one image. The expected lag of 1 image, that has been modeled in the design matrix for the analysis with SPM99, becomes

apparent in the steep initial rise to 0.6% above the mean signal for the 2nd image. It is followed by a decrease and the signal remains at about 0.4% above \hat{S} until it drops to 0 for the 9th image. The lower part of the box-car is not as obvious as there are still large variations akin to those in fig. 5.13. The cascade of the highly significant voxel ($t=18$) resembles the single lagged box-car in a reasonable fashion. There is still a decrease in the upper part of the box-car and the lower part is not flat either, but this could not be expected from a signal with only 10 measurements per data point.

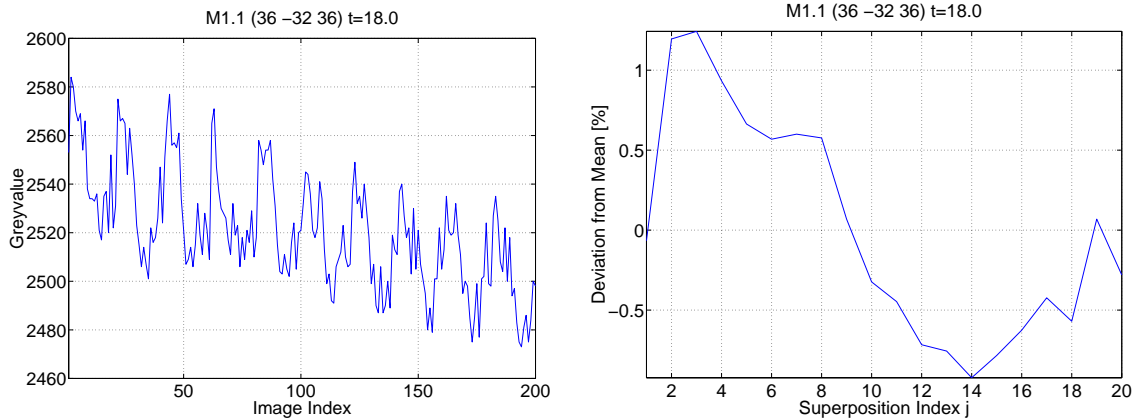


Figure 5.15: Signal and cascaded signal of a highly significant voxel ($t=18$) in SI for session M1.1

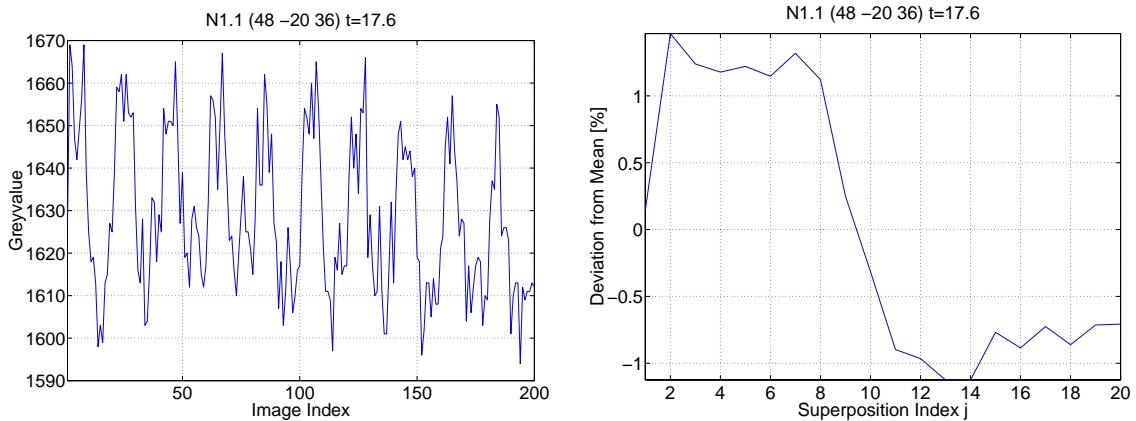


Figure 5.16: Signal and cascaded signal of a highly significant voxel ($t=17.6$) in SI for session N1.1

There is an apparent baseline drift in the signal in figure 5.15. In the design matrix of SPM99 this is modeled by means of the high-pass filter, so it should not confound the parameter estimation. Hence this drift should not influence the t-value. To emphasize this point figure 5.16 shows the signal and the cascaded signal of a voxel with a comparable significance ($t=17.6$). This signal from session N1.1 does not drift like the one from session M1.1, but its t-score is still smaller. In addition the cascaded signal in fig. 5.16 is much clearer than the one in fig. 5.15.

The cascaded signals can of course not be used as a quantitative measure for the quality of the signal. The signals do not comprise enough data points and the signal to noise ratio is usually too high (about 2 to 1) to allow for a reasonable elimination of the uncorrelated noise. Averaging the cascades from neighbouring voxels does not really improve the cascades for smoothing has introduced a strong correlation between the neighbours. Increasing the size of the neighbourhood will reduce correlation but also signal to noise for less significant voxels are inevitably included. The cascades nevertheless emphasize the basic form of the signal and serve as a qualitative illustration.

5.8.2 Autocovariance

Autocorrelation is measure for correlation within the signal of one voxel (compared to correlation that compares the signal of several voxels to each other or to a reference signal). An autocovariance function normalized to the variance of the signal is calculated for selected voxels according to equation 5.2 to look into its possibilities of evaluating the significance of a signal. The normalization introduces a dependence of the amplitude of the autocovariance function on the noise. The signal was subject to cyclic addition before calculating the autocovariance.

$$AC(\Delta i) = \frac{1}{N} \cdot \frac{1}{AC(0)} \sum_{k=1}^N [S(k) - \hat{S}] \cdot [S(k + \Delta i) - \hat{S}] \quad (5.2)$$

The autocovariance function of the insignificant voxel with $t=0.2$ (see fig. 5.17, left) does not exhibit a periodic signal and has small amplitudes (up to ± 0.15) as expected. A higher significance is reflected in a periodicity of the autocovariance function as in fig. 5.17, right) and a higher amplitude. Maxima are reached for multiples of 20, but the shape of the curve is not smooth as it is when the significance increases (fig. 5.18). The drift that can be observed in the signal for voxel (36,-32,36) in session M1.1 (see also fig. 5.15) is reflected in the autocovariance function. The autocovariance function of voxel (48,-20,36) from session N1.1 owns a larger amplitude and lacks the drift that is present in fig. 5.18, left side even though its t-score is lower.

The autocovariance can be used to evaluate the significance of the signal. The smoother the shape of the autocovariance and the larger its amplitude, the clearer was the original signal. Both the cascade and the autocovariance functions of voxels (36,-32,36) from session M1.1 and (48,-20,36) from session N1.1 suggest that the latter one's signal is more significant in spite of the t-scores that indicate the opposite.

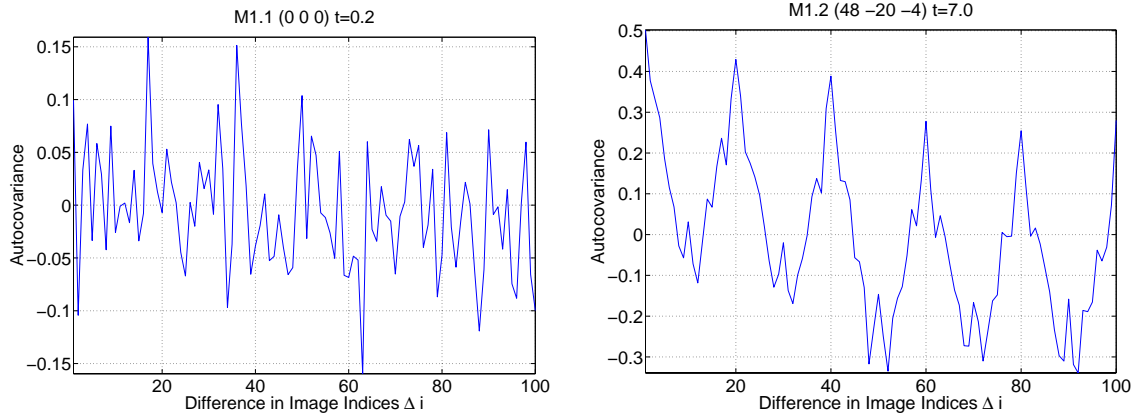


Figure 5.17: The autocovariance functions for voxels with $t = 0.2$ and $t = 7.0$ calculated with equation 5.2.

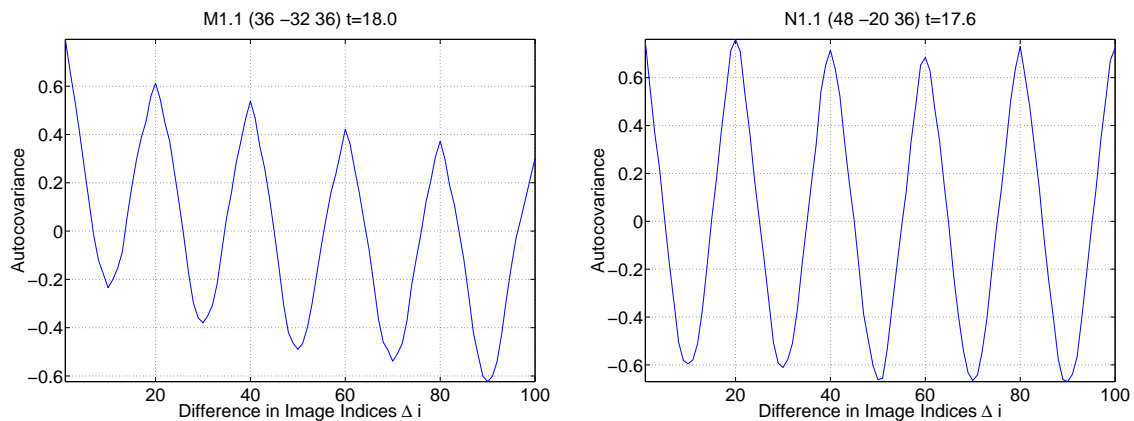


Figure 5.18: The autocovariance functions for voxels with $t = 18.0$ and $t = 17.6$ calculated with equation 5.2.

5.8.3 Fourier Transformation

A discrete fourier transformation is performed on the signals of the same selected voxels with different t -scores. The corresponding power spectra are displayed in figures 5.19 and 5.20. The first element of the power spectrum is omitted as it corresponds to the sum of all data points of the signal and would stretch the scale too much. The signal of the insignificant voxel with $t = 0.2$ obviously contains many frequencies indicating that there is only noise. The power spectrum of the voxel with $t = 7.0$ looks like what a typical fMRI signal is expected to look like. The cardiac and respiratory cycles of generally about 1 and 0.25 Hz respectively are aliased into the range $0 \leq f \leq F_{Nyquist}$. The Nyquist frequency corresponds to $F_{Nyquist} = 0.1$ Hz for a signal with $TR = 5$ s. Hence the cardiac frequency of $f = 1$ Hz would be aliased to 0 Hz and the respiratory one of $f = 0.25$ Hz to 0.05 Hz. The

cardiac and the respiratory were not measured, so it is not possible to say which one of the small peaks at 0.02, 0.04 and 0.06 Hz in the power spectrum they correspond to. The $1/f$ low-frequency noise can also be discerned (see also 2.5.2). The actual signal with $f_0 = 0.01$ Hz yields the largest peak with about 4 times the amplitude of the peaks for the periodic noise in the signal of voxel (48,-20,-4) in session M1.2. The peaks corresponding to $f_0 = 0.01$ Hz in the highly significant voxels in figure 5.20 are more explicit. They both have about 18 times the height of the periodic noise peaks. It is interesting that the $1/f$ noise is very low for subject N (right plot) while it is comparatively large for subject M (left plot). The level of $1/f$ noise does not seem to influence the t-value.

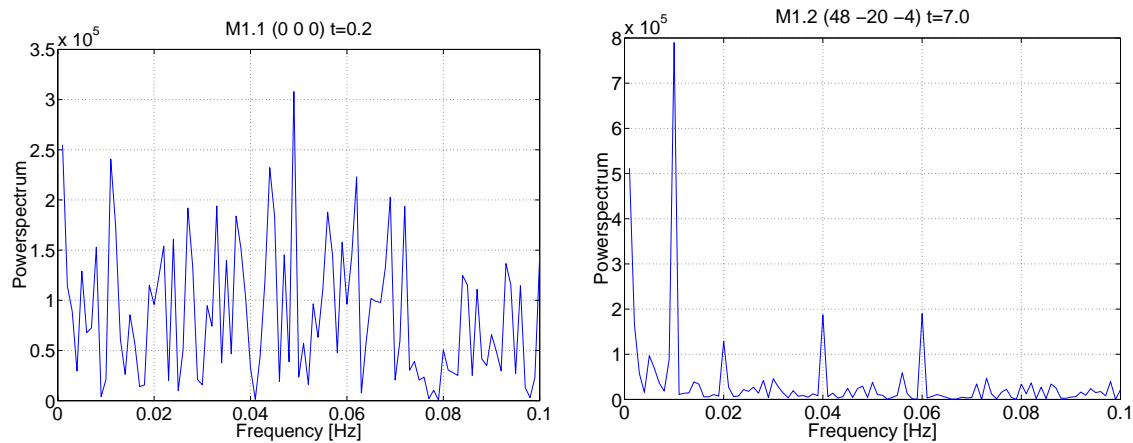


Figure 5.19: Power spectrum of voxels with $t=0.2$ and $t=7.0$.

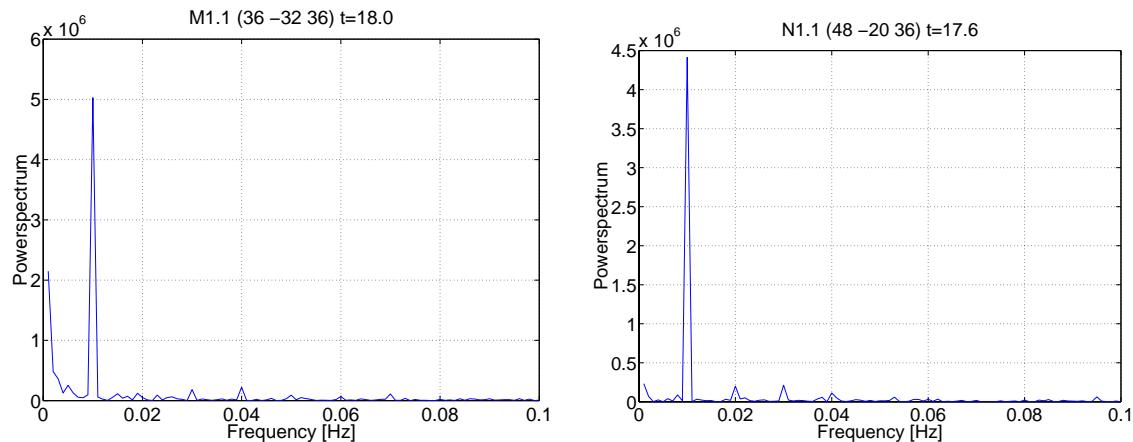


Figure 5.20: Power spectrum of voxels with $t=18.0$ and $t=17.6$.

The power spectrum of a signal yields further verification of the significance of the signal. The high peaks in fig. 5.20 demonstrate the high significance while the smaller peak in fig. 5.19 for the less significant voxel ($t = 7.0$) shows that the signal is less explicit. In the following it will be investigated whether it is possible to detect the presence of a signal in the brain by determining the averaged power spectrum from a large part of the brain or whether it will be eliminated by the noise. Figure 5.21 depicts the averaged power spectrum from all voxels within a bounding box of $[0:68,-60:0,-12:72]$ (in mm). This bounding box corresponds to the upper two thirds of the left cerebral hemisphere including both the primary and the somatosensory cortex as well as the motor cortex. The averaged power spectrum exhibits a large $1/f$ low frequency noise component and small periodic noise peaks at 0.02 and 0.04 Hz. The signal at 0.01 Hz is still present, but has been diminished and cannot be distinguished from the periodic noise peaks with confidence. The signal in this area was very strong (two major clusters of 241 and 18 vx respectively and t-scores within $5.5 \leq t \leq 18$) and usually lesser signals are still considered significant. The fourier transformation cannot confidently detect the presence of a periodic structure in a fMRI signal if an averaged power spectrum is used. significance of the voxel.

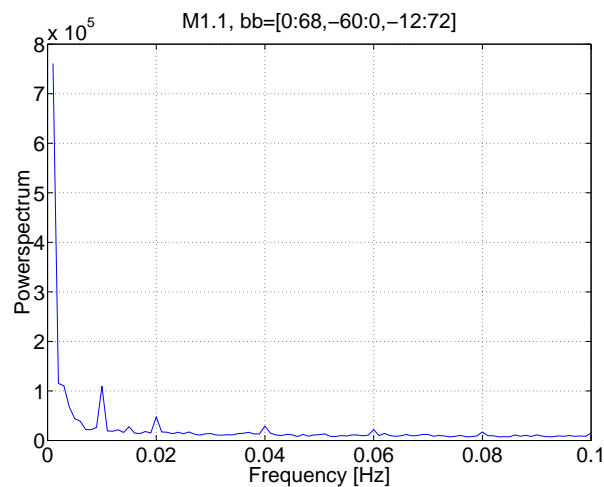


Figure 5.21: Averaged power spectrum of all voxels within a bounding box of $[0:68,-60:0,-12:72]$.

Summary and Outlook

First fMRI experiments on healthy, seeing subjects were performed with a new pneumatically driven tactile display to investigate the processing of tactile stimulation in the human brain. They succeeded in mapping the expected somatotopic representation in the contralateral primary somatosensory cortex for three subjects at two distinct points (the index finger and the foot). For one subject the representation of the arm in SI was also located. The tactile stimulation with the PTD did not only cause brain activation in SI but also in SII and MI. In some sessions ipsilateral activation of SI, SII or MI was also detected. The observed activation of SII also exhibits a somatotopic map similar to that of SI.

Even though great care was taken to avoid motor stimulation the primary motor cortex was activated. This leads to the assumption that the somatosensory and the motor cortex are strongly interconnected. The experiments with subjects M and N result in one large index finger activation that spans both SI and MI. The PTD was operated at an air pressure of 5.9 bar for these experiments. Only 4 bar were applied for the experiment with subject F whose index finger activation is focussed in SI and merely 'leaks' into MI. Hence using the PTD with a smaller air pressure is likely to reduce the motor stimulation. A measurement of the force exerted by one taxel of the PTD is currently performed at the Department of Clinical and Biological Psychology of the University of Mannheim. Aside from the pressure dependence, the influence of the frequency on the taxel force is of particular interest.

In one of the performed experiments the frequency of the walking pattern applied to one module of the PTD was varied pseudo-randomly between 0.7 Hz, 1.23 Hz and 5 Hz. The variation does not appear to influence either the activation cluster size, the maximum t-value or its location. Before the dependence of the brain activation on the frequency is further examined it is important to clarify the relationship of both frequency and brain activation to the applied force.

An adaptation effect over the period of one hour was not discernable. It seems that healthy subjects can concentrate on the tactile stimulations performed with the PTD for at least one hour without their brain's response to the stimulus being reduced.

The reproducibility of the brain activations was also analyzed. The coordinates of the maximum t-scores are well reproduced for each individual subject (within one cerebral hemisphere) while the actual t-values and the cluster sizes are subject to large random variations. The deviation of activations due to tactile as well as motor stimulation is less than 1.2 cm and for most cases even less than 0.5 cm. For one subject the reproducibility across the cerebral hemispheres was examined and it turned out that the coordinates of

the maximum t-scores are subject to deviations up to 2.4 cm. The reproducibility of the locations of the maximum t-scores in the intersubject analysis varied between 3 mm to 4 cm. An experiment with a brain phantom shows that the PTD does not perturb the fMRI image acquisition.

The reported experiments with seeing subjects induced activation of the somatosensory and the motor cortex. A next step could be to perform experiments with blind subjects to examine whether they exhibit activation of the same brain areas or if other areas, e. g. the visual cortex, are also involved. It would also be useful to be able to compare the degrees of activation in blind and seeing subjects. Statistical parametric mapping is unfortunately not well-suited to evaluate the intensity distribution of the activation. The t-scores do not provide a reliable measure of the degree of activity and the thresholded statistical parametric maps should rather be regarded as a black and white map of significance versus no significance. A new approach based on wavelet transforms might be more appropriate for comparing the intensities of activations as it results in a profile of activity [Tur99]. Wavelet transform methods differ from traditional Fourier methods by their inherent ability of localizing information in the time-frequency domain while by means of a Fourier transformation the information of either time or frequency is lost.

Statistical parametric mapping has nevertheless succeeded in precisely localizing activation sites. It should be possible to perform future analyses using SPM99 much faster so increasing the statistic should be considered. The main speed factor is that the analysis has been automated using the newly implemented batch modus of SPM99. All analysis steps except for thresholding can be performed automatically now. Thresholding is still rather time-consuming since it is often necessary to try different thresholds for all data sets. Automatisation of thresholding with SPM99 is desirable.

The intersubject analysis using normalized data yielded rather large deviations in the localization of activations. It seems to be preferable to analyze each subject individually by superposition of the activations onto structural scans. A new extension to SPM99 allows to print series of coronal, sagittal or axial slices of those superpositions. This also speeds up the analysis as it eludes tedious inspection with SPM99's interactive user interface.

Having shown the authenticity of the data detected with SPM99 and using the PTD for tactile stimulation new experiments do not need to restrict themselves to simple tactile stimulation. The next step could be to proceed to investigations into pattern recognition. Only a better understanding of how complex tactile stimulations and patterns are processed by both blind and seeing subjects can finally help to optimize information transfer via the tactile channel to the human brain.

Appendix A

Directions and Planes in the Human Brain

The terminology of neuroanatomy is specialized to describe both the absolute position of structures and their relative position. Two major axes, the dorsal-ventral and the rostral-caudal axis, describe the organization of the central nervous system. For animals, e. g. a mouse the rostral-caudal axis runs approximately in a straight line from the nose to the tail. The dorsal-ventral axis is perpendicular to the rostral-caudal axis and runs from the back to the abdomen. In humans the situation is a bit more complicated (see fig. A.1). The rostral-caudal axis does not follow a straight line but instead undergoes a bend (or flexure) at the midbrain. The terms inferior and superior are used to describe structures located rostral to this bend. The planes in which anatomical sections or slices are made are named horizontal (or axial), coronal and (para-) sagittal (see fig. A.1).

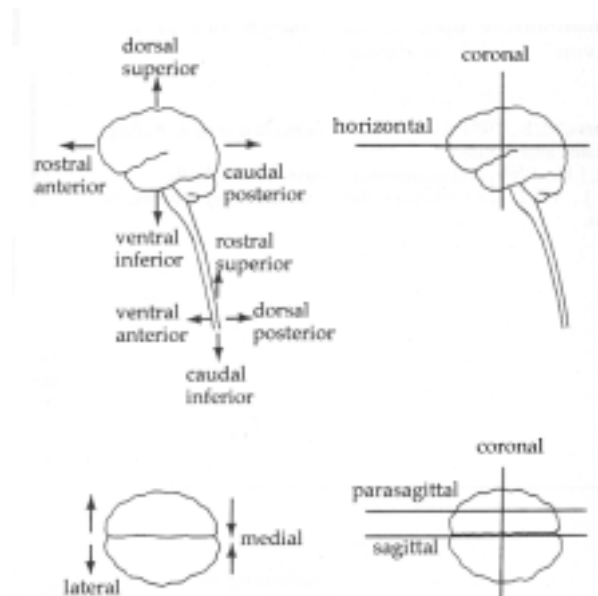


Figure A.1: Directions and Planes in the Brain

Appendix B

Affine Transformations in Preprocessing

B.1 General Affine Transformation

The affine transformation is a simple and well defined spatial transformation. In 3-D it is given by 12 parameters. For each point (x_1, x_2, x_3) in an image mapping into the coordinates of another Euclidean space is given by

$$\begin{pmatrix} y_1 \\ y_2 \\ y_3 \\ 1 \end{pmatrix} = \begin{pmatrix} m_{11} & m_{12} & m_{13} & m_{14} \\ m_{21} & m_{22} & m_{23} & m_{24} \\ m_{31} & m_{32} & m_{33} & m_{34} \\ 0 & 0 & 0 & 1 \end{pmatrix} \begin{pmatrix} x_1 \\ x_2 \\ x_3 \\ 1 \end{pmatrix}$$

Several transformations can be combined in one by simply multiplying the transformation matrices to form a single matrix.

Rigid body transformations are a subset of the more general affine transformations. In 3 dimensions a rigid body transformation is defined by six parameters.

B.2 Voxel to Real World Coordinates

The matrix M_f is responsible for converting voxel coordinates to ‘real world’ coordinates. If an image f has a voxel size of $xmm \times ymm \times zmm$ and an origin (in voxels) (X, Y, Z) then

$$M_f = \begin{pmatrix} x & 0 & 0 & (-x \cdot X) \\ 0 & y & 0 & (-y \cdot Y) \\ 0 & 0 & z & (-z \cdot Z) \\ 0 & 0 & 0 & 1 \end{pmatrix}, \quad M_f^{-1} = \begin{pmatrix} \frac{1}{x} & 0 & 0 & X \\ 0 & \frac{1}{y} & 0 & Y \\ 0 & 0 & \frac{1}{z} & Z \\ 0 & 0 & 0 & 1 \end{pmatrix}$$

B.3 Realignment

The realignment of an image f to an image g , performed as a preprocessing step in SPM99, is a rigid body transformation with the transformation matrix $M_{realign}$. The parameters \mathbf{q} account for translation (q_1, q_2, q_3) in x, y and z as well as for rotation (q_4, q_5, q_6) around the x-, y-, and z-axis.

$$M_{realign} = M_f^{-1} \underbrace{\begin{pmatrix} 1 & 0 & 0 & q_1 \\ 0 & 1 & 0 & q_2 \\ 0 & 0 & 1 & q_3 \\ 0 & 0 & 0 & 1 \end{pmatrix}}_{\text{Translations}} \times \underbrace{\begin{pmatrix} 1 & 0 & 0 & 0 \\ 0 & \cos q_4 & \sin q_4 & 0 \\ 0 & -\sin q_4 & \cos q_4 & 0 \\ 0 & 0 & 0 & 1 \end{pmatrix}}_{\text{Pitch}} \times$$

$$\underbrace{\begin{pmatrix} 0 & \cos q_5 & \sin q_5 & 0 \\ 1 & 0 & 0 & 0 \\ 0 & -\sin q_5 & \cos q_5 & 0 \\ 0 & 0 & 0 & 1 \end{pmatrix}}_{\text{Roll}} \times \underbrace{\begin{pmatrix} 0 & \cos q_6 & \sin q_6 & 0 \\ 0 & -\sin q_6 & \cos q_6 & 0 \\ 1 & 0 & 0 & 0 \\ 0 & 0 & 0 & 1 \end{pmatrix}}_{\text{Yaw}} \times M_g$$

M_f and M_g map from voxel to real world coordinates.

B.4 Affine Normalization

For affine spatial transformation an additional 6 parameters are needed: 3 zooms (q_7, q_8, q_9) in x, y and z and 3 shears (q_{10}, q_{11}, q_{12}) in xy, xz and yz.

$$M = M_f^{-1} \underbrace{\begin{pmatrix} 1 & 0 & 0 & q_1 \\ 0 & 1 & 0 & q_2 \\ 0 & 0 & 1 & q_3 \\ 0 & 0 & 0 & 1 \end{pmatrix}}_{\text{Translations}} \times \underbrace{\begin{pmatrix} 1 & 0 & 0 & 0 \\ 0 & \cos q_4 & \sin q_4 & 0 \\ 0 & -\sin q_4 & \cos q_4 & 0 \\ 0 & 0 & 0 & 1 \end{pmatrix}}_{\text{Pitch}} \times$$

$$\underbrace{\begin{pmatrix} 0 & \cos q_5 & \sin q_5 & 0 \\ 1 & 0 & 0 & 0 \\ 0 & -\sin q_5 & \cos q_5 & 0 \\ 0 & 0 & 0 & 1 \end{pmatrix}}_{\text{Roll}} \times \underbrace{\begin{pmatrix} 0 & \cos q_6 & \sin q_6 & 0 \\ 0 & -\sin q_6 & \cos q_6 & 0 \\ 1 & 0 & 0 & 0 \\ 0 & 0 & 0 & 1 \end{pmatrix}}_{\text{Yaw}} \times$$

$$\underbrace{\begin{pmatrix} q_7 & 0 & 0 & 0 \\ 0 & q_8 & 0 & 0 \\ 0 & 0 & q_9 & 0 \\ 0 & 0 & 0 & 1 \end{pmatrix}}_{\text{Zoom}} \times \underbrace{\begin{pmatrix} 1 & q_{10} & q_{11} & 0 \\ 0 & 1 & q_{12} & 0 \\ 0 & 0 & 1 & 0 \\ 0 & 0 & 0 & 1 \end{pmatrix}}_{\text{Shear}} \times M_g$$

Appendix C

Coordinates in SPM99

C.1 Talairach Coordinate System

The Talairach Coordinate System (TCS) is determined by a line through the superior edge of the *Anterior Commissure* and the inferior edge of the *Posterior Commissure* - the AC-PC line - and the interhemispheric, sagittal plane. The AC is also the origin of the coordinate system. Fig. C.1 illustrates the TCS.

Why the commissures? Both commissures are relatively easy to locate on structural scans. On functional scans (EPI) it is hard to make out the PC but the AC can still be located with confidence. The main idea of the TCS was actually to provide comparability of individual brains.

A brain is divided into cuboids, the dimensions of which vary with the principal axes. The volume defined by the plane to the interhemispheric plane and passing through the AC-PC line and the lowest point of the temporal cortex is, for example, divided in 4 equidistant sections, etc.. It is a proportional grid system. This feature is not relevant here since multi-subject comparison is performed on normalized brains.

C.2 The MNI brain

In order to define a brain that is more representative of the population than the single brain used by Talairach and Tournoux, members of the Montreal Neurological Institute did a large number of MRI scans on normal subjects. Every brain was then linearly matched to the Talairach brain. The transform consisted of 9 parameters (3 translations, 3 rotations and 3 zooms). Two average brains were created: a 305 and a 152 average. SPM99 uses the 152 average brain. The MNI linear transform has not matched the brains completely to the Talairach brain, so the MNI brains turned out to be slightly larger. The differences are larger on the outer parts of the brain and are at maximum in the order of 10 mm. From the AC to its top the MNI brain is about 5 mm taller and 5 mm longer. Its temporal lobes go about 10 mm deeper (the lowest slice is at $z = -50$ compared to $z = -40$ in the Talairach atlas). The AC, which serves as origin, is 4 mm below that of the Talairach brain.

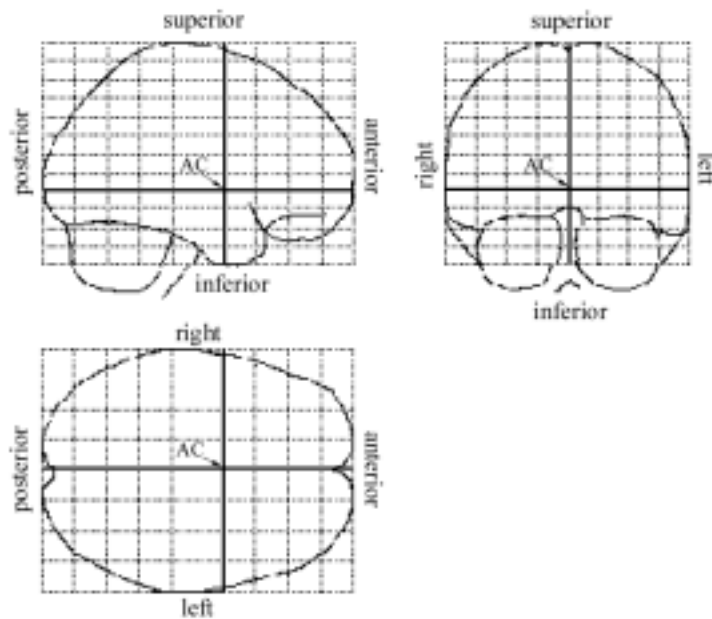


Figure C.1: The Talairach Coordinate System with the origin located in the AC.

It is not possible to do an exact transformation from the MNI to the Talairach brain, but there are some approximations (see [Bre99]). This is unfortunate since the Talairach atlas depicts the designated Brodman's areas. So far there is no published MNI atlas defining Brodman's areas on the MNI brain.

Appendix D

Examples for Batch-Files in SPM99

defaults.m

```
%-----  
% batch variables defined here for analysis 'defaults_edit'  
%-----  
  
defaults_edit(1) = struct( ...  
    'type_area', [1 2 3 4], ...  
    'index', [1 1 1 1] );  
  
type_area = {'Misc', 'Printing', 'RealignCoreg', 'Normalisation', ...  
    'Hdr', 'Statistics', 'Reset'};  
  
%===== Misc Defaults  
Misc = struct( ...  
    'log_to_file', 1, ...  
    'log_file_name', 'spm.log', ...  
    'cmdline', 0, ...  
    'grid', 0.4 );  
  
%===== Printing Defaults  
Printing = struct( ...  
    'printing_mode', 3, ...           % ps to file  
    'postscript_filename', 'spm', ...  
    'postscript_type', 8, ...         % 8 is eps level 2;  
    'default_printer', 0, ...  
    'printer_name', '', ...  
    'post_type', '-dpsc', ...  
    'graphics_filename', 'spm', ...  
    'graph_type', 4, ...  
    'print_string', '' );  
  
%===== RealignCoreg Defaults  
RealignCoreg = struct( ...  
    'separate_combine', 1, ...        % combine coregistration  
                                       % and realignment
```

```

'create', 1, ...
'adjust', 1, ...           % adjust sampling errors
'mask', 1, ...            % mask object brain
'reg_quality', 1.00, ...  % registration quality
'weight_reg', 0 );       % allow weighting

%===== Normalisation Defaults
Normalisation = struct( ...
'defaults', 1, ...        % 1 - parameter estimation
'estimates', 0, ...       % Neurological Convention (R is R)
'custom_norm', -1, ...    % -1 - allow customized
                        % 1 - disallow
'nonlin_func_nb', 13, ... % non-linear basis functions
'func_nb', 0, ...
'nonlin_ite_nb', 12, ...  % non-linear iterations
'nonlin_regular', 0.01, ... % strength of regularization
'mask_brain', 1, ...      % 1 yes
'bounding_box', 1, ...    % default bounding box
'voxel_sizes', 3 );      % 3 <-> 2*2*2 mm

```

prepro1.m

```

%-----
% user variables defined here
%-----

datadir='/misc/tmp/vision/ex_28jun00/M/ex1/';
Fr = {spm_get('files',datadir,'m1_1*.img')};
Frs = {spm_get('files',datadir,'rml_1*.img')};

%-----
% batch variables defined here for analysis 'realign'
%-----

realign = struct(...
'subject_nb', 1, ...      % number of subjects
'num_sessions', 1, ...   % number of sessions for each subject
'sessions', [1], ...     % index into structure sessions
'option', 3, ...         % 1 - only registration
                        % 2 - only transformation
                        % 3 - both
'modality', 1, ...       % 1 - within modality
                        % 2 - between modality
'reslice_method', -9, ... % interpolation method: -9 <-> sinc
'create', 3, ...         % 3 - mean image + all images
'mask', 1, ...           % 1 - mask voxels outside the brain
'adjust_sampling_errors', 0);

%-----

sessions(1) = struct(...
'images', {{Fr}});

```

```

%-----
% batch variables defined here for analysis 'smooth'
%-----

smooth = struct(...
'FWHMmm', [8 8 8], ...
'files', {{Frs}} );

```

prepro2.m

```

%-----
% user variables defined here
%-----

datadir='/misctmp/vision/ex_28jun00/M/ex1/';
Fn = {spm_get('files', datadir, 'rml_1*.img')};
Fns = {spm_get('files', datadir, 'nrml_1*.img')};

%-----
% batch variables defined here for analysis 'normalize'
%-----
% attention: defaults have to be set to allow customized
% normalization for these settings to take effect

normalize = struct(...
'option', 3, ...
% 1 - determine parameters only
% 2 - perform transformation
% 3 - 1+2
'nbsubjects', 1, ...
% number of subjects
'estimates', 1, ...
% 0 - radiological convention
% 1 - neurological convention
'object_masking', 0, ...
% mask object brain during
% registration
'objmask', {''}, ...
% file containing mask
'template', ...
' SPM_dir/templates/EPI.img', ... % template image for normalization
'image', {{Fn1}}, ...
% image to determine parameters from
'matname', ...
% file to write parameters to
{{'filename.mat'}}, ...
'images', {{Fn}}, ...
% images to write normalized
'type', 1, ...
% default normalization = 0
% custom normalization = 1
'nonlin_func_nb', 13, ...
% number of non-linear basis fcts
% (0:14); 13 = 7*8*7
'func_nb', 0, ...
% number of basis functions
% (only for 'custom')
'nonlin_ite_nb', 12, ...
% number of non-linear iterations
'nonlin_regular', 0.01, ...
% Extremely heavy (1.0) to very
% light regularization (0.0001)
'mask_brain', 1, ...
% mask object brain during
% transformation in order

```



```

% not to count exterior voxels
'interp', -9, ... % interpolation type:
% 0 <-> nearest neighbour (fast)
% 1 <-> bilinear (slower)
% -9 <-> sinc (slowest, but best)
'bounding_box', 3, ... % 0 - custom
% 1 - default
% (-78:78,-112:76,-50:85)
'direction1', [-10;10], ... % only if 'custom'
'direction2', [-10;10], ...
'direction3', [-10;10], ...
'voxel_sizes', 3, ... % voxel size after normalization:
% 0 - custom, 3 - 2*2*2 mm
'voxel_sizes_custom', [2 2 2] ); % if 'custom' 'for voxel_sizes'

%-----
% batch variables defined here for analysis 'smooth'
%-----

smooth = struct(...
'FWHMmm', [4 4 4], ...
'files', {{Fns}} );

```

stat.m

```

%-----
% user variables defined here
%-----

datadir = '/misc/tmp/vision/ex_28jun00/M/ex1/';
Fsr = {spm_get('files',datadir,'srml_1*.img')};
Fsnr = {spm_get('files',datadir,'snrml_1*.img')};

%-----
% batch variables defined here for analysis 'model'
%-----

model = struct( ...
'types', 4, ... % specify and estimate
'global_effects', {'None'}, ... % no global normalization
'burst_mode', 0, ...
'HF_fil', 'specify', ... % high-pass filter
'HF_cut', [200], ... % cut-off = RT * SOA * 2
'LF_fil', 'none', ... % low-pass filter
'LF_cut', 4, ... % cut-off
'int_corr', 'none', ... % internal correlation?
'now_later', 1, ... % estimate 'now' or 'later'
'stop_writing', 0, ... % overwrite existing design
% matrix? (y/n) <-> (0/1)
'trial_fcon', 0, ... % trial specific F-contrasts
'RT', 5, ... % RT [s]
'replicated', 0, ... % are sessions replicated?

```

```

'nssess',          1, ...           % number of sessions
'nscans',          [200], ...       % number of scans
'files',           {{Fsr}}, ...
'conditions_nb',  [2], ...           % number of active phases
'conditions',      [1], ...           % index into structure
                                     % 'conditions'
'regressors_nb',  [0], ...           % number of regressors
'regressors',      [], ...           % indices into structure
                                     % 'regressors'
'parametrics_type', {{'none'}}, ... % parametric modulation
'parametrics',     [], ...           % indices into structure
                                     % 'parametrics'

'stochastics_flag', [0], ...
'stochastics',     [] );

model(2)=model(1);
model(2).files={Fsnr};

%-----

conditions(1) = struct( ...
'names',          {{'trial 1','trial2'}}, ...
'onsets',         {{1:20:200,11:20:200}}, ... % SOA
'types',          {{'epochs','epochs'}}, ... % 'events' for very
                                     % short stimulations

'bf_ev',          [0], ...
'bf_ep',          [1 1], ...         % indices into structure
                                     % 'bf_ep'

'volterra',       0, ...
'variable_dur',   0 );              % variable durations? no

%-----

bf_ep(1) = struct( ...
'ep_type',        4, ...             % '4' = box-car function
'length',         7, ...             % length of active phase
                                     % [scans]

'conv',           1, ...             % convolve with hrf
'deriv',          0 );              % no temporal derivatives

%-----
% batch variables defined here for analysis 'contrasts'
%-----

contrasts(1) = struct( ...
'names',          {{'index','foot'}}, ...
'types',          {{'T','T'}}, ...
'values',         {[1 -1 0],[-1 1 0]}) );

```

Bibliography

- [Afi98] A.K. Afifi, R.A. Bergman, Functional Neuroanatomy, McGraw-Hill, New York (1998)
- [Ana00] <http://www.mayo.edu/bir/analyze/AnalyzeFileInfo.html>
- [Ban93] P.A. Bandettini, MRI studies of brain activation: temporal characteristics. In: Functional MRI of the brain, Berkeley: SMRM, California 143-151 (1993)
- [Bor99] J. Bortz, Statistik, Springer-Verlag, Berlin (1999)
- [Box95] J.L. Boxerman, P.A. Bandettini, The intravascular contribution to fMRI signal change: Monte Carlo modeling and diffusion weighted studie in vivo, Mag. Res. Med. **34**, 4-10 (1995)
- [Bre99] M. Brett, Medical Research Council - Cognition and Brain Science Unit - Imaging, Homepage (1999)
<http://www.mrc-cbu.cam.ac.uk/Imaging/>
- [Bro99] M.A. Brown, R.C. Semelka, MRI Principles and Applications, 2nd edition, Wiley-Liss, New York (1999)
- [Fra97] R.S.J. Frackowiak, K.J. Friston, C.D. Frith, R.J. Dolan, J.C. Mazziotta, Human Brain Function, Academic Press, San Diego (1997)
- [Fri94a] K. Friston, P. Jezzard, R. Turner, Analysis of functional MRI time series, Human Brain Mapping **1**, 153-171 (1994)
- [Fri94b] K. Friston, K.J. Worsley, R.S.J. Frackowiak, Assessing the Significance of Focal Activations Using Their Spatial Extent, Human Brain Mapping **1**:210-220 (1994)
- [Fri95] K. Friston, J. Ashburner, J.B. Poline, Spatial Registration and Normalization of Images, Human Brain Mapping **2**:165-189 (1995)
- [Har00] G. Harrington, C. Wright, H. Downs, A New Vibrotactile Stimulator for Functional MRI, Human Brain Mapping **10**:140-145 (2000)

- [Hor00] J.P. Hornak, The Basics of MRI, Rochester, NY (2000)
http://www.cis.rit.edu/htbooks/mri/bmri.htm
- [Jae97] B. Jaehne, Digitale Bildverarbeitung, Springer, Berlin Heidelberg (1997)
- [Jez99] P. Jezzard, Basic Physics of fMRI, FMRIB, Oxford University, UK (1999)
http://www.fmrib.ox.ac.uk/~peter/j/lectures/hbm_1/sld001.htm
- [Kan91] E.R. Kandel (Editor), Principles of Neural Science, 4th edition, Prentice Hall International, London (1991)
- [Loo99] M. Loose, A Self-Calibrating CMOS Image Sensor with Logarithmic Response, Phd-Thesis, HD-IHEP 99-07, Heidelberg (1999)
- [Mal99] J.A. Maldjian, A. Gottschalk, R.S. Patel, Mapping of Secondary Somatosensory Activation Induced by Vibrational Stimulation: an fMRI Study, Brain Research 824 (1999) 291-295
- [Mar96] J.H. Martin, Neuroanatomy, 2nd edition, Appleton and Lange, Stamford, Conn. (1996)
- [Mau00] T. Maucher, S. Runde, K. Meier, E. Sampaio, C. Scheiber, Evaluation of a new pneumatically driven tactile display for fMRI-studies by mapping the human somatosensory cortex, submitted to Magnetic Resonance in Medicine, July 2000
- [Mau98] T. Maucher, Aufbau und Test eines taktilen Seh-Ersatzsystems, Thesis, HD-IHEP 98-11, Heidelberg (1998)
- [Moo95] D.S. Moore, The Basic Practice of Statistics, W.H. Freeman and company, New York (1995)
- [Nol95] J. Nolte, J.B. Angevine, Jr., The Human Brain in Photographs and Diagrams, Mosby, St. Louis, MO (1995)
- [Ros82] A. Rosenfeld, A.C. Kak, Digital Picture Processing, Volume 2, Academic Press, Orlando (1982)
- [Sch99] J. Schemmel, An Integrated Analog Network for Image Processing, Phd-Thesis, HD-IHEP 99-08, Heidelberg (1999)
- [SPM97] SPM short course notes (1997)
http://www.fil.ion.ucl.ac.uk/spm/course/notes.html
- [Sti99] C. Stippich, R. Hofmann, D. Kapfer, Somatotopic mapping of the human primary somatosensory cortex by fully automated tactile stimulation using functional magnetic resonance imaging, Neurosci-Lett. 277(1):25-8 (1999)

- [Tal88] J. Talairach, P. Tournoux, Co-Planar Stereotaxic Atlas of the Human Brain, Georg Thieme Verlag, Stuttgart (1988)
- [Tra98] I. Tracey, Brief Introduction to FMRI - Physiology, FMRIB, Oxford University, UK (1998)
http://www.fmrib.ox.ac.uk/fmri_intro/physiology.html
- [Tur99] F.E. Turkheimer, M. Brett, D. Visvikis, V.J. Cunningham, Multiresolution Analysis of Emission Tomography Images in the Wavelet Domain, Journal of Cerebral Blood Flow and Metabolism 19(11):1189-1208 (1999)
- [Vis00] Homepage of the Electronic Vision Group
<http://www.kip.uni-heidelberg.de/vision/>
- [Wor96] K.J. Worsley, S. Marrett, Searching Scale Space for Activation in PET Images, Human Brain Mapping 4: 74-90 (1996)

Acknowledgements

At this point I would like to thank everybody who contributed to this work, namely:

Prof. Dr. K. Meier for the opportunity to work on this very interesting - and in the regime of physics rather unconventional - project.

Prof. Dr. J. Bille for taking on the part of second referee.

Thorsten for proof-reading, great teamwork and his always enchanting company throughout the year.

All members of the Electronic Vision Group for their interest in the project and the good vibes within the group.

Dr. C. Scheiber for his support in all questions concerning fMRI and SPM99.

M. Brett for his prompt answers and helpful MATLAB-scripts.

My parents for always supporting me in no matter what.

Frank for proof-reading, for Australia and for bringing out the best in me.